TERAHERTZ METAMATERIALS:

REFRACTIVE INDEX, SENSING, AND RESONANCES

By

LEENA SINGH

Bachelor of Engineering | Electronics & Communications
Uttar Pradesh Technical University,
Lucknow, India
2008

Master of Science | Electrical Engineering
Oklahoma State University,
Stillwater, OK
2015

Submitted to the Faculty of the
Graduate College of the
Oklahoma State University
in partial fulfillment of
the requirements for
the Degree of
DOCTOR OF PHILOSOPHY
July 2021

TERAHERTZ METAMATERIALS:

REFRACTIVE INDEX, SENSING, AND RESONANCES

Dissertation Approved:

Dr. Weili Zhang

Dissertation Adviser

Dr. Daqing Piao

Dr. John O'Hara

Dr. James Wicksted

Name: Leena Singh

Date of Degree: July 2021.

Title of Study: TERAHERTZ METAMATERIALS:

REFRACTIVE INDEX, SENSING, AND RESONANCES

Major Field: Electrical Engineering

Abstract: Engineering of high refractive index metamaterials at terahertz frequencies have been presented. Applications of terahertz metamaterials as sensor and polarization convertor have also been introduced. The metamaterials under study have been fabricated using conventional photolithography techniques in class 1000 cleanroom on free-standing, flexible substrates made of mylar/polyimide. The experimental investigations have been carried out with 8F confocal, photoconductive switch-based terahertz time-domain spectroscopy. All the simulation work has been carried out using commercially available software CST Microwave Studio and Matlab.

The main finding in this work is the deep sub wavelength coupling technique used to achieve high refractive index value of about 41.8 at 2.026 THz. This work also presents two simple linear equations utilized for further enhancement of the refractive index values at the desired terahertz frequencies. Despite the strong absorption terahertz frequencies in presence of water, this study successfully demonstrates the ability of terahertz metamaterials for sensing of chemical and biological samples in aqueous solution using terahertz spectroscopy systems with sensitivity as high as 305 GHz/RIU. A terahertz metamaterial-based polarization converter has also been presented. It demonstrates broad bandwidth and transmission efficiency as high as 80% by coupling multiple responses.

TABLE OF CONTENTS

Chapter Page

LIST OF FIGURES

Figure Page

LIST OF TABLES

Table Page

LIST OF SYMBOLS

μ	material permeability
ε	material permittivity
η	refractive index
α_1	angle of incidence
α_2	angle of refraction
ω_p	plasma angular frequency
n	carrier density
e	electron charge
m^*	effective mass of carrier
c	speed of light
σ	conductance
ω_0	angular frequency at resonance
β_{max}	propagation constant
k_0	wave number at resonance frequency
N	number of layers
L	inductance
C	capacitance
Γ	resistive damping factor

f	frequency
λ	wavelength
R	refraction coefficient
t	transmittance
r	reflectance
εr	relative permittivity
μr	relative permeability
$\varepsilon 0$	permittivity of free space
$\mu 0$	permeability of free space
$S21$	transmission S-parameter
$S11$	reflection S-parameter
W	dissipated energy
t	spacer thickness
$ADWR$	asymmetric double wire resonator
Φs	phases of the sample
Φr	phases of the reference
txy	cross-polarization transmission coefficient
rxx	reflection coefficient
Eyt	electric fields of the y-polarized transmission wave
Exi	electric fields of the x-polarized incident wave

E_{xr}	electric fields of x-polarized reflected wave
B_f	relative bandwidth
f_h	upper cutoff frequencies
f_l	lower cutoff frequencies
$T(\omega)$	normalized amplitude transmission
v	phase velocity

CHAPTER I

INTRODUCTION

Electromagnetic waves are present all around us, traveling at a constant speed, transmitting energy from one point to another. Humans can sense some of these electromagnetic waves as heat (760nm to 1mm), sound (14.9Mm to 17.6Km/20Hz-17kHz), or visible light (750nm to 380nm), but it requires special setup to sense/utilize the rest of the electromagnetic spectrum. Electromagnetic waves are produced by the vibration of charged particles which provide them with electrical and magnetic properties. Microwave, radar, x-ray, radio, and telecommunication are some of the technologies that utilize these properties. Electromagnetic waves with frequencies ranging from 1 to 10 THz are quite remarkable as they witness the breakpoint of both electrical and magnetic responses in most of the naturally occurring materials. Due to this reason, these frequencies remain least explored, creating what is known as the Terahertz gap. This slice of spectrum is most elusive due to the fact that these frequencies are powerful enough to penetrate through thick concrete walls and yet have no ionizing effect on biological cells, making them the best-suited frequency for many applications ranging from surveillance to biomedical devices.

One of the most used applications of these frequencies is Terahertz spectroscopy, a technique that allows the far-infrared optical properties of a material to be detected as a function of time. Figure 1.1 shows one of the terahertz

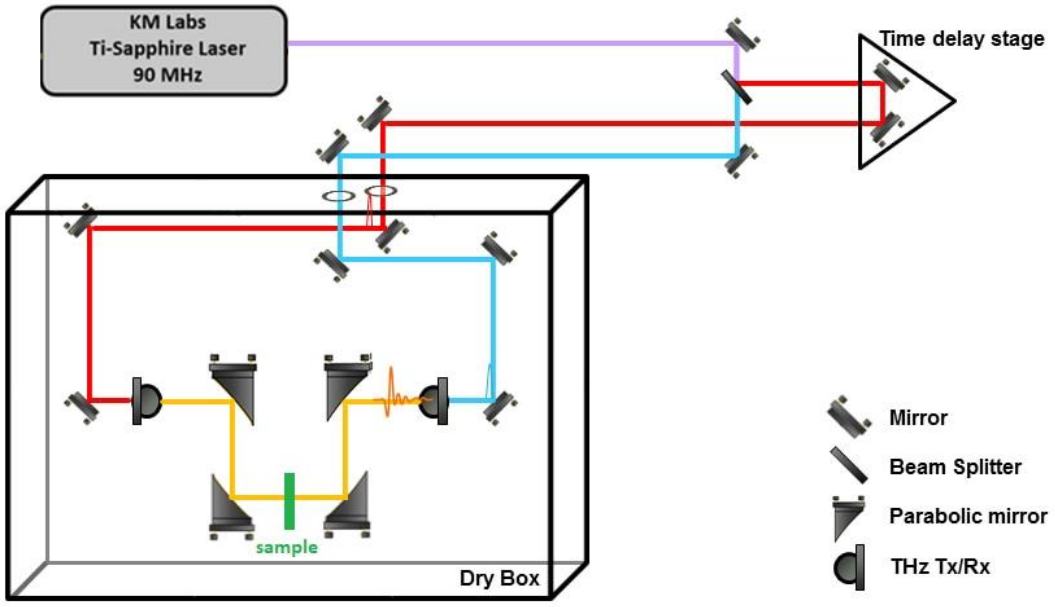

Fig. 1.1 8F confocal spectroscopy technique

A photoconductive switch-based terahertz time-domain spectroscopy system that consists of four confocal parabolic mirrors for obtaining a parallel beam front and a smaller beam waist at the sample and a time delay stage to control the precise timing at which the terahertz pulse reaches the receiver antenna.

spectroscopy setups that are used for sample characterization, An 8F confocal spectroscopy system. It is a photoconductive switch-based terahertz time-domain spectroscopy system that consists of four confocal parabolic mirrors for obtaining a parallel beam front and a smaller beam waist at the sample. The entire system is enclosed in a box and purged with dry air to eliminate the effect of water vapor at terahertz frequencies. Historically, terahertz spectroscopy was used for spectral characterization of the rotational and vibrational resonances and the thermal–emission lines of simple molecules[1]. THz spectroscopy has also been used to determine carrier concentration and the mobility of doped semiconductor materials such as GaAs and Si wafers [2-4] dielectric constants, and refractive index of thin films[5], as well as for the characterization of high-temperature superconductors. optical-pump THz-probe systems facilitated experimental evidence to quantum-kinetic theoretical predictions regarding charge build-up or dressed quasi-particles.[6] Terahertz frequencies are of especial interest to astronomy and space science due to their ability to extract material characteristics that other frequencies may not.[4]

Although terahertz technology had very diverse and attractive applications in the field of astronomy, semiconductor, medical-imaging, atmospheric studies, space-communication, defense, and so on, it remains the least developed region due to lack of materials responding to these frequencies[4, 7] By the end of 1999, advancements in microfabrication techniques have added ease to the fabrication of artificial media.[8] In addition to 3D structures, two-dimensional (2D) thin film, and structures with metallic components within the unit cells, metallo-dielectric structures have also begun to attract scientific attention, as the physics associated with the metallo-dielectric structures was quite unique and very different from the pure dielectric structures.[9] The term metamaterial was first defined by R.M. Welser in 2001 as “macroscopic composites having a man-made, 3D, periodic cellular architecture designed to produce an optimized combination, not available in nature, of two or more responses to a specific excitation. Each cell contains metaparticles, macroscopic constituents designed with low dimensionality that allow each component of the excitation to be isolated and separately maximized. The metamaterial architecture is selected to strategically

Permeability (μ) / Permittivity (ε)	$\mu >> 1$	$0 < \mu < 1$	$\mu < 0$
$\varepsilon >> 1$	Right-handed materials Forward propagating waves	Permeability (μ) near-zero (MNZ)	Magnetic Plasma Evanescent waves
$0 < \varepsilon < 1$	Permittivity (ε) near zero (ENZ)	Perfect tunneling effect	Permeability (μ) negative (MNG)
$\varepsilon < 0$	Electric Plasma, Evanescent waves	Permittivity (ε) negative (ENG)	Left-handed materials (DNG) backward propagating waves

Table 1.1. Possible combinations of refractive index metamaterial in ε-μ domain

All possible combinations of permeability and permittivity used to design refractive index metamaterials with desired properties.

recombine local quasi-static responses, or to combine or isolate specific non-local responses"[10]. The advent of metamaterials has proven to be especially valuable in the terahertz regime and was expected to close the "THz gap."[8] The capability to control electromagnetic waves inside an artificially designed material opened tremendous possibilities. The transmission of electromagnetic waves inside of any materials is basically defined by the permittivity (ε) and the permeability (μ) of the materials. Refractive index (η), another material property of interest, is defined by permeability and permittivity as:

$$\eta = \sqrt{\varepsilon\mu}\,. \qquad (1.1)$$

Materials with all the possible combinations of permeability and permittivity, as shown in table 1.1. now become possible.[11]

1.1 Index of refraction

The measures of the change in direction as well as the speed of the electromagnetic wave while passing from one medium to another with different permeability or permittivity or both is defined as the index of refraction. An electromagnetic wave traveling at an angle of α_1 w.r.t. the normal in medium with refractive index η_1, undergoes refraction at the medium interface and travels at an angle of α_2 w.r.t. the normal in medium with refractive index η_2.[8] According to Snell's law relation between the ratio of refractive indices of the two media and the ratio between the angle of incidence and angle of refraction is defined as:

$$\frac{\eta_1}{\eta_2} = \frac{\sin\alpha_2}{\sin\alpha_1}. \qquad (1.2)$$

Metamaterials with designer refractive index have been of much interest among the scientific community due to the various potential applications and capabilities made possible with them. As discussed earlier refractive index can also be defined as the square root of the product of material permittivity and permeability. In other words, the refractive

index is the property of the materials that define the amount by which the electrical and magnetic component of the electromagnetic waves deviates from its original direction at the interface of two media with different values of permeability and/or permittivity. It is worth noting that even though the refractive index is defined by both permeability and permittivity, both permeability and permittivity of the media act individually on the passing electromagnetic wave. Thus it is possible to design metamaterials with a specific value of the refractive index that can individually manipulate the propagation of either electrical or magnetic component of the electromagnetic wave based on the value of permeability and the permittivity of the material designed. The index of refraction can be engineered based on the following categories:

1. High refractive index metamaterials with
    1.1. Higher permeability ($\mu >> 1$)
    1.2. Higher permittivity ($\varepsilon >> 1$)
    1.3. Both permeability and permittivity have higher positive values ($\mu, \varepsilon >> 1$)
2. Negative refractive index metamaterials with
    2.1. Permeability negative ($\mu < 0$)
    2.2. Permittivity negative ($\varepsilon < 0$)
    2.3. Both permeability and permittivity negative ($\mu, \varepsilon < 0$)
3. Near-Zero refractive index metamaterials with
    3.1. Permeability positive and near-zero ($0 < \mu < 1$)

3.2. Permittivity positive and near-zero ($0 < \varepsilon < 1$)

3.3. Both permeability and permittivity positive and near-zero ($0 < \mu, \varepsilon < 1$)

1.2 High Refractive Index Metamaterials

Materials with an enhanced index of refraction are much desired for laser particle acceleration in the field of lithography, imaging, optical communications, atomic tests of electroweak particles, solar devices, magnetometry, and many more. An electromagnetic wave entering a material with a higher refractive index at some angle w.r.t. the normal tends to bend towards the normal in the materials with a higher refractive index. The higher the refractive index, the more bending towards the normal.

Initial attempts to achieve higher refractive indices involved the use of atomic resonances, coherent quantum systems, and photonic bandgap materials.[8] With the prevalence of the concept of metamaterials, a metal film with subwavelength periodic 1D cut through slits was used to demonstrate achievement of higher refractive index as well a means to control refractive index by controlling geometric parameters of the structure. With careful selection of the geometric parameters of the subwavelength cut through slits in a high purity copper film, an effective refractive index of about 5.51 was achieved at terahertz frequencies.[12]. Recently, deep subwavelength coupling technique is used to achieve a record-breaking high index of refraction of about 41.8 at 2.06 THz.[13] A detailed discussion of the various techniques and metamaterial structures used to achieve higher index of refraction is presented in chapter 2.

1.3 Negative Refractive Index Metamaterials (NRM)

A Negative refractive index metamaterial(NRM) is an artificial material with a negative effective refractive index created by subwavelength unit cells that can be considered homogenous. Figure 1.2 depicts an electromagnetic wave

incident on the flat surface of negative index metamaterial from a point source. The artificial materials crafted to achieve both permeability and permittivity values to be negative simultaneously are often referred to as Double Negative metamaterials(DNM) in literature. At a given wavelength range, negative permeability (μ) and permittivity (ε) can be written as $\mu = |\mu| \exp(i\pi)$, and $\varepsilon = |\varepsilon| exp(i\pi)$, hence refractive index, $\eta = \sqrt{\varepsilon\mu}$,

$$\eta = \sqrt{|\mu||\varepsilon| exp(2i\pi)}, \quad (1.3)$$

$$\eta = \sqrt{|\mu||\varepsilon|}\,.exp(i\pi), \quad (1.4)$$

$$\eta = -\sqrt{|\mu||\varepsilon|}\,, \quad (1.5)$$

i.e., the refractive index of the medium with simultaneously negative permeability and permittivity must be negative.[14]

Metals show negative permittivity below their plasma frequency, and thus arrays of conducting wires, as shown in figure 1.3, have been used to achieve negative permittivity values in metamaterials. [15] . The generic frequency dependent permittivity has the form

$$\varepsilon(\omega) = 1 - \left(\omega_p^2\right) / (\omega^2 - \omega_0^2 + i\omega\Gamma), \quad (1.6)$$

where the plasma frequency, ω_p^2 , is

$$\omega_p^2 = 4\pi(n_e^2 / m^*), \quad (1.7)$$

and n is the carrier density, e is the charge of an electron, and m* is the effective mass of carriers.([15]) In the case of metamaterials, both n and m* are defined by their unit cell structure, and thus metal structures are used at their plasma frequency and thereby achieve negative permittivity at the frequency of interest. For the structure shown in figure 1.3, plasma frequency is given as

$$\omega_p^2 = \frac{2\pi c^2}{a^2\, ln(a/r)}. \qquad (1.8)$$

And the effective permittivity is given as

$$\varepsilon_{eff} = 1 - \frac{\omega_p^2}{\omega[\omega - i(\omega_p^2 a^2 \varepsilon_0)/\sigma\pi r^2]} \approx 1 - \frac{\omega_p^2}{\omega^2}. \qquad (1.9)$$

For $\omega < \omega_p$, effective permittivity becomes negative, assuming conductance $\sigma \to \infty$.[14]

As far as negative permeability is concerned, there is no known natural material that shows permeability below zero. It is only with the advent of metamaterial that negative permeability becomes achievable. Split ring resonators (SRR) shown in Figure 1.4 (left) and swiss roll structures shown in Figure 1.4 (right) are most commonly used to achieve negative permeability.

It is known that the inductance of the unit cell structure is usually responsible for the magnetic response of the metamaterial. According to Faraday's law, when a time-varying magnetic field is applied perpendicular to a coil surface, the induced current is generated in the wires of the coil. Metamaterial unit cell structures direct the induced currents to provide desired inductance to the structure and, in turn, provides a method for steering the effective metamaterial permeability towards positive or negative values

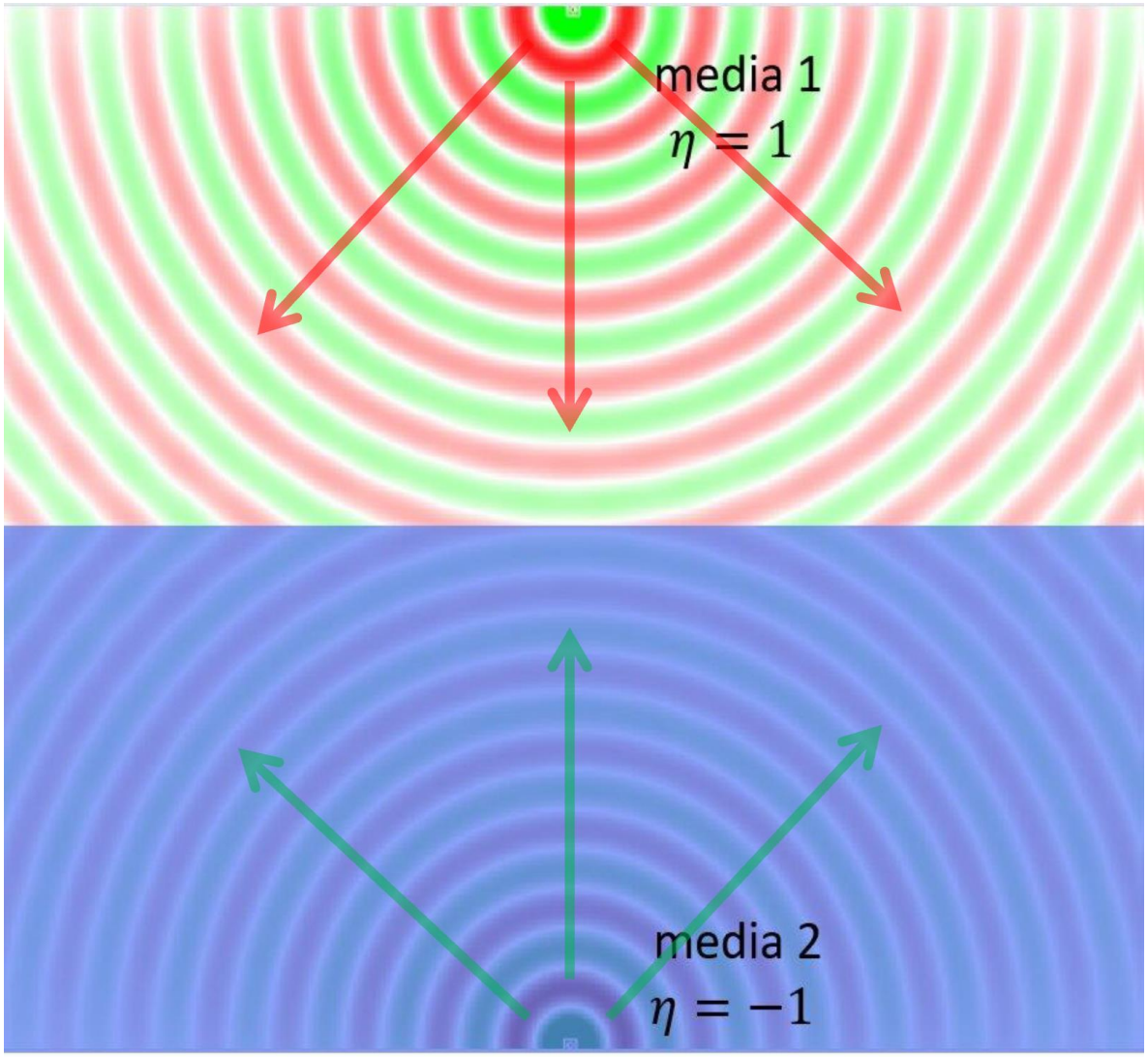

Fig. 1.2. Negative Refraction

Normally incident electromagnetic waves originating from a point source experiencing negative refraction at the boundary of NRM.

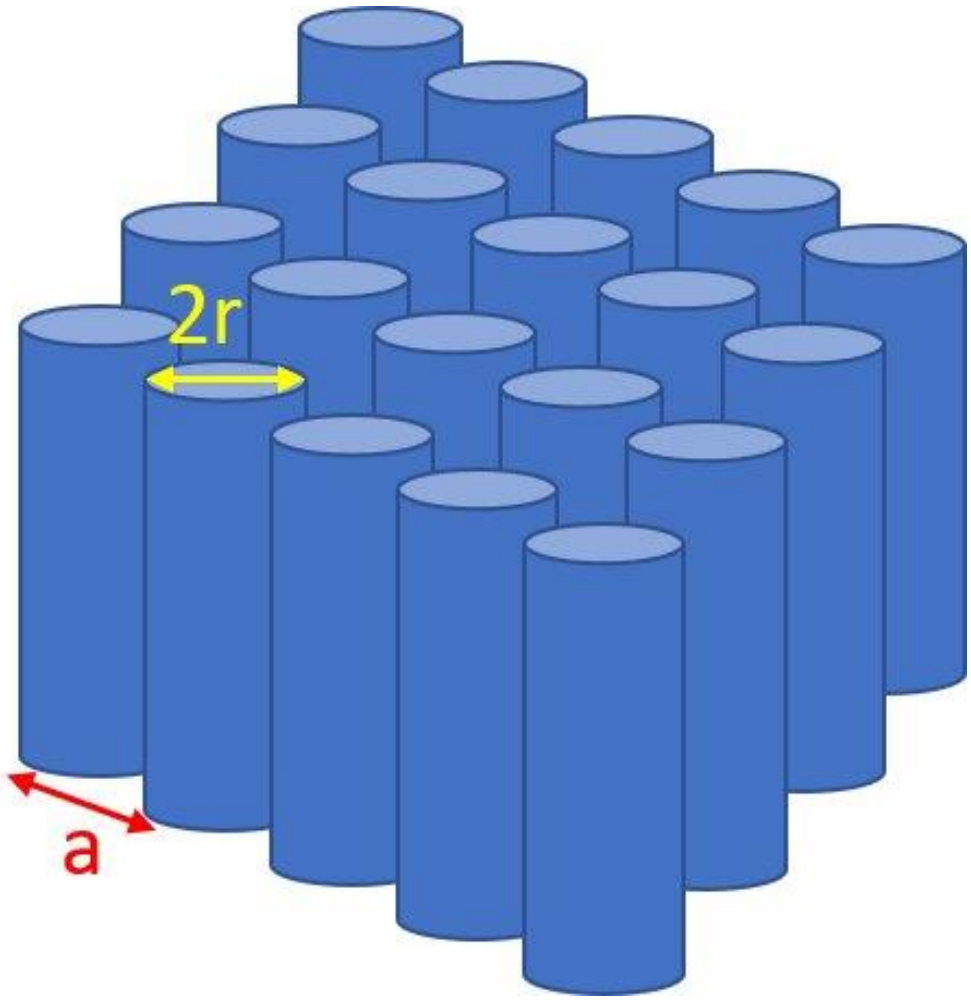

Fig. 1.3. Wire Array

An array of conducting wires for achieving negative permittivity

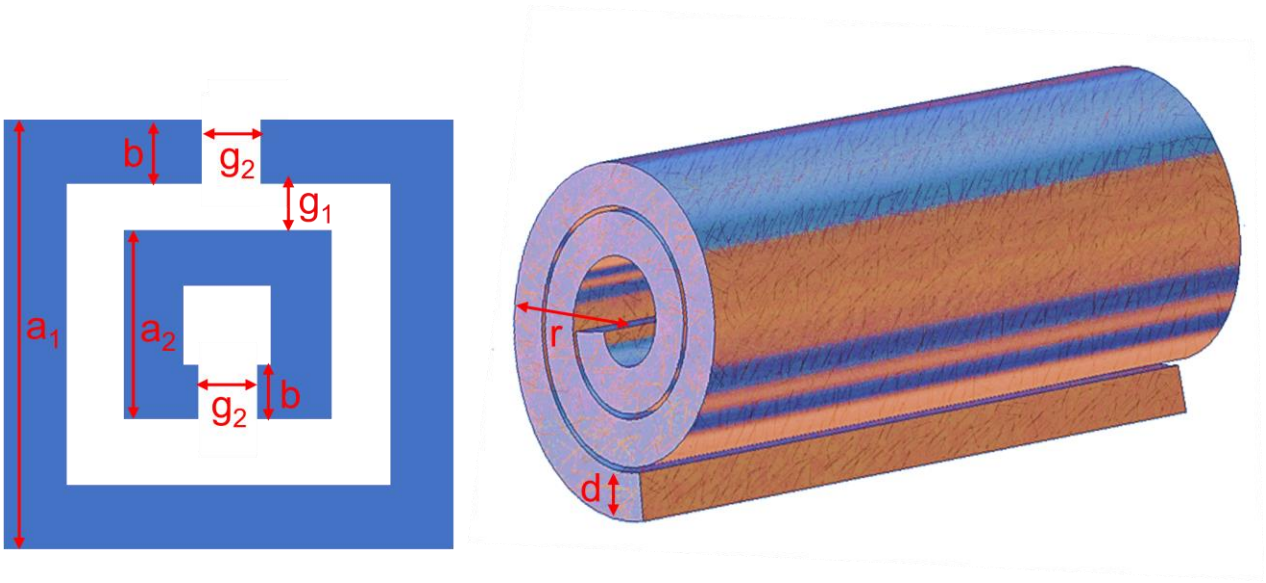

Fig. 1.4. SSR and Swiss Roll

Structures that can achieve negative permeability, split-ring resonator(right), and swiss-roll structure(left)

For the SSR structure, The time-varying magnetic field induces a current in the resonator arms, making it behave like an inductor. The circulating current in the SSR arms builds up change across the resonator gap, transforming the gap into a capacitive element. Thus the SSR structure behaves like an LC circuit, whose resonance frequency can be written as:

$$\omega_0 \sim \sqrt{1/LC}. \qquad (1.10)$$

For frequency above ω_0 the SSR provides positive inductance, while at frequencies below ω_0 the structure provides a negative response. [15]

The effective frequency dependent permeability of the SSR unit cell is expressed as [15]:

$$\mu_{eff}(\omega) = 1 + (F\omega^2) \,/\, (\omega_0^2 - \omega^2 - i\Gamma\omega). \qquad (1.11)$$

In the swiss roll structure, the induced current produced due to the time-varying magnetic field applied parallel to the common axis flows by charing the capacitance between the inner and the outer side of the metal sheet.[16] The system starts behaving like magnetic pole plasma and provides negative permeability to the structure in some frequency range.[16]

For the Swiss roll structure, the frequency dependent anisotropic permeability is expressed as[17]:

$$\mu_z(\omega) = 1 - \frac{F}{\left(1 - {\omega_0^2}/{\omega^2}\right) + i({\Gamma}/{\omega})}, \mu_x = \mu_y = 1, \qquad (1.12)$$

where F is the geometrical factor, ω_0 is the resonant frequency, and Γ is the resistive damping factor. Metamaterials with both permeability and permittivity less than zero have certain unique characteristics. The phase velocity, doppler shift, directions of Cherenkov radiations as well as radiation pressure inside these materials are reversed.[16] D.R.

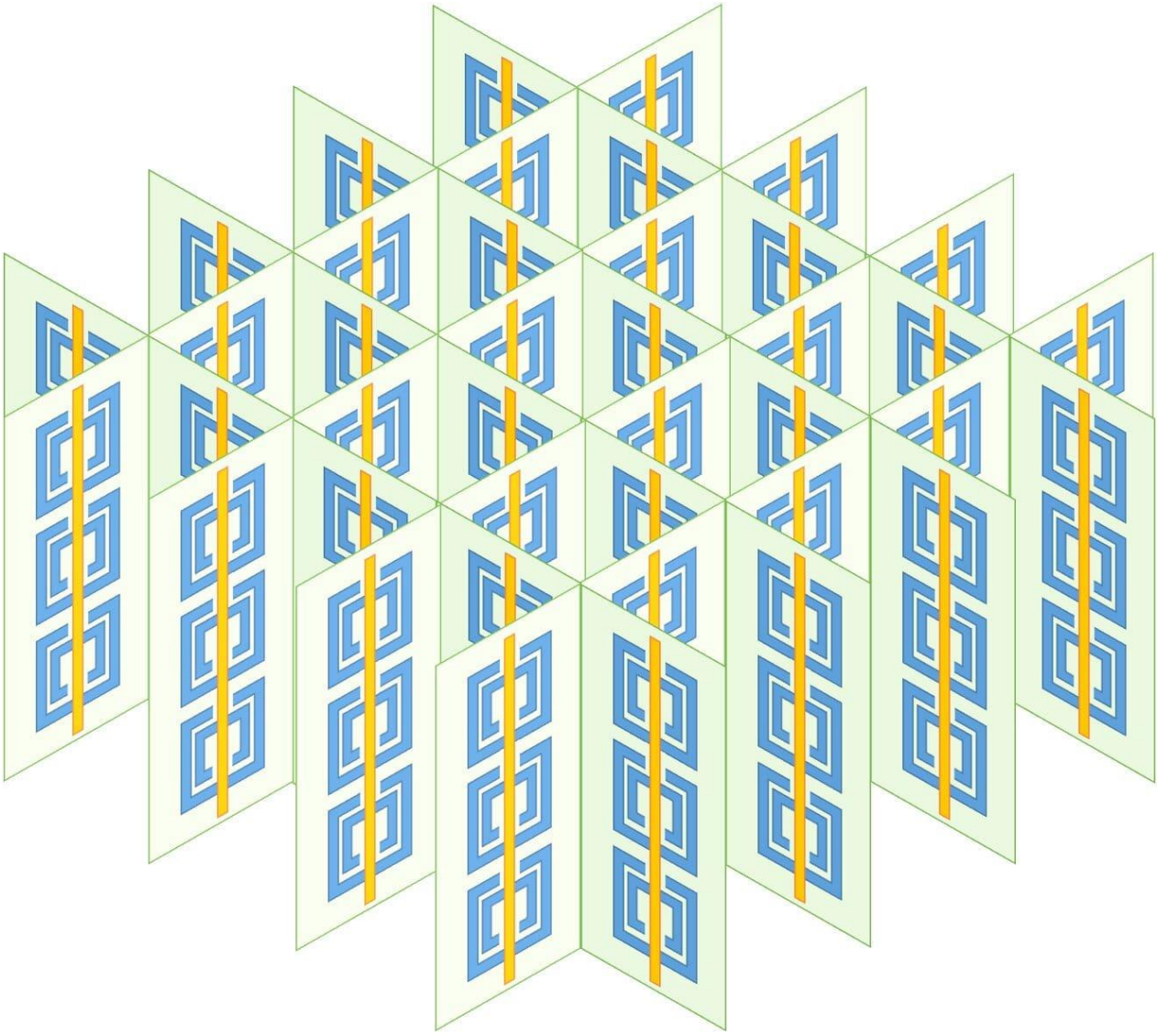

Fig. 1.5. Negative index metamaterials

Schematic of the metamaterial fabricated to demonstrate of double negative refractive index

Smith and et al. conceived a metamaterial unit cell design to achieve a double negative refractive index [18] by using a combination of two structures, an array of wire to achieve negative permittivity and an SSR unit cell structure to acquire negative permeability over the same frequency band. This structure was then experimentally verified by Shelby et al. in 2001 at microwave frequencies. Figure 1.5 shows a schematic of the fabricated metamaterial consisted of split-ring resonators on interlocking strips of the standard circuit board and a two-dimensional array of copper strips[19]. Some of the metamaterials with a double negative refractive index at terahertz frequencies utilized a similar combination of planar SSR structure and the cross wire to achieve negative refraction at around 2 THz [20],[21], and 4.9 THz[22].

1.4 Near-Zero refractive index metamaterials

Materials with refractive index values between 0 to 1, i.e., the refractive index is positive but less than 1, are generally classified as near-zero refractive index materials. Electrometric fields in these media are static in space (for $n = 0$) but remain dynamic in time. The wavelength(λ) and the frequency(f) of an electromagnetic wave traveling inside amedium are correlated to each other via phase velocity(ν), which in turn is defined by the material properties, permeability(μ) and permittivity(ε) of that medium as below[2]:

$$\nu = f.\lambda, \qquad (1.13)$$

$$\nu = \frac{1}{\sqrt{\varepsilon\mu}}. \qquad (1.14)$$

In equation (1.14), when either permeability (μ) or permittivity (ε) of the medium approaches zero, the phase velocity becomes infinity, the phase of the electromagnetic wave appears to be fixed. This high value of phase velocity, when substituted in equation (1.13), results in a very high wavelength at high frequencies. The unique properties offered by near-zero refractive index metamaterial have great potential in realizing energy tunneling, directional emission, and

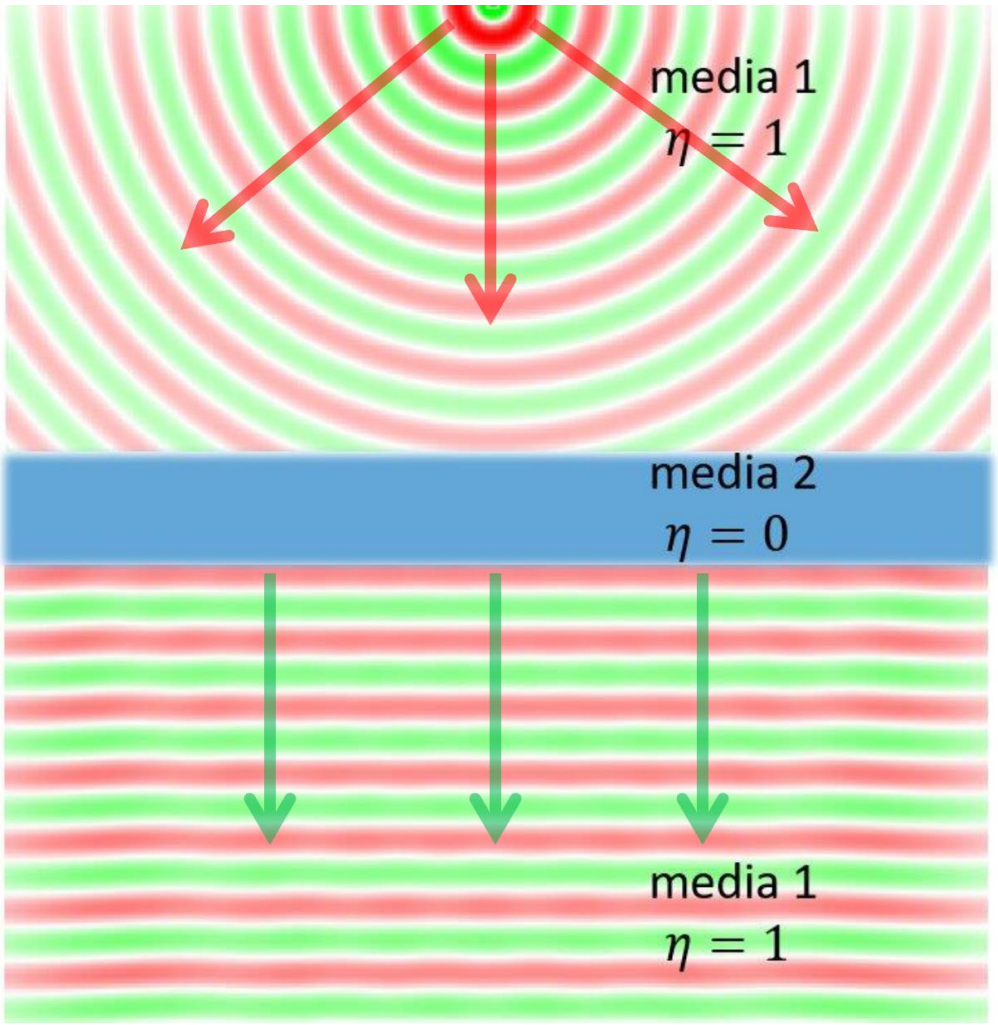

Fig. 1.6. Zero index of refraction

Electromagnetic waves originating from a point source experiencing refraction when incident normally at a slab with zero refractive index

beam focusing effects. Figure 1.6 depicts the electromagnetic waves from a point source incident normally on a near-zero refractive index slab undergoing refraction.

When an electromagnetic wave is incident on a near-zero refractive index slab at a non-zero angle wrt to the normal, the beam exiting from the slab attains planar wavefront. This can be explained by Snell's law, as stated in equation (1.2).When η_1 attains a near-zero value, α_2 becomes zero, aligning the electromagnetic waves along the normal axis.[23]

As per Drude's model, the frequency specific permittivity (for metal or heavily doped semiconductors) can be written as:

$$\varepsilon(\omega) = \varepsilon_\infty \left(1 - \frac{\omega_p^2}{\omega^2 + i\omega\Gamma}\right), \qquad (1.15)$$

where Γ is loss constant, ω_p is plasma frequency, and ω is angle frequency [23]. In equation (1.15), when Γ becomes small and ω_p approaches ω, the value ε (ω) gets close to zero. In fact, many materials exhibit near-zero permittivity values at their plasma frequencies, such as potassium at terahertz frequencies and silicon carbide at mid-infrared frequencies, aluminum-doped zinc oxide (AZO) and ITO at near-infrared frequencies, and $Bi_{1.5}Sb_{0.5}Te_{1.8}Se_{1.2}$ (BSTS) exhibit an ENZ response at ultraviolet frequencies[24].

Materials with near-zero permeability, and especially materials with both permeability and permittivity near zero at the same frequency range, are not readily available in nature. Hence, artificial materials designs become necessary to harness all the exciting possibilities offered by near zero-index material. Metamaterials with near-zero refractive can be realized either by making permittivity or permeability or both near zero.

Material permeability and permittivity, in turn, affects the refractive index, wave impedance and reflection coefficient of the metamaterial as specified by below equation (1.16),(1.17) and (1.18):

$$\textit{Refractive index, } \eta = \sqrt{\varepsilon . \mu}\,, \qquad (1.16)$$

$$\textit{Wave impedance, } z = \sqrt{\mu / \varepsilon}\,, \quad (1.17)$$

$$\textit{Reflection coefficient, } R = (z - z_0) / (z + z_0). \quad (1.18)$$

The three possible cases for achieving refractive index values near zero can be defined as following:

CASE 1: $\varepsilon \rightarrow 0$, $Z \rightarrow \infty$, $R \rightarrow +1$

Perfect magnetic conductor(PMC)

When the permittivity of a material attains near-zero value, the refractive index of the materials tends to zero, wave impedance approaches to infinity, and the reflection coefficient becomes unity. Such materials are also known as perfect magnetic conductors or PMC.

CASE 2: $\mu \rightarrow 0$, $Z \rightarrow 0$, $R \rightarrow -1$

Perfect electrical conductor(PEC)

When the magnetic permeability of the material reaches zero, this results in a zero or low index of refraction as well as near-zero wave impedance. The reflection coefficient of the materials tends to negative 1. Such materials are known as perfect electrical conductors or PEC.

CASE 3: $\varepsilon, \mu \rightarrow 0$, $Z \rightarrow Z_0$, $R \rightarrow 0$

Impedance matched materials

The third case is when both dielectric permittivity and magnetic permeability simultaneously accomplish zero or near-zero values, the reflection coefficient of such materials tends to zero. The refractive index tends to be zero while the wave impedance becomes equal to that of free space. Hence, these are also known as impedance-matched metamaterials.

A double-sided paired cut wire structure [25], as shown in Figure 1.7, demonstrated near-zero refractive index at terahertz frequencies with both permeability and permittivity values approaching near zero. The electric field of the electromagnetic waves propagating parallel to the cut wire pair imparts dielectric properties to the metasurface. At the resonance frequency, this dielectric property that in turn is responsible for the permittivity of the metamaterial changes value from negative to positive. The metasurface attains zero relative permittivity value while transitioning from negative to positive resonance.

Due to the magnetic field of the electromagnetic waves propagating perpendicular to the metasurface, the double-sided paired cut wire structure behaves as minuscule induction elements. Thus, providing the magnetic resonance to the structure, which changes value from positive to negative at the resonance frequency and is responsible for relative permeability of the metamaterial. The metamaterial acquires zero permeability value while the magnetic resonance moves from negative to positive domain. Thus the above-shown metasurface becomes capable of achieving near-zero values for both permeability and permittivity, subsequently realizing zero refractive index value. The metasurface demonstrates a refractive index value of $0.16 + j0.09$ at 0.505 THz with relative permittivity of $0.18 + j0.10$ and relative permeability of $0.004 + j0.16$.[25].

1.5 Summary

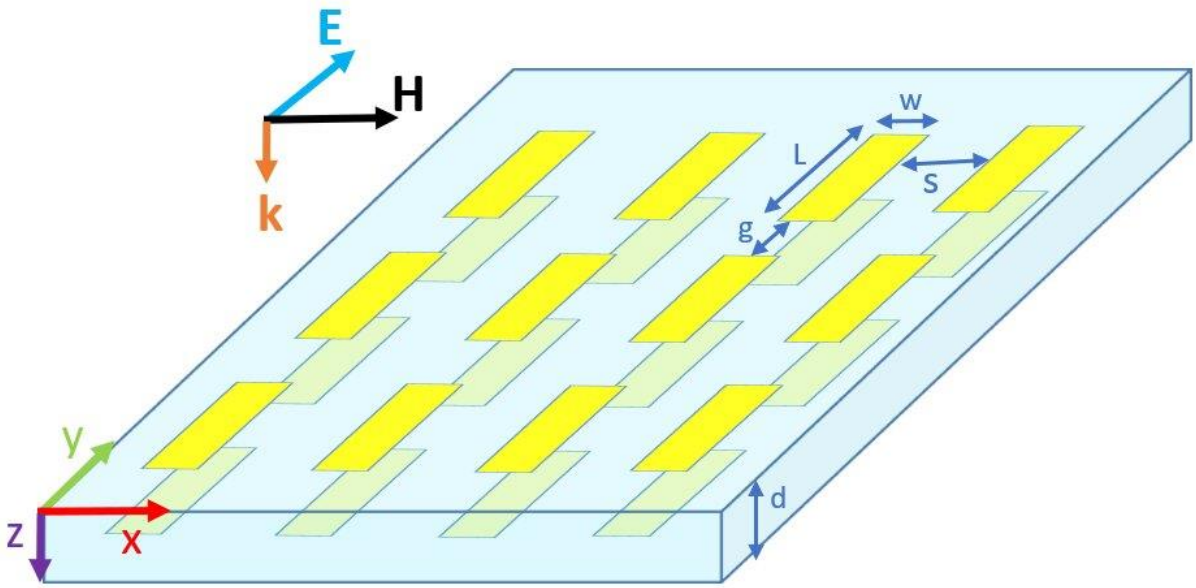

Fig. 1.7. Zero-Index Metamaterials

Schematic of the metasurface with near-zero refractive index at terahertz frequencies.

In this chapter, we presented a conceptual overview of different types of refractive index possibilities and design mechanisms at terahertz frequencies. Different types of meta-atom structures that have been used over the past year to achieve designer refractive indices have also been discussed briefly. The capability to control the electromagnetic waves, especially electrical and magnetic components, separately is not only riveting but also crucial to study and understand many physical and quantum processes. Many applications that have only been theoretically conceptualized so far now become possible with the advent of metamaterials. The ability to harness the full potential technological applications promised by terahertz frequencies has long remained a challenge due to the lack of the necessary availability of workable natural materials itself. Designer refractive index metamaterials are one of the many essential fields of study towards closing this terahertz gap. Many advancements have been made not only to achieve the required (high, negative, or zero) refractive index but also to dynamically control their values. Meta atoms that can dynamically change refractive index values from positive to zero and to negative with the help of optical, electrical, or stress as stimuli have been studied. Various new applications like performing mathematical functions with designer refractive indices metamaterial, advanced antennas, electromagnetic tunneling, sensor, cloaking, and so on have already been presented in scientific literature.

ACKNOWLEDGEMENT: This chapter is due publication as book chapter, " L. Singh and W. Zhang, Terahertz index of refraction engineering, World Scientific, 2021".

CHAPTER II

ADVANCEMENTS IN HIGH REFRACTIVE INDEX MEDIA: FROM QUANTUM COHERENCE IN ATOMIC SYSTEM TO DEEP SUB-WAVELENGTH COUPLING IN METAMATERIALS:

Refractive index enhancement is crucial in the fields of lithography, imaging, optical communications, solar devices, and many more. In this chapter, I will be presenting a review of the advancements in the process of designing high refractive index metamaterials, starting from quantum coupling and photonic bandgap materials to metamaterials utilizing deep subwavelength coupling to achieve ever-high values of refractive index. The understanding of the evolution of material design from intrinsic electronic states manipulation to meta-atoms design is not only fascinating but also a prerequisite to developing successful devices and applications. A particular attention is given to experimentally verified schemes in engineering a high index of refraction. This would enhance our understanding of the various schemes that were successfully verified for refractive index enhancement and thus help us find our path forward.

2.1 Snell's Law

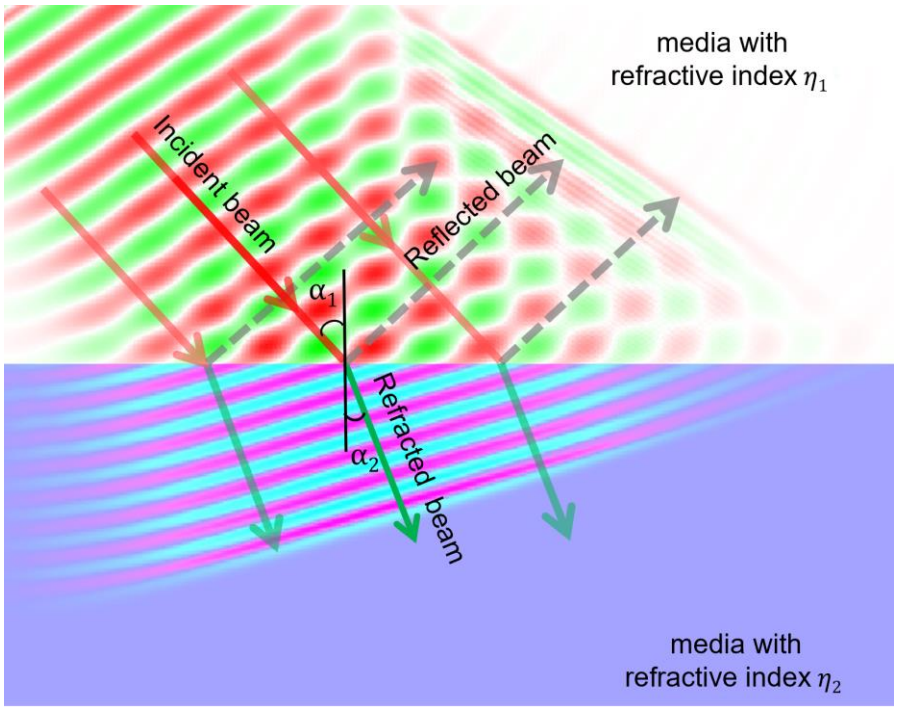

Fig. 2.1. Bending to an electromagnetic wave

Bending to an electromagnetic wave while passing from one medium to another with different refractive indices. An electromagnetic wave travelling at an angle of α_1 w.r.t. the normal in medium with refractive index η_1, undergoes refraction at the medium interface and travels at an angle of α_2 w.r.t. the normal in medium with refractive index η_2.

Humans have been using materials with various refractive indices for visible light manipulation for centuries. An impressive application of modified refractive index can be found in the form of well-known stained glass art window as found in the 13th century Notre Dame Cathedral in Paris. When an electromagnetic wave hits the boundary of two mediums with different refractive indices, a part of the incident wave is send back to its original direction(medium), known as reflected wave, and the other part passes through the second medium known as refracted wave. The part of the EM wave that enters through the second medium may witnesses change in speed, wavelength, and direction of travel depending on the properties of the two media. Refractive index is basically defined as a dimensionless quantity, which measures the bending of the electromagnetic wave while passing from one medium to another, Fig. 2.1 shows the refraction of a plane monochromatic EM wave while passing from a medium with refractive index η_1 to another medium with refractive index η_2.

By 20th century, a number of scientific journals had already been discussing the potential applications of high refractive index media for laser particle acceleration[26, 27], optical microscopy[28], atomic tests of electroweak physics[29] and magnetometry[30].

2.2 High refractive index via quantum coherence

A wide variety of materials with different refractive indices already exists in nature. But being able to create a material with required refractive index for a specific wavelength/frequency was necessary for various applications. In 1991, O. Scully presented the possibility of achieving a high refractive index without high absorption via quantum coherence, in principle for the first time[30]. Index enhancement was accomplished by choosing to operate near an atomic resonance between a coherent ground-state doublet configuration $|b\rangle$ and $|b'\rangle$ and an excited state $|a\rangle$ with level

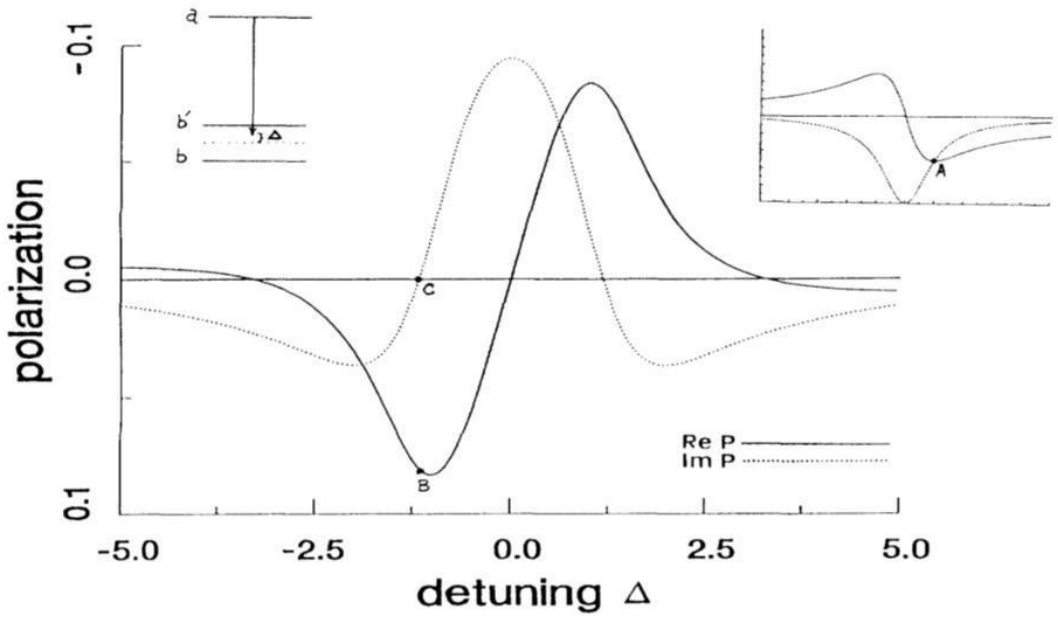

Fig. 2.2. Dispersive (ReP) and absorptive (lmP) parts of polarization

Dispersive (ReP) and absorptive (lmP) parts of polarization vs detuning of radiation frequency from midpoint between level b' and b. Polarization plotted on arbitrary scale, and detuning Δ, plotted in units of atomic decay. Inset, upper right-hand corner: Usual dispersion-absorption curve. Inset, upper left-hand corner: Present level scheme. *[Reprinted with permission from "Scully, M.O., Enhancement of the index of refraction via quantum coherence. Phys. Rev. Lett. 1991, 67(14): p. 1855-1858". Copyright (1991) by the American Physical Society].*

---

probabilities ραα, α = a, b, c along with an appropriately chosen atom-field detuning[30]. The result is shown in Fig. 2.2. The normal case of resonant dispersion is shown in upper right-hand corner inset in Fig. 2.2, the maximum refraction (Re*P*) is marked with point *A*, the absorption (Im*P*) is also large at this point. However, when there is coherence between the lower levels *b'* and *b*, the dispersion can be large (point *B*) with a near zero absorption marked as point *C*. Coherence between levels b' and b can be achieved by a number of techniques, i.e., pulse[31], microwave[32] or Raman technique[33, 34]. In 1992, M. Fleischhauer, et al. presented a detailed survey of various schemes in which atomic coherence and interference effects lead to complete absorption cancellation and an ultrahigh index of refraction[35]. In 1996, Zibrov, et al presented proof-of-principle experiment demonstrating resonantly enhanced refractive indexand reduced absorption achieved by quantum coherence in Rb vapor[36]. A resonant change of about 10^{-4} was observed in the refractive index.

2.3 Photonic bandgap materials for refractive index enhancement

In 1994, J. Dowling, et al. proposed photonic bandgap materials as a possible candidate to achieve high index of refraction and presented a quantitative study explaining the anomalous index of refraction in photonic band gap materials[37]. It has already been established that a carefully chosen periodic dielectric lattice may exhibit frequency bandgaps for all photon polarizations and directions of propagation[12]. His study was based on the one-dimensional (1D) periodic dielectric array that was used to model a three-dimensional photonic bang gap material, to enhance the effective refractive index. He explained that near the gap in the photonic band gap materials the effective index of refraction can become less than unity and in fact can approach zero at the band edge itself-leading to ultra-refractive optical effect[37]. Given that refractive index of a system is the ratio n1/n2, his scheme was based on decreasing n2 instead of increasing n1, to obtain high effective refractive index[37]. In order to consider a three dimensional structure analytically as a one-dimensional problem it was assumed that the photons always encounter the same periodic index variation irrespective of the propagation direction or polarization. Such a periodic array is shown in Fig. 2.3 (a). Fig

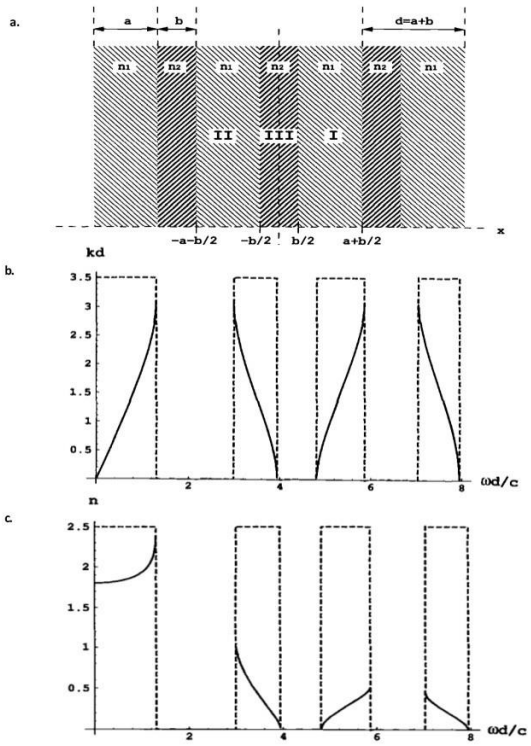

Fig. 2.3. The dispersion and the effective index of refraction for a three-dimensional photonic band gap material

(a) one-dimensional periodic dielectric array used to model a three-dimensional photonic bandgap material. The alternating dielectric regions of indices n_1 and n_2 have width a and b with $d = a + b$ the lattice period. The dispersion relation, $\omega = \omega(k)$,can be obtained by ensuring that the first and second derivative of the modal functions $a_k(x)$, are continuous across the I-III and III-II interfaces, and by invoking Block's theorem. (b) Choosing $n_1 = 1.0$, $n_2 = 4.0$, and $b/d = 0.85$ as our lattice parameters we plot here the dispersion relation, in form $k(\omega)d$ and $\omega d/c$. (c) plot of effective refractive index.

2.3(b) depicts *kd* versus *ωd/c* plot. Note that the phase velocity $v_\emptyset = \omega/k$ approaches infinity at the three band edges, where $kd \to 0$ and *ωd/c* is approximately 4.0, 4.8 and 8.0 respectively. Since the index of refraction is defined as $n = c/v_\emptyset$, this implies that $n \to 0$ at these points[12]. Fig 2.3(c) shows the plot of effective refractive index, $n_{eff}(\omega) = c/v_\emptyset$ versus *ωd/c* , depicting that the effective index of refraction is substantially zero at the frequencies near the band edges where *ωd/c* = 4.0, 4.8 and 8.0.

2.4 Metamaterials for refractive index enhancement

By the end of 1999, advancements in microfabrication techniques have added ease to the fabrication of artificial media. In addition to 3D structures, two-dimensional (2D) thin film and structures with metallic components within the unit cells, metallo-dielectric structures have also begun to attract scientific attention, as the physics associated with the metallo-dielectric structures was quite unique and very different from the pure dielectric structures[38]. In 2001, the term metamaterial was first defined by R.M. Welser as "macroscopic composites having a man-made, 3D, periodic cellular architecture designed to produce an optimized combination, not available in nature, of two or more responses to a specific excitation. Each cell contains metaparticles, macroscopic constituents designed with low dimensionality that allow each component of the excitation to be isolated and separately maximized. The metamaterial architecture is selected to strategically recombine local quasi-static responses, or to combine or isolate specific non-local responses"[39]. Every material consists of molecules and atoms, these act as building blocks for the material and are responsible for defining material behaviour toward EM waves. The ingenious idea that we can create artificial atoms (meta-atoms) which then act as unit cells for the artificial material(metamaterials), thus providing complete control over the of the material behaviour towards the EM waves is quite intriguing. This capability that we can design a unique structure with specific resistance, inductance and conductance and use either one or a combination of such structure to be periodically repeated to form an artificial material with pre-defined response towards the electrical and magnetic components of the EM wave soon attracted enormous attention for designing materials with high refractive

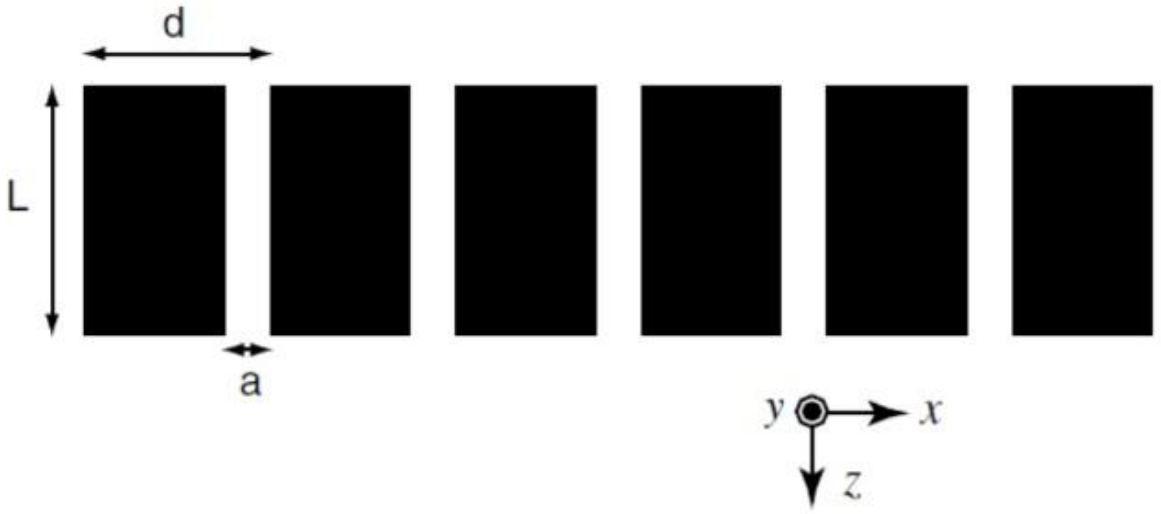

Fig. 2.4. Schematic of the metal film with periodic slits.

The parameters are defined as in the figure: *a* is the width of the slit, d is the periodicity, and L is the thickness of the metal film. The black regions indicate the metal parts, and the white regions are the vacuum. The film is extended in the *x-y* plane. *[Reprinted with permission from "Shen, J.T., P.B. Catrysse, and S. Fan, Mechanism for designing metallic metamaterials with a high index of refraction. Phys. Rev. Lett. 2005, 94(19): p. 197401". Copyright (2005) by the American Physical Society]*.

---

index, higher than any naturally existing material, negative refractive index, phase change, filters, and many more applications.

In 2005, J.T. Shen, et al. explained the mechanism for designing a high refractive index metallic metamaterial. Shen claimed that a metallic film with periodic 1D cut through slits, can be considered as a dielectric slab with an effective refractive index, n and width, L, as shown in Fig. 2.4[40].

The effective "n" is determined by field comparison between the metallic film with periodic cut through the slits and the dielectric slab. Given the periodicity of the slits in the metallic film is smaller than the wavelength, the zeroth order transmission amplitude of a TM wave normally incident on the metallic film can be written as[40],

$$t_0 = \frac{4[(f/\emptyset^2)/(1+1/\emptyset^2)]e^{-i(\omega/c)L}}{1-[(1-1/\emptyset)/(1+1/\emptyset)]^2 e^{2i(\omega/c)L'}}, \qquad (2.2)$$

where, $f = a/d$ is the filling factor of the slit, and $\emptyset = \sum_{p=-\infty}^{\infty} f g_0^2 \frac{w/c}{\propto_0}$, for normal incidence, $g_0 = 1$ and $\propto_0 = w/c$. When a plane is normally incident on a dielectric slab with refractive index n, the transmission amplitude can be written as:

$$t = \frac{4[n/(1+n^2)]e^{-in(\omega/c)L'}}{1-[(1-n)/(1+n)]^2 e^{2in(\omega/c)L'}}. \qquad (2.3)$$

Comparing equations (2.2) and (2.3), both transmission amplitudes t_0 and t, can be approximately equalized by setting $n = 1/\emptyset$ and $L' = L/n$[40]. With the transmission equivalence set up and establishing effective refractive index as $n = d/a$, which is defined only by the geometry of the structure. Shen, et al. pointed that refractive index of a media can be enhanced without having to change the intrinsic electronic states of the material. The paradigm of high refractive index media design is now shifting towards controlling the behavior of the electromagnetic waves by virtue

of structural geometry of the artificial media, so as to achieve desired materials parameters namely, permeability and permittivity, rather than meddling with the atomic states of the media.

2.5 Terahertz frequencies and high refractive index metamaterials

The range of frequencies from 1 to 3 THz is extremely fascinating as it witnesses the breakpoint of both electrical and magnetic response in most of the naturally occurring materials. Terahertz regime is the slice of the spectrum that lies between infrared and microwave radiations. These frequencies are capable enough to penetrate through thick concrete walls making them very attractive for security screening application and having no ionizing effect making them very safe to be used for medical applications. In spite of the fact that, terahertz frequencies had very diverse and attractive applications in the field of astronomy, semiconductor, medical-imaging, atmospheric studies, space-communication, defense and so on, it remains the least developed region due to the lack of materials responding to at these frequencies[4, 7]. The advent of metamaterials has proven to be especially valuable in the terahertz regime and expected to close the "THz gap". Following the same structure of metallic film with periodically arranged cut through slits, theoretically conversed by J.T. Shen, et al., A. Pimenov and A. Loidl performed the first experimental demonstration for a high refractive index metamaterial at terahertz frequencies in 2006[12]. A terahertz high refractive index metamaterials was fabricated with high purity copper plates with periodic slits[12]. A Mach-Zehnder interferometer arrangement[41] was then used to carry out the experiment for the frequency range 60 to 380 GHz, and the reflectance $R = |r|^2$ and complex transmittance $\sqrt{T}e^{i\emptyset}$ were measured. The effective parameters of the sample were obtained using Fresnel optical formulas for reflectance and transmittance, using following equations:

$$t = \frac{(1-r_0^2)t_1}{1-r_0^2 t_1^2}, \qquad (2.4)$$

$$r = \frac{(1-t_1^2)r_0}{1-r_0^2 t_1^2}. \qquad (2.5)$$

Here, $r_0 = (n-1)/(n+1)$ and $t_1 = \exp(2\pi i n L/\lambda)$, r_0 is the reflection amplitude at the air-sample interface, t_1 is the "pure" transmission amplitude, n is the complex refractive index, L is the sample thickness, and λ is the radiation wavelength[12]. An effective refractive index 5.51 was obtained and an additional correction $\emptyset_{corr} = 2\pi(L - L_{eff})/\lambda$ was suggested to be added to the experimentally obtained phase, in order to establish the equivalence to the real dielectric slab. This metal-dielectric interface can support surface plasmon waves in the optical regime.

The dispersion curve of these surface plasmon waves is relatively flat at high frequencies and can be used to slow down light. In the low frequency (microwave) regime, however, the metal is treated as a perfect electric conductor (PEC), which means electromagnetic waves cannot penetrate into metal and hence metal-dielectric interface cannot support surface waves. So, instead of cut through slits or metal-dielectric interface, an array of holes drilled in metal surface were used to achieve slow electromagnetic waves[42, 43]. The schematic and numerical comparison between the metal dielectric structure and metallic hole structure is illustrated in Fig. 2.5[42].

These detailed studies about the behavior of the EM waves within these periodic metal dielectric interfaces led the way for two very intriguing structural schemes achieve high index of refraction in 2009. One was broad bandwidth 3D structure by J. Shin, et al.[44] while another was a resonance based structure by H. Shi, et al.[45]. J. Shin's structure consisted of metal cubes that were arranged in a cubic array fashion, all the six surfaces of these cubes consisted of air slits and were inter-connected by three orthogonal wires, as shown in Fig. 2.6(a). The structure was based on the observation that the induced charges due to normal electric field determines effective relative permittivity, ε_r while the induced surface current due parallel magnetic field contributes to the effective relative permeability, μ_r[44]. For large cube limit (i.e. $b \approx a$), permittivity and permeability can be estimated using following equations:

$$\varepsilon_r \approx a/(a-b), \qquad (2.6)$$

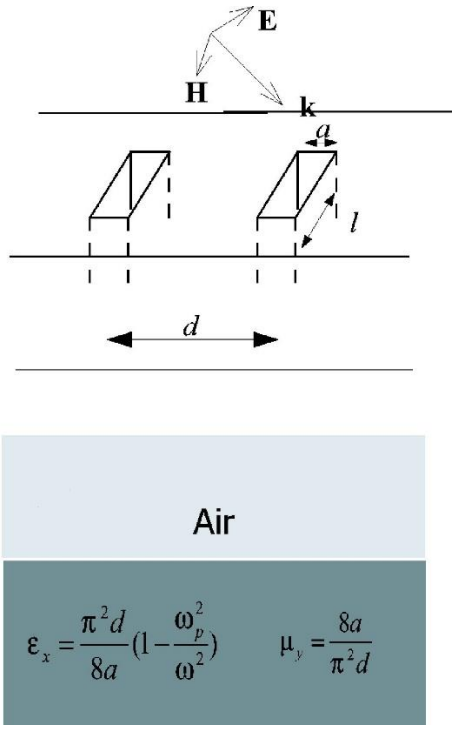

Fig. 2.5. Equivalent waveguide structure for periodic holes.

Metal surface with periodic holes drilled (above) and equivalent waveguide structure (below). [Reprinted with permission from "Z. Ruan and M. Qiu, Slow electromagnetic wave guided in subwavelength region along one-dimensional periodically structured metal surface. Appl. Phys. Lett. 2007, 90(20): p. 201906", with the permission of AIP Publishing]

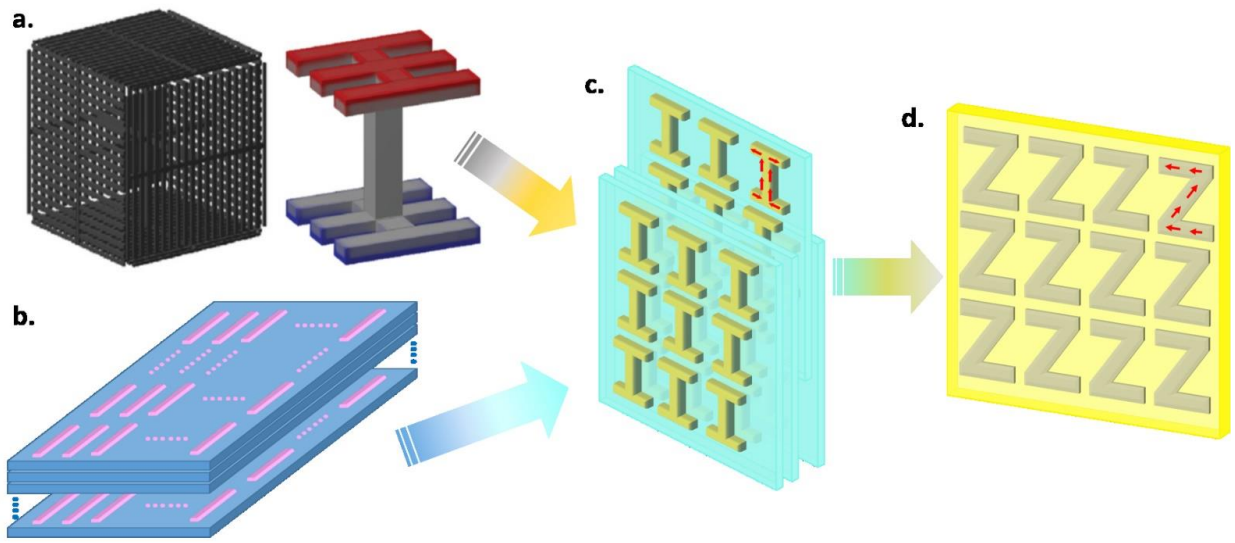

Fig. 2.6. Metamaterial design evolution.

(a) Unit cell of metal cubes that were arranged in a cubic array fashion, all the six surfaces of these cubes consisted of air slits and were inter-connected by three orthogonal wires along with the simplified structure (left) with two plates with air slits and a connecting wire along z-direction. *[Reprinted with permission from "J. Shin, J.T. Shen, and S. Fan, Three-dimensional metamaterials with an ultrahigh effective refractive index over a broad bandwidth. Phys. Rev. Lett. 2009, 102(9): 093903". Copyright (2009) by the American Physical Society].* (b) Layered view of bulk materials formed with unit cell of single cut wire on dielectric substrate. (c) 'I'- shaped metallic patch structure, (d) terahertz metamaterial with Z-shaped meta-atoms.

$$\mu_r = 1 - b^2/a^2 \approx \frac{2(a-b)}{a}, \qquad (2.7)$$

where 'b' is the side of the cube and 'a' represents the periodicity[44]. The simulated structure was able to enhance the refractive index over a broad bandwidth, by maintaining permeability near unity via reducing the area subtended by the current loops owing to the air slits in the surface and thereby suppressing the diamagnetic response. Meanwhile, the permittivity of the structure is enhanced by upholding a strong capacitive response within the cubic array. The other salient scheme, which was proposed by H. Shi, was based on electric resonance in the surface structures to enhance the effective refractive index[45]. H. Shi's configuration, as shown in Fig. 2.6(b) is a planar structure of periodic arrangement of metallic wires on a dielectric substrate of subwavelength thickness, which was then layered to achieve a bulk metamaterial. The value of maximum effective refractive index of the metamaterial is characterized using Bloch wave method and was defined using the following equation:

$$n_{max} = \beta_{max}/k_0 = \pi c/(\omega_0 d), \qquad (2.8)$$

where ω_0 is the resonance angular frequency, β_{max} is the propagation constant at the resonance, k_0 is the wave number at resonance frequency and *d* is the periodicity of the structure[45]. The length of the metallic subwavelength wires controlled the resonance frequency while the propagation constant corresponding to higher refractive index around the resonance is governed by the number of layers along the direction of propagation of the electromagnetic wave. This resonance based scheme offered a contrast to the previous prevalent methods which achieved high refractive index by the confinement of electromagnetic mode in the highly subwavelength region, i.e. the propagation TEM mode in the slits and evanescent mode in the holes below the cutoff[45]. This metallic wire array metamaterial design was soon after, experimentally verified and analyzed by X. Wei, et al. in 2010, to achieve high refractive index value at visible frequencies with a metamaterial fabricated using quartz as dielectric substrate and silver to form cut wire structure[46].

In 2011, M. Choi, et al., exquisitely combines both J. Shin[44] and H. Shi's[45] schemes to demonstrate high refractive index value at terahertz frequencies. The resonating subwavelength cut wire structure in H. Shi's scheme was replaced with an 'I'-shaped metallic patch[47], an abridged 2D version of J. Shin's silted cube structure. The resultant metamaterial structure, as shown in Fig. 2.6(c) is capable of producing high effective permittivity due to a strong capacitive behavior while maintaining a low diamagnetic response due to the smaller current-loop area. M.Choi's metamaterial was fabricated on flexible, thin film polyimide substrate, the metallic structure was created using gold (on chromium), a periodic array of thus created unit cells is then layered on top of each other similar to H. Shi's scheme, to investigate the bulk properties of the metamaterial. The band structure and the dispersion relation of the fabricated metamaterial was investigated to understand the effect of number of layers on the electromagnetic characteristics of the bulk media. The maximized transmission of the slab is defined by the equation,

$$f_p = (pc)/(2nNd), \qquad (2.9)$$

where f_p is the transmission peak frequency, p is a non-negative integer, N is the number of layers, c is the speed of light and d is the thickness of each layer[47]. M. Choi experimentally achieved a refractive index as high as 38.64 at 0.315 THz and claimed that higher values of refractive index can be achieved by reducing the distance between the individual 'I'-shaped metallic patches or the spacing between each layer until the gap width reaches the Thomas–Fermi length scale[48] or the quantum tunneling scale of electrons.

The exact 3D structure of metallic cubes arranged in a cubic array fashion proposed by J. Shin, et al.[44], was experimentally demonstrated in microwave regime by T. Campbell, et al. in 2013[1]. T. Campbell fabricated two samples, one with array of solid copper cubes and another with an array of structured copper cubes. Both the samples were characterized using strip line method for material characterization pioneered by W. Barry in 1986[49]. The comparison of the experimentally obtained material parameters of the solid cubes with that of the structured cubes

revealed that the real part of permittivity of the structured cube sample was approximately half that of the solid cube sample but the refractive index was still nearly doubled since the structured cubes facilitated reduced diamagnetic response resulting in almost six-fold increase in the effective permeability value[1].

S. Tan, et al. furthered M Choi's 'I'-shaped metallic patch structure[47] with a Z-shaped meta-atom in 2015[50], as shown in Fig. 2.6(d). The Z-shaped meta-atom was capable of attaining high refractive index at lower frequency by virtue of existence of a parallel, unidirectional surface current in the two arms of the structure which leads to larger effective induction as compared to that in I-structure thus lowers the resonance frequency without having to reduce the size of the over-all structure. The Z-structure metamaterial was fabricated using conventional lithography using aluminum and thin film polyimide substrate. Time–domain terahertz spectroscopy characterization revealed 21.6% average shift in the resonance frequency[50]. This simple design modification offered great ease in the fabrication of high refractive index metamaterials operating at lower frequencies. In depth discussion of this work is provided in chapter 3. In 2016, T. Chang reported a broadband refractive index scheme based on mesoscopic space-filling curves. He claimed gigantic dielectric constant enhancement due displacement between the layers resulting in very high displacement enhancement factor[51].

2.6 High refractive index via deep subwavelength coupling

Although above approaches were able to enhance refractive index to unnatural values, the highest values of refractive indices achievable with these schemes are demarcated mainly due to two reasons. First, the limit posed by the number of layers that can be productively used at a particular frequency, dictated by equation no. (2.9). Second, the practical limit to which the periodicity of the meta-atoms can be decreased, before losing the capacitance effect all together.

In 2017, we proposed a terahertz metamaterial design capable of achieving even higher values of refractive index owing to a very high effective permittivity realized by employing deep subwavelength coupling between the arrays of identical structures situated on both sides of an ultra-thin dielectric film, as shown in Fig. 2.7[13].

Owing to the subwavelength thickness of the substrate film, the metal structures situated on both of its sides got coupled generating tremendous capacitive response in addition to the capacitance due to the nearest neighbor coupling between structures on the same side. Meanwhile the permeability of the metamaterial remained near unity due to small current loop area subtended by the checkboard metal structure. An array of isotropic checkboard structure was fabricated by thermal deposition of aluminum on both sides of polyimide substrate film of thickness 22 and 1 μm, respectively. Using terahertz-time domain spectroscopy, both the samples were characterized and the calculated effective refractive index for the 1 μm thick sample was found to be increased to 41.8 as compared to that of 7.78 refractive index for the 22 μm thick sample and can be further increased to 77.02 for a 100 nm thick sample. The enhancement of the refractive index can be further boosted by increasing deep subwavelength coupling between meta-atoms on the opposite side of the spacer layer either by decreasing the substrate layer thickness or selecting a substrate of higher refractive index or both. The effective refractive index of the metamaterial governed dominantly by the inter-layer deep subwavelength coupling, demonstrated a universal power law behavior (described by equation no. (2.10)) with respect to the substrate thickness, and a linear behavior (described by equation no. (2.11)) with respect to the substrate refractive index:

$$N_{effective} = \alpha t^{\beta}, \qquad (2.10)$$

$$N_{effective} = aN_{substrate} + b, \qquad (2.11)$$

where α, β, a and b are the constants that depend on the metamaterial structure, t is the substrate film thickness and $N_{substrate}$ is the substrate refractive index. Although it was predicted by many previous schemes[40, 45, 47] that

decreasing the thickness of individual designer layers of bulk metamaterial would enhance the refractive index values, it was the first time that reducing the substrate thickness to subwavelength levels was utilized to facilitate coupling effect between the resonating structures fabricated on both the sides of the substrate layer. This inter-layer subwavelength coupling led to a very high effective permittivity in the sample and thus an ultra-high value of the effective refractive index of the metamaterial. The complete description of this scheme is presented in chapter.3.

2.7 Conclusion

In conclusion, the science of designing high refractive index medium has come a long way since manipulating the intrinsic state of matter to the design of metamaterials with perpetually imaginative structures. It may not even be far-fetched to assume that the high refractive index media designed with static values of refractive indices have become quite saturated. In recent years the focus has shifted more towards devising media capable of dynamic enhancement of the refractive index[54, 55] by means of electrical stimuli. These incredible scientific endeavors leading to the realization of thin film, broadband, dynamic control, and ultra-high refractive index media are sure to play a crucial role in shaping the face of modern devices.

ACKNOWLEDGEMENT: This chapter has been previously published as , " L. Singh and W. Zhang, Advancements in high refractive index media: from quantum coherence in atomic systems to deep sub-wavelength coupling in metamaterials [Invited], Chin. Opt. Lett. Vol. 18, pp. 062401, 2020".

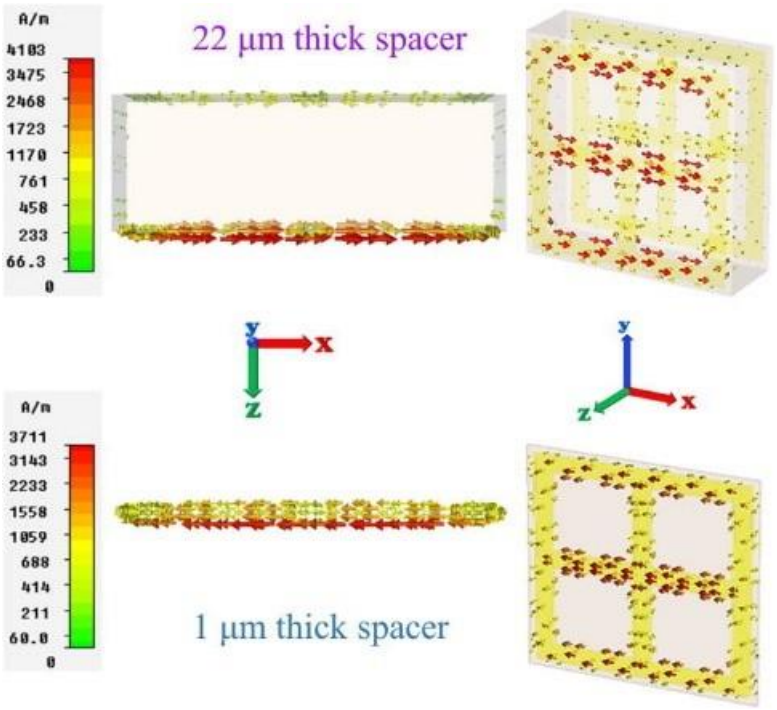

Fig. 2.7. Ultra-thin terahertz metamaterial

Ultra-thin terahertz metamaterial with double sided metal structure. Depicting deep subwavelength coupling absence (above) and presence (below) between the metal structures situated on both sides of an ultra-thin dielectric substrate. [Reprinted with permission from "L. Singh, R. Singh, and W. Zhang, Ultra-high terahertz index in deep subwavelength coupled bi-layer free-standing flexible metamaterials. J. Appl. Phys. 2017, 121(23): 233103", with the permission of AIP Publishing]

CHAPTER III

ULTRA-HIGH TERAHERTZ INDEX IN DEEP SUBWAVELENGTH COUPLED BI-LAYER FREE-STANDING FLEXIBLE METAMATERIALS

This chapter presents detail description of a free standing, thin film metal dielectric checkboard structure which is capable of enhancing the refractive index to unnaturally high values by exploiting the deep subwavelength coupling.

Using this metamaterial structure a record high refractive index of 77.02+43.22*i* is obtained at terahertz frequencies. The chapter also describes a power law that governs the enhancement of the effective refractive index of the structure via deep subwavelength coupling in a bilayer design. This presents a far simpler and effective approach for refractive index enhancement. The approach relies on deep subwavelength coupling to obtain extremely high refractive index values that can lead to many practical applications in the field of imaging, lithography, design of delay lines and interferometers.

3.1 Introduction

In a sense, every material is a composite, even if the individual ingredients consist of atoms and molecules.[56] These natural atoms when replaced with artificially designed unit cell structures (meta-atoms), result in an engineered material that is now well known as metamaterials. Metamaterial properties are derived from their meta-atoms rather than their composition. These sub-wavelength meta-atoms can be designed with unique shapes and sizes, and wit-fully arranged and oriented to achieve unconventional values of permeability [57] and permittivity [58], the characteristic electromagnetic properties of any material medium. By tailoring the electric and magnetic response of the material towards incident electromagnetic waves, the effective refractive index can be varied from negative[18, 19, 59-62] to zero,[63-66] or even to higher positive values.[64, 67-72] Metamaterials have created a completely new dimension to engineered materials. This has offered an opportunity to build new devices with exotic functionalities.[73] Metamaterials are proven to be especially valuable in the terahertz regime, where most naturally existing materials exhibit weak electromagnetic wave response.[74-76]

Recently, high-index metamaterials have drawn much attention.[69] Higher values of positive refractive indices are especially desired in the field of imaging and lithography, where the resolution scales inversely with the refractive index.[77] Increasing the refractive index over a large frequency range results in the broadband slow light, which can be used to enhance the storage capacity of the delay lines[78]. High indexed metamaterials may also enhance the spectral sensitivity of certain types of interferometers[79] and can benefit many other practical application areas. Most of the previous high indexed metamaterials offer a specific value of fixed high refractive index or short range of high index values.[72] Enhancing refractive index values for any of these previous structures usually involves dealing with complicated parameter trade-off equations or structural element changes[67, 80]. Another method used so far, to increase refractive index values, is to stack multiple layers of same structure, which is not only a complicated approach due to the alignment issues but also results in thicker metamaterials, and hence limits the maximum values of refractive index that can be achieved. Enhancing the effective value of refractive indices over a broad range, for a thin film, free

Reference article	Frequency	Highest value of ref. index
Ref. 13.	0.384 THz	61.83
Ref. 14.	0.333 THz,	14.36
Ref. 16.	0.315 THz	54.87
This work	2.11 THz	77.02

Table 3.1. Performance comparison.

The effective refractive index value of the current state of the art are compared with that of the proposed structure.

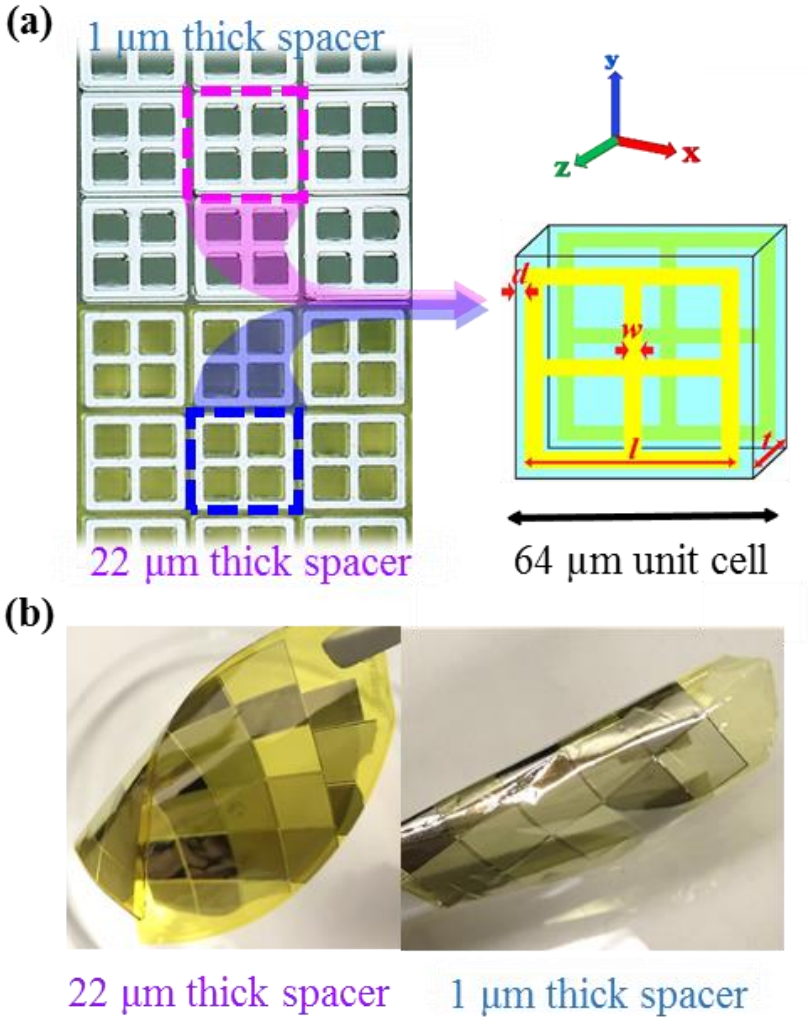

Fig. 3.1. Microscopic images and Unit cell design.

(a) Microscopic image of the fabricated samples(left). Dimensions of the checkboard structure are l = 60 μm, w = 5 μm, d = 4 μm and t = 22 μm and 1 μm, respectively. The aluminum structures of thickness, t_m = 0.2 μm are fabricated on both the sides of the polyimide substrate (spacer layer), 3D view shown on the right side. (b) Photograph showing flexibility of the fabricated free standing samples, with 22 μm and 1 μm substrate thickness, respectively

standing metamaterial, still remains a challenge. An effective refractive index values comparison of the proposed structure with that of the current state of the art is presented in Table 3.1.

In this chapter, we propose and demonstrate a high index metamaterial that consists of an aluminum closed resonator array on two sides (front and back) of a mechanically stable, thin-film, free-standing polyimide substrate. Figure 3.1a shows the microscopic image of the checkboard structure. The structure is symmetrical in both the *x*- and *y*-directions, making the metamaterial insensitive to the polarization of incoming light at normal incidence. The inset of Figure 3.1a shows the design and dimensions of the unit cell structure of the metamaterial. The length of the metallic unit cell structure is set at 60 μm and the width of the metal bars, *w* is 5 μm. The entire sample consists of 156 × 156 unit cells with a periodicity of 64 μm.

3.2 Experimental and numerical design

To investigate the effect of deep subwavelength coupling in the proposed metamaterial structure, two samples with polyimide substrate thickness of 22 μm and 1 μm were fabricated and characterized using terahertz time-domain spectroscopy (THz-TDS) system. Two layers of polyimide (PI 2525) of 11 μm each, were spin coated on a silicon substrate by conventional lithography techniques, each followed by soft bake for 2 minutes at 120º C. The final 22 μm thick polyimide spacer layer was cured at 150º C, with an increase of 5º C per minute up to 250º C, which was maintained to be constant for 30 minutes and then decreased to 100º C for 20 minutes. A single layer of polyimide (PI 2610) was spin coated at 500 and 5000 rpm for 5 and 30 seconds, respectively, followed by a soft bake at 90º C for 90 seconds. The 1 μm thick polyimide spacer layer was then heat cured with an increase of 4º C per minute from room temperature, up to 350º C, which was maintained for 30 minutes. Both the polyimide layers were finally allowed to be cooled down to room temperature.

An aluminum layer of 0.2 μm was uniformly deposited on the cured polyimide layers by thermal evaporation, which was patterned using a positive photoresist, PR1-4000A. The polyimide layer with metal structure was then peeled off from the silicon wafer to form a free standing sample. Another 0.2 μm thick aluminum layer was deposited and structured on blank side of the polyimide substrate. Finally, the fabricated thin-film, free-standing metamaterial samples are shown in Figure 3.1b.

A photoconductive switch based THz-TDS system that consists of four parabolic mirrors, arranged in an 8*f* confocal geometry was used to characterize the transmission properties of the metasurface[81-83]. The transmission is recorded with the terahertz beam illuminating the sample at normal incidence, along the *z*-axis. The electric field vector is in the *x*-direction and the magnetic field vector is in the *y*-direction (*x*, *y* and *z* in Figure 3.1a). The *8f* confocal system illuminates the metasurface sample with a focused terahertz beam of 3.5 mm waist diameter. The transmission amplitude is calculated as

$$t(\omega) = \left| {Es(\omega)}/{Er(\omega)} \right|, \qquad (3.1)$$

where $Es(\omega)$ and $Er(\omega)$ are the Fourier transform of the transmitted signal through the sample and the reference, respectively. The free space terahertz pulse in a dry nitrogen purged environment is used at normal room temperature as a reference. The experiment is conducted with 17 ps time-domain terahertz pulse scan, so as to provide a spectral resolution of 59 GHz to the measurements.

The measured transmission amplitude through the metamaterial sample *(orange)* and air as reference *(pink)* are shown in Figure 3.2 a, for both 22 μm and 1 μm samples, respectively.

The transmission through the 22 μm sample is quite significantly attenuated beyond 1.12 THz and remains almost zero in the frequency band of 1.2-2.1 THz. An extensive set of simulations have been performed using commercially available Finite Integration Method solver in CST microwave studio.

During simulations, the sample shows an angle independent behavior, hence the angle of incidence was kept normal to the sample surface. The background material properties were set to type normal, i.e. air with $\varepsilon = 1.0$ and $\mu = 1.0$. Closed electric and magnetic boundary conditions were set along the *x*-axis and *y*-axis, respectively, while an open boundary condition was employed along the *z*-axis. The observation ports were set at a distance of 5 μm along the *z*-axis from the sample surface, in order to obtain far field response for the *x*-polarized incident wave. Polyimide (lossy) with permittivity (Re[Ɛ] = 2.96)[67] and aluminum with conductivity 2.2×10^7 S/m[84] available with the CST material library are used in the simulation. Experimentally measured and the simulated, transmission amplitudes are found to be in excellent agreement with each other, as shown in Figure 3.2b, for both 22 μm and 1 μm samples, respectively. The slight deviations arise from the non-conformities during the fabrication process and variations in the material parameters used for the simulations.

3.3 Results and discussion

The simulated reflection parameter, S11 (green) and the simulated transmission parameter, S21 (blue) for the 22 μm and 1 μm samples are shown in Figure 3.3a. For the 22 μm sample, the transmission is drastically suppressed after 1.12 THz, and the reflection reaches unity while in the case of the 1 μm sample the reflection gradually approaches to unity near 1.5 THz. This clearly shows that most of the incident wave energy is reflected back rather than being scattered at non-zero angles with respect to the surface normal. The checkboard structure can be seen as an infinite periodic grating, in reference to diffraction theory. Since

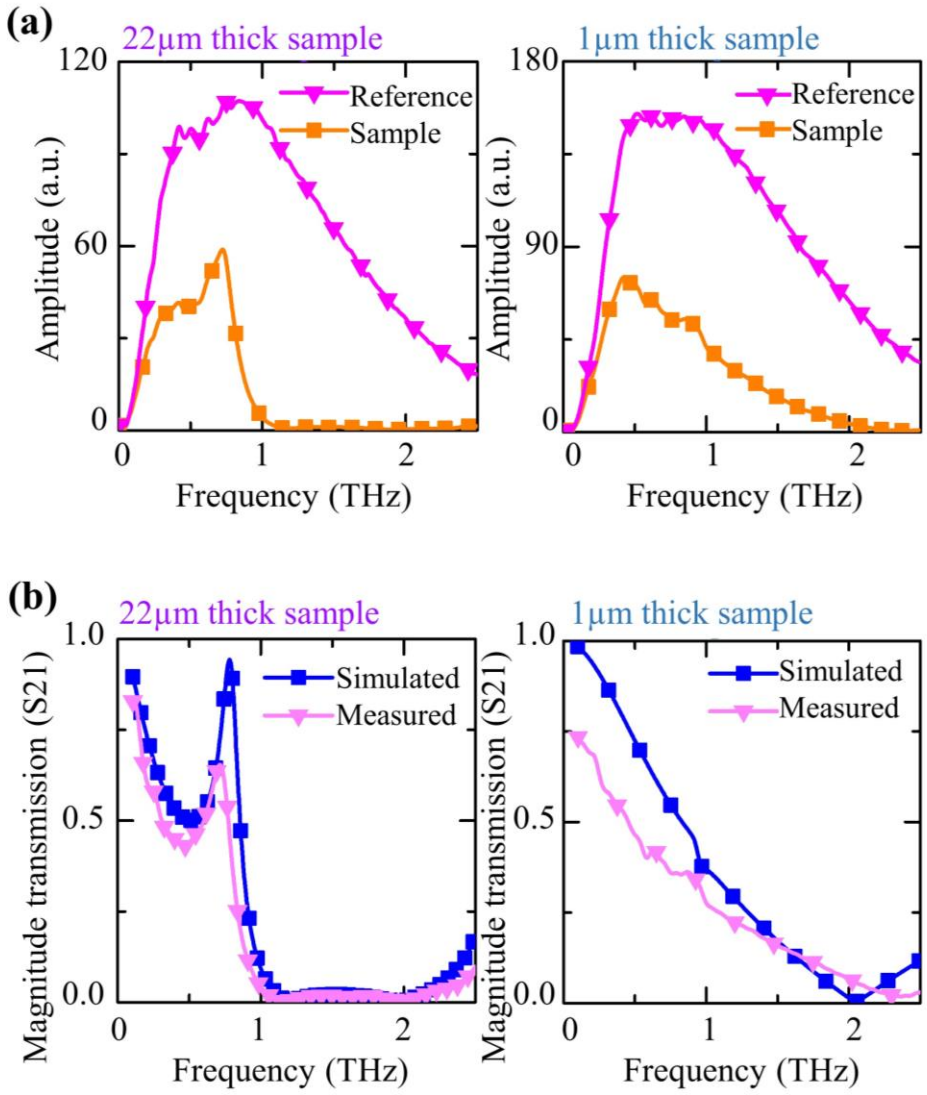

Fig. 3.2. Simulated and measured transmission map.

(a) Measured transmission amplitude for the 22 μm and 1 μm thick samples is compared with that of the reference, air and (b) comparison between the simulated and the measured transmission magnitude (normalized w.r.t. air as reference) for the samples is shown for the 22 μm and 1 μm thick samples, respectively

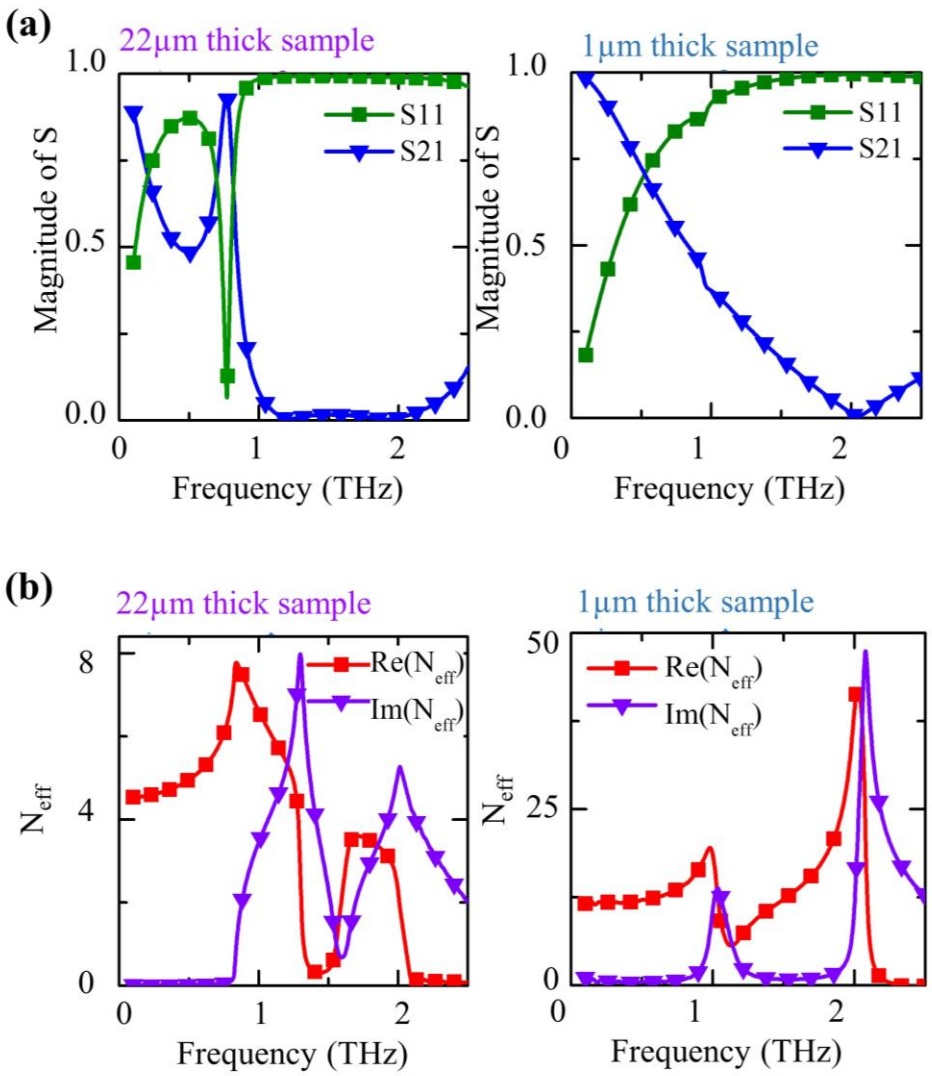

Fig. 3.3. Simulated S-parameter and calculated refractive index.

(a) Simulated reflection, S11 (green) and simulated transmission, S21 (blue). (b) Calculated complex refractive index of the samples with peak values 7.78+0.96*i* at 0.839THz and 41.8+22.07*i* at 2.026 THz for the 22 μm and 1 μm samples, respectively

the unit cell of periodicity 64 μm is much smaller as compared to the wavelength of interest (~299 μm), the first order diffraction for the structure does not exist at normal incidence.

The standard parameter retrieval equation was adopted for the refractive index extraction using the simulated transmission (S21) and reflection (S11) values[85]. In order to choose the correct branch of the real part of the refractive index[86], a customized matlab code[87] is used to extract the complex refractive index of the metamaterial solving the following equations[86].

$$S_{11} = \frac{R_{01}\left(1-e^{i2nk_0d_{eff}}\right)}{1-R_{01}^2e^{i2nk_0d_{eff}}}, \qquad (3.2a)$$

$$S_{21} = \frac{(1-R_{01}^2)e^{ink_0d_{eff}}}{1-R_{01}^2e^{i2nk_0d_{eff}}}, \qquad (3.2b)$$

where

$$R_{01} = \frac{Z-1}{Z+1},$$

$$z = \pm\sqrt{\frac{(1+S_{11})^2 - {S_{21}}^2}{(1-S_{11})^2 - {S_{21}}^2}},$$

d_{eff} is the effective thickness of the homogeneous slab. In order to consistently estimate the effective refractive index, the sum of substrate thickness, t and twice of metal layer thickness, t_m (for two layers) is used as d_{eff}, effective thickness, for equation 2a and 2b. Since the experimental and the simulated transmission amplitudes are in excellent agreement with each other, the simulated transmission (S21) and reflection (S11) values can be reliably used for the estimation of the effective parameters.

The calculated effective refractive index of the medium, with the highest peak value of 7.78+0.96*i* at 0.839 THz is obtained for the 22 μm sample while it is 41.8+22.07*i* at 2.026 THz for the 1 μm sample as shown in Figure 3.3b.

When there is a decrease of 95.5% in the thickness of the sample, the real part of the refractive index shows an increase of 437.3%. It is interesting to note that although the imaginary part of the refractive index, which is indicative of the absorption losses in the sample, shows an increase of 2203.76%, with the same decrease in sample thickness, the value of the imaginary part is smaller as compared to their real counterparts, hence it does not significantly hamper the performance of the samples. The smaller value of the imaginary part of the refractive index as compared with their real counterparts, for both the 22 μm and 1 μm samples, at the respective frequencies of interest is indicative of lower absorption losses in the metamaterial.

It is worth noting that the effective homogeneity condition, which requires that the thickness along the propagation direction is smaller than the operating wavelength, remains valid throughout the frequency band of operation [67]. The effective permittivity and permeability of metamaterial samples are numerically extracted using the following equations [86]

$$\varepsilon_{eff} = \frac{N_{eff}}{Z_{eff}}, \qquad (3.3a)$$

and

$$\mu_{eff} = N_{eff}.Z_{eff}, \qquad (3.3b)$$

where N_{eff} and Z_{eff} are the effective refractive index and normalized impedance retrieved from the S-parameters, respectively[67].

The real part of the effective refractive index *(red)* for 22μm samples shown in Figure 3.3b, shows two peaks. The first peak value of the real part of the effective refractive index is due to permeability peak of 9.75+7.69*i* at 0.827

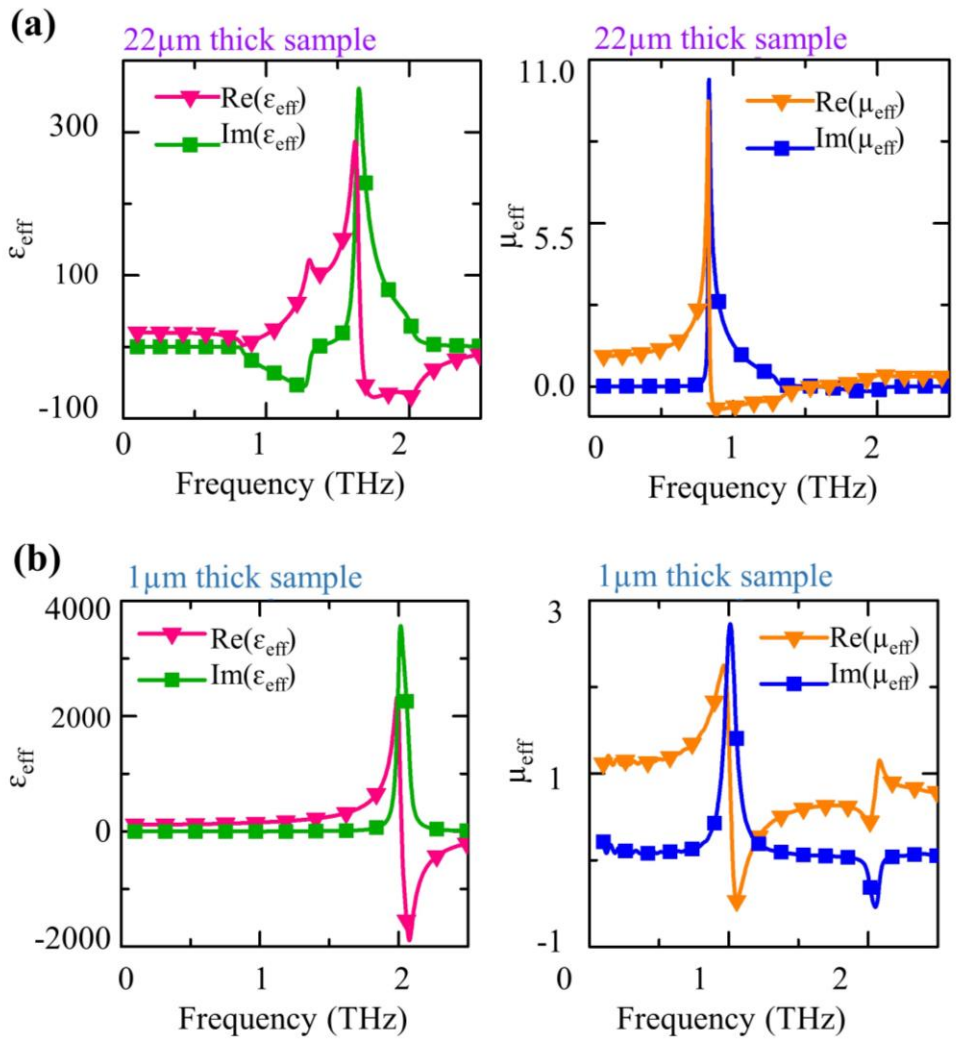

Fig. 3.4. Calculated permeability and permittivity.

(a) and (b) Numerically obtained values of effective permeability and permittivity from the S-parameter retrieval method for the 22 μm and 1 μm samples, respectively.

THz and the second local maxima of the real part of the effective refractive index, is contributed by the effective permittivity peak of 287.6+198.8*i*, at 1.623 THz, as shown in Figure 3.4a.

This clearly shows that the peak effective refractive index of the 22 μm sample is contributed by the high magnetic activity [88-90][of the structure at resonance frequency. Similarly, for the 1 μm sample, the first local maxima of the real part of the effective refractive index (red), as shown in Figure 3.3b, is due to the permeability peak of 2.51+1.484*i* at 0.967 THz, as shown in Figure 3.4b, while the second maxima, which also happens to be the peak value of the real part of the effective refractive index, is contributed mainly by the permittivity peak of 2336+1993*i* at 1.99 THz and not by the permeability, which remains unity at the frequency of interest, as shown in Figure 3.4b. For both 22 μm and 1 μm samples, we observe two peaks in the real part of the effective refractive index values. The first peak appears due to high permeability of the sample and the second peak is contributed mainly by the high permittivity of the sample. In the case of the 22 μm sample, the highest value of the real part of the effective refractive index (first peak) appears due to high permeability of the sample, while in the case of the 1 μm sample, the highest values of the real part of the effective refractive index (second peak) appears due to the high permittivity of the sample. This exceptionally high value of the effective permittivity, in the case of the 1 μm sample is in fact, the result of the deep subwavelength coupling between the meta-atoms on the opposite sides of the structure, which is enhanced due to the decrease in the substrate thickness.

Moreover, it is noteworthy that in Figure 3.4a and b, the imaginary parts of both permittivity and permeability attain negative values for different frequencies. This is not in contradiction with any physical law[91-95]. The dissipated energy, *W* is given by the following equation,[94]

$$W = \frac{1}{4\pi}\int d\omega\omega[\,\varepsilon''|E(\omega)|^{\,2} + \mu''|H(\omega)|^{\,2}], \qquad (3.4)$$

where $\varepsilon'' \; and \; \mu''$ are the imaginary parts of the effective permittivity and permeability, respectively. The condition W>0, does not require that $\varepsilon'' \; and \; \mu''$ must be simultaneously positive.[96] We further investigate the distribution of electromagnetic field inside the structure, the electric and magnetic energy density at 0.839 THz for the 22 μm sample and at 2.026 THz for the 1 μm sample is shown in Figure 3.5. For the *x*-polarized incident electromagnetic wave, the electric energy is mainly concentrated on the edges of the structure along the *y*-axis, which shows a strong coupling between the adjacent structures on the same side of the substrate. The magnetic energy density inside the structure is very weak, other than central metal bar along the *x*-axis. Owing to the thin metal layer of 200 nm and 5 μm width, the area subtended by the induced current loop is very small, which does not support a high magnetic moment and hence, leading to an extremely low diamagnetic effect at the frequency band of interest[44, 67, 69]. The permittivity of metamaterials, which is mainly due to the strong capacitive coupling between the adjacent unit cell, can be increased multiple-fold, by decreasing the substrate thickness and hence allowing deep subwavelength coupling between the meta-atoms on the opposite sides of the structure. In order to explore the enhancement of the effective refractive index by means of deep sub-wavelength coupling, an extensive study of six samples with varying dielectric spacer thickness has been carried out. All the geometric parameters except for the dielectric thickness (*t*) are kept constant for all the samples. The effect of the change in thickness, *t* of the polyimide spacer layer on the effective refractive index of the metamaterial is shown in Figure 3.6a.

Refractive index as high as 77.02 at 2.11 THz is achieved by reducing the polyimide spacer thickness to 100 nm. This value of refractive index is five-fold higher than that of the initial structure, with 22 μm thick spacer layer. The numerical simulations demonstrate, that as the spacer thickness decreases, the deep subwavelength coupling between the meta-atoms on the opposite side of the spacer layer is enhanced which leads to an increase in the effective refractive index of the sample.

The numerically calculated peak value of the effective refractive indices as a function of the dielectric spacer thickness

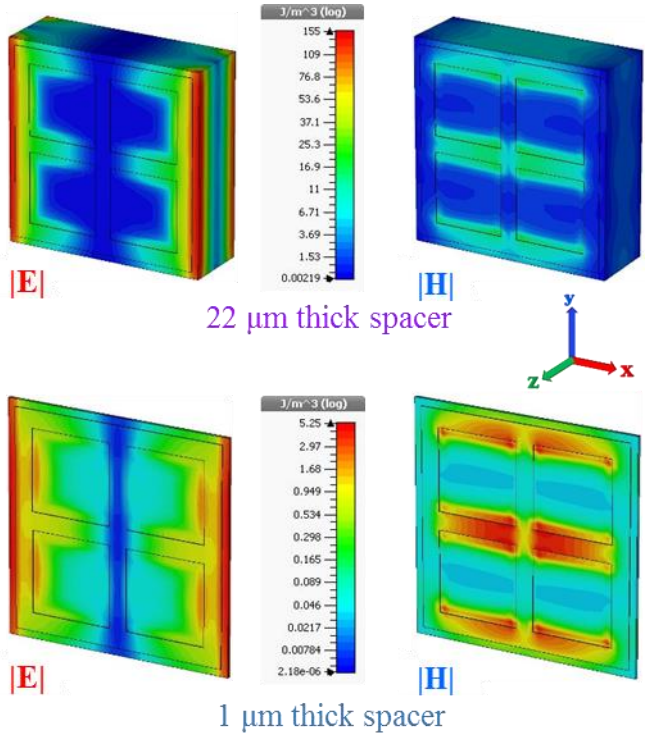

Fig. 3.5. Energy density.

Simulated distribution of the electric and magnetic energy density at 0.839 THz and 2.026 THz for the 22 µm and 1 µm samples, respectively.

is shown in Figure 3.6 b. To our surprise, the peak value of the effective refractive indices (N_{peak}) demonstrates a universal power law behavior, with respect to the dielectric spacer thickness (t) described by

$$N_{peak} = 37.076t^{-0.424}, \qquad (3.5)$$

at the spacer thickness less than 5 um. This is further verified by plotting the natural log of both spacer thickness and the peak value of the effective refractive indices shown in Figure 3.6c. The data could be easily fit to a straight line, which is a signature of the power law and is indicative of the scale invariance and the universality of the function,

$$ln(N_{peak}) = -0.4243ln(t) + 3.613. \qquad (3.6)$$

The above equation clearly establishes, that exploiting the deep subwavelength coupling between the meta-atoms on the opposite side of the substrate by tailoring the dielectric spacer thickness, is one of the most straightforward and efficient ways to enhance the peak refractive index over a much wider range of values. The significance of this finding lies in the ease and capability to use a rather simple structure, to achieve the precise values of the positive high refractive index, as required in various fields of application.

The effect of deep sub-wavelength coupling can be clearly visualized by the surface current distribution in the structure. Figure 3.7 shows the surface current distribution for the 22 μm and 1 μm thick samples.

The metal structure on the back side of the 22 μm thick substrate (that acts as the spacer) is weakly coupled with that of the front side metal closed ring, as seen by the incident wave, leading to lower permittivity and hence lower effective refractive index peak as compared to that of thinner substrates. For the 1 μm spacer thickness, there exists a significantly strong subwavelength coupling between the opposites sides of the substrate, as illustrated in Figure 3.7 by the stronger surface current distribution.

Another set of simulations was carried out, in order to study the effect of alignment between the two sides of the

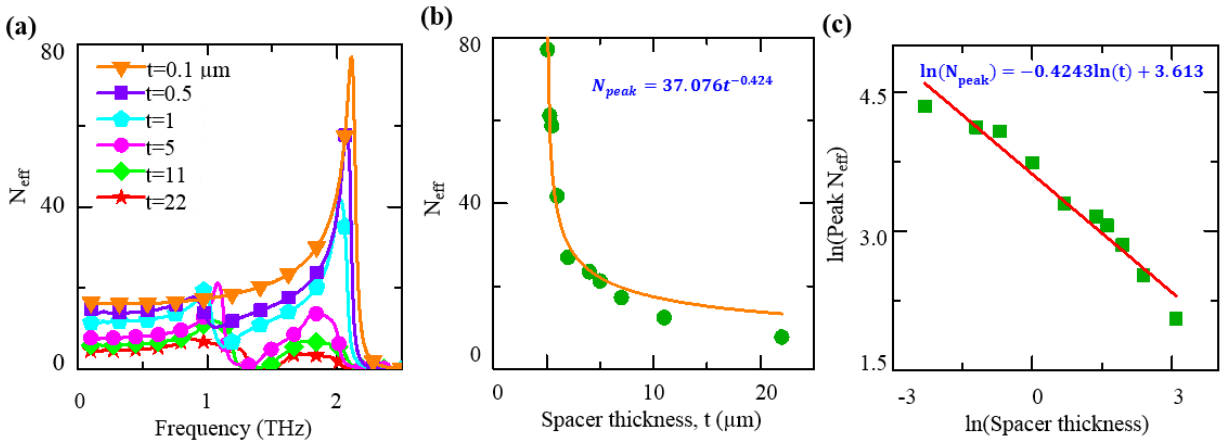

Fig. 3.6. Effective refractive index versus substrate thickness.

(a) Calculated effective refractive index for the various spacer thicknesses, (b) change in the peak value of the effective refractive index w.r.t. the spacer thickness and (c) natural log of the peak refractive index versus natural log of the spacer thickness

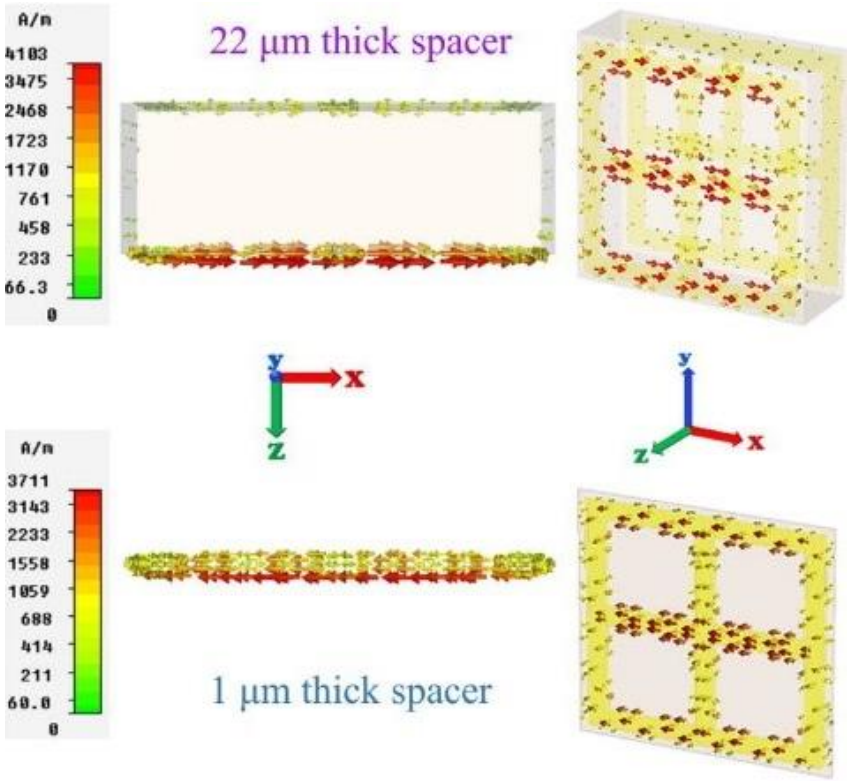

Fig. 3.7. Surface current distribution.

Top and perspective view of the surface current distribution for normal incident wave along the z-direction inside the structure with (a) 22 μm thick substrate and (b) 1 μm thick substrate.

structure, on the peak refractive index value. It was observed that the peak refractive index value which depends on the strength of the subwavelength coupling between meta-atoms at the two sides of the sample, as visualized by the surface current distribution in Figure 3.7, in turn depends on the amount of the area of the metallic elements of the two sides being superposed on each other. This finding opens up another opportunity for further enhancement of the refractive index, by changing the structure, such that there is an increase in the superposition area between the two sides.

We further investigated the effect of the change in the refractive index of the spacer layer to enhance the deep subwavelength coupling between the two metal sides of the structure. In order to systematically examine the effect of the change in the substrate refractive index on the effective refractive index (N_{eff}) of the overall structure, two samples with 22 μm and 1 μm thicknesses were simulated and studied with varying substrate refractive index, keeping all other dimensions of the structure constant. The effective refractive index of the structures increases with increasing the substrate refractive index, as shown in Figure 3.8a and 3.8b. The higher refractive index substrates further facilitated the coupling between the meta-atoms on opposite sides of the samples. The plot of the peak value of the effective refractive index (N_{peak}) as a function of the spacer layer refractive index (N_{spacer}) for 22 μm and 1 μm samples, shown in Figure 3.8 a and 3.8 b, perfectly follows linear behavior, and is expressed as Equations 3.7 and 3.8, respectively,

$$N_{peak} = 3.5052 N_{spacer} + 1.6309, \qquad (3.7)$$

$$N_{peak} = 6.5148 N_{spacer} + 29.951. \qquad (3.8)$$

This finding is significant, as it provides the capability to further tailor the effective refractive index of the metamaterial, independent of the thickness of the substrate. Moreover, the fact, that Equation 3.8 for the 1 μm sample, shows a steeper slope as compared to that of Equation 7 for the 22 μm sample, indicates that increasing the spacer metamaterial, independent of the thickness of the substrate. Moreover, the fact, that Equation 3.8 for the 1 μm

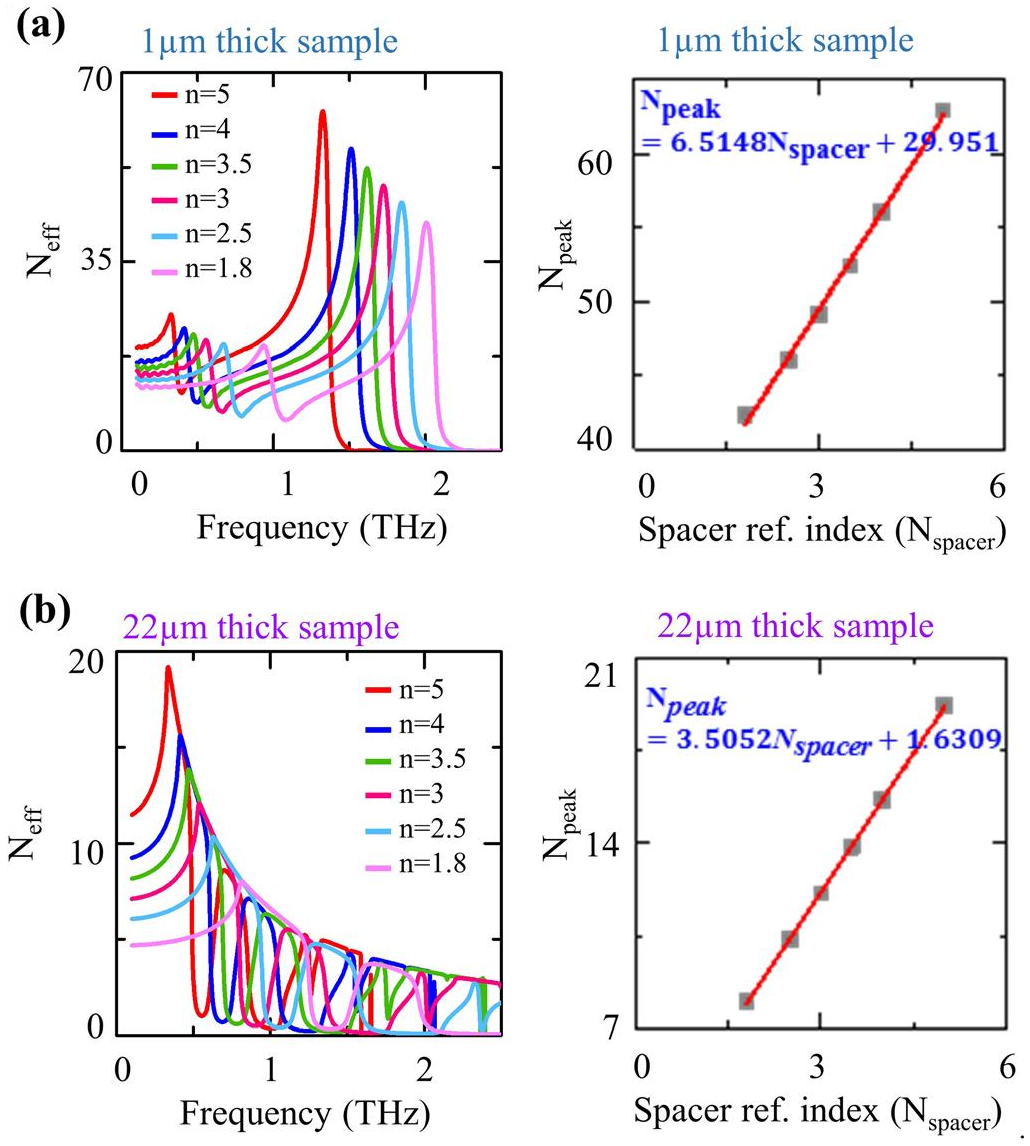

Fig. 3.8. Effective refractive index versus substrate refractive index.

Calculated effective refractive index for varying the spacer refractive index for (a) 1 um and (b) 22 um thick samples. Change in the peak value of the effective refractive index of the sample with respect to the spacer refractive index for (a) 1 um and (b) 22um thick samples.

sample, shows a steeper slope as compared to that of Equation 7 for the 22 μm sample, indicates that increasing the spacer refractive index is more effective when the sample thickness is low. Theoretical and numerical simulations reveal that by combining the effect of the both, decreased substrate thickness, to 0.1 μm and increased substrate refractive index, of 5 units, a peak refractive index of 83.42 at 1.93 THz, can be achieved

3.4 Conclusion

We have experimentally and numerically demonstrated the effect of enhancing the deep subwavelength coupling to achieve extremely high refractive index in terahertz metamaterials. More than five-fold enhancement in the peak value of the effective refractive index was realized by merely altering the dielectric spacer thickness. As a result, a peak refractive index of about 77.02 at 2.11 THz was experimentally characterized. Exploiting deep subwavelength coupling, by means of varying dielectric spacer thickness would benefit other metamaterials structures as well, to enhance the peak values of their refractive index. Such designs of high refractive index metamaterials may find applications in terahertz photonics where the naturally occurring materials have limited response

ACKNOWLEDGEMENT: This chapter has been previously published as, "L. Singh, R. Singh, and W. Zhang, Ultra-high terahertz index in deep subwavelength coupled bi-layer free-standing flexible metamaterials, Journal of Applied Physics, vol. 121, p. 233103, 2017".

CHAPTER VI

TERAHERTZ SENSING OF HIGHLY ABSORPTIVE WATER- METHANOL MIXTURES WITH MULTIPLE RESONANCES IN METAMATERIALS

Terahertz sensing of highly absorptive aqueous solutions remains challenging due to strong absorption of water in the terahertz regime. In this chapter, we experimentally demonstrate a cost-effective metamaterial-based sensor integrated with terahertz time-domain spectroscopy for highly absorptive water-methanol mixture sensing. This metamaterial has simple asymmetric wire structures that support multiple resonances including a fundamental Fano resonance and higher order dipolar resonance in the terahertz regime. Both the resonance modes have strong intensity in the transmission spectra which we exploit for detection of the highly absorptive water-methanol mixtures. The experimentally characterized sensitivities of the Fano and dipole resonances for the water-methanol mixtures are found to be 160 and 305 GHz/RIU, respectively. This method provides a robust route for metamaterial-assisted terahertz sensing of highly absorptive chemical and biochemical materials with multiple resonances and high accuracy.

4.1 Introduction

Metamaterials exhibit strong optical response towards the presence of an analyte due to strong localization and enhancement of the electromagnetic fields. Such a response enables material sensing with metamaterials in different spectral range, extending from microwaves to optics [103-110].

Recently, metamaterial-assisted sensing platform integrated with terahertz spectroscopy has attracted a lot of interests and is being increasingly implemented for chemical and biological sensing[109-125]. The key advantages of this sensing platform include high sensitivity, real-time, and label-free detection. However, at terahertz frequencies, owing to the strong absorption of polar liquids, such as water, most of these studies have typically been limited to dry or partially hydrated specimens. Very few reports on direct liquid sensing based on terahertz metamaterials have been presented [109, 114-116, 118, 120]. Since most of the functionalities of chemical and biological materials are expressed in water, the key solvent of most biological substances, therefore, it is important to realize readily available and cost- effective sensing platforms for water-based real biological systems.

We demonstrate a cost-effective metamaterial sensor with a simple metallic structure but strong and sensitive multi-modal resonance for highly absorptive water- methanol mixtures. The metamaterial sensor that consists of asymmetric dual-wire arrays offers the ease of fabrication and exhibits multi-modal resonances, including a Fano resonance dip, a dipole resonance dip, and a Fano transmittance peak between the two dip resonances due to structural symmetry breaking. Predominantly, both resonances have strong intensity and are able to sense highly absorptive solutions. Sensing accuracy can be improved by detection of frequency shifts at multiple resonances. In addition, we use free-standing, transparent and thin Mylar substrate with a total thickness of 22 μm. The thin substrate with lower dielectric constant has lower influence on the capacitance of the resonators, thus enhancing the sensitivity [126-130][31–35]. We demonstrate that the proposed metamaterial sensor combined with terahertz time-domain spectroscopy (THz-TDS) could be effectively utilized in terahertz sensing of water-methanol mixtures with the capability to identify

solvent type and determine the corresponding concentrations. This work would motivate metamaterial- assisted terahertz sensing for chemical and biological substances in highly absorptive aqueous systems.

4.2 Metamaterial structure and simulation

Figure 4.1(a) shows the microscopic image of the proposed asymmetric dual-wire resonator (ADWR) with the inset showing the unit cell schematic. The unit structure is composed of two aluminum (Al) wires placed in parallel on the Mylar substrate. The detailed structural parameters are as follows: P_x = 80 μm, P_y = 126 μm, L_1 = 60 μm, (fix all subscripts issues) L_2 = 106 μm, d = 20 μm, and ω = 6 μm. The thicknesses of the Al and Mylar films are 200 nm and 22 μm, respectively. Numerical simulation of the ADWR was carried out using CST Microwave Studio frequency domain solver with tetrahedral mesh [131]. The Mylar substrate was modeled as a lossless dielectric with dielectric permittivity ε = 2.89 and the DC conductivity σ of Al was set to be 3.56×10^{-7} S/m.

4.3 Experiment

The ADWR was fabricated using the following processes: the dual-wire structures were first patterned on Mylar substrate by conventional photolithography using positive photoresist. A 200-nm-thick Al film was then thermally deposited and followed by lift-off process.

Double-distilled water (home-made) and methanol with a purity higher than 99.9% (Pharmco-AAper) were used in this work without further purification. The water-methanol mixtures were prepared with 0%, 30%, 50%, 70%, 100% (v/v %) water volume percentage.

The ADWR and water-methanol mixtures were measured by a traditional photoconductive switch-based THz-TDS system [115, 132][20, 37]. Figure 4.1(b) shows the schematic diagram of liquid sample measurement using ADWR-assisted THz-TDS. The ADWR was placed in a quartz cuvette composed of two parallel, 60-μm-spaced, and 1-mm-

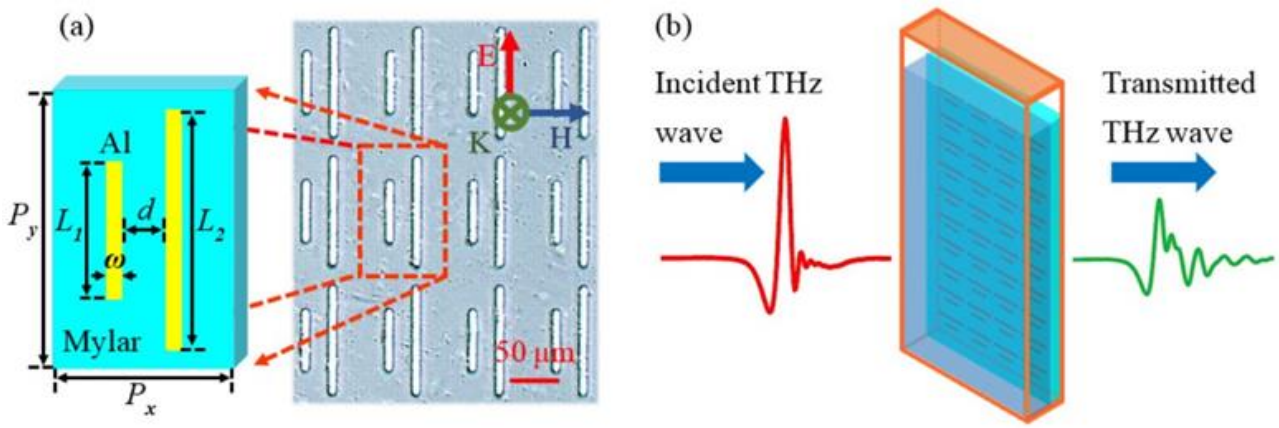

Fig. 4.1. Proposed asymmetric dual-wire resonator (ADWR).

(a) Microscopic image of the ADWR with the inset showing the schematic unit structure where Px = 80 μm, Py = 126 μm, L1 = 60 μm, L2 = 106 μm, d = 20 μm, and ω = 6 μm. (b) Schematic diagram of liquid sample measurement by ADWR combined with THz-TDS.

thick windows with the side of the Mylar substrate closely attached to one of the quartz windows. The liquid sample was then injected into the cuvette. The cuvette was sealed and placed midway between the transmitter and receiver in the focused beam of the THz-TDS system. The polarization of the incident terahertz field was parallel to the wires. An identical empty quartz cuvette was used as the reference. The amplitude transmission t(ω) was obtained by the following equation:

$$t(\omega) = |E_s(\omega)|/E_r(\omega), \qquad (4.1)$$

where $E_s(\omega)$ and $E_r(\omega)$ are the fast Fourier transformed (FFT) transmitted electric fields of the sample and the reference pulses, respectively, ω is the angular frequency. The average of three repeated transmission measurements was used for further analysis.

4.4 Analysis of simulation results

Figure 4.2(a) presents the simulated amplitude transmission of the ADWR and the two individual wire structures with L1 = 60 μm, L2 = 0 μm, and L1 = 0 μm, and L2 = 106 μm. The two individual bar structures resonated at two different frequencies due to their unequal wire lengths. The short wire resonated at a higher frequency, f = 1.695 THz, while the longer wire resonated at a lower frequency, f = 1.068 THz. However, once the two bars were placed together, the resonance in the coupled ADWR exhibited multi-modal resonances including an asymmetric resonance dip at 1.038 THz, a transmittance peak at 1.269 THz, and a symmetric resonance dip at 1.734 THz. It should be noted that the two resonance dips happened to be located near the two resonance dips of the individual wire arrays. The insets of Fig. 4.2(a) present the surface current distributions at the two resonance dips of the coupled ADWR. We observed Fano-like antiparallel currents at 1.038 THz and a dipole-like parallel currents at 1.734 THz.

In order to understand the mechanism of these multi-modal resonances especially the Fano resonance, we investigated the transmission responses of dual-wire resonators (DWRs) with different asymmetries. Figure 4.2(b) shows the

simulated amplitude transmission of the DWRs, including one perfectly symmetric dual-wire resonator (SDWR) with L1 = L2 = 60 μm and five ADWRs with L2 increasing from 60 to 120 μm, but a constant L1 = 60 μm. The other parameters of these DWRs remain unchanged as Px = 80 μm, Py = 126 μm, d = 20 μm, and ω = 6 μm. For the SDWR, there was only a single resonance at 1.824 THz observed in the transmission. However, when the two wires had different lengths, that is, the structural asymmetry was introduced, multi-modal resonances would appear. In addition, a gradual red shift was observed for both resonances, and the Fano resonances became significantly broader but stronger with the increase of the asymmetry. These phenomena could be contributed to the destructive interference between the two wires caused by symmetry breaking [133-136]. In the symmetric system, there was no destructive interference between the two wires, and hence only one broad dipole resonance in the transmission spectra is seen. However, once the structural symmetry is broken in the unit cell with two unequal lengths of wires, the destructive coupling at lower frequency leads to antiparallel surface current distribution that gives rise to the sharp Fano resonance. The surface current distribution at higher frequency is parallel in nature thus leads to dipolar resonance mode, as shown in the inset of Fig. 4.2(a). When the length difference between the two wires was increased, the Q factor of the Fano resonance dip was declined with increasing resonance intensity, as shown in Fig. 4.2(b). We further investigated the sensitivity of the Fano and dipole resonance dips in the ADWRs with varying L2 shown in Fig. 4.2(b) using rigorous simulations. The shifts in the resonance frequency at 4 μm analyte thickness and varying refractive index from n = 1.0 to n = 1.6 with an incremental step of 0.2 were calculated. Table 4.1 lists the simulated Fano and dipole resonances sensitivities in terms of change in resonance frequency per refractive index unit (RIU) of the analyte and Fano resonance intensities of the ADWRs. The Fano resonance intensity here was defined as the power transmission (the square of the amplitude transmission) difference between the Fano resonance dip and the Fano transmittance peak.

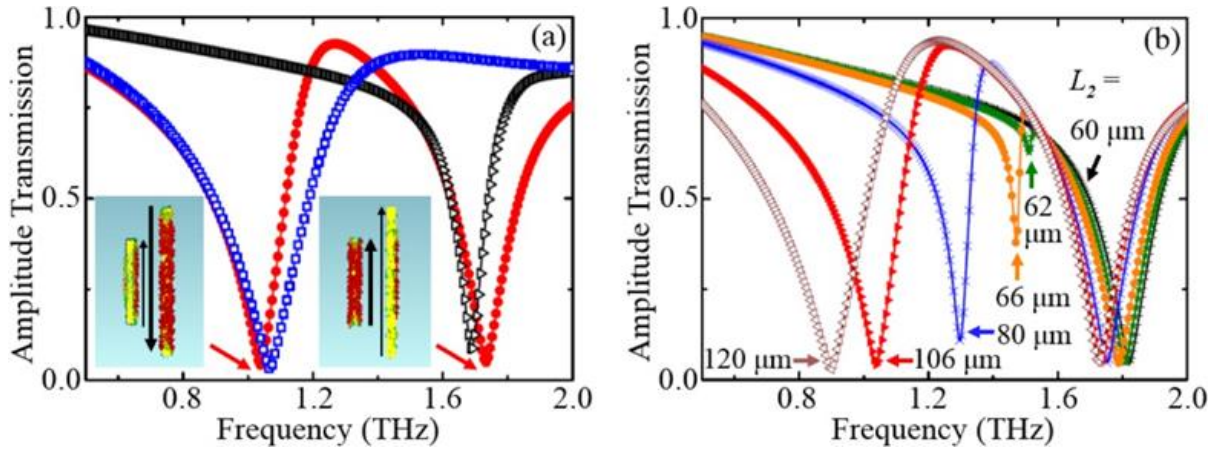

Fig. 4.2. Simulated transmission

(a) the ADWR with L1 = 60 μm, L2 = 106 μm (red solid circle) and the two individual wire structures with L1 = 60 μm, L2 = 0 μm (black triangle) and L1 = 0 μm, L2 = 106 μm (blue square) with the insets depicting the surface current distributions of the ADWR at 1.038 and 1.734 THz, and (b) DWRs with different asymmetries where L2 was increased from 60 to 120 μm, but a constant L1 = 60 μm.

L_2(um)	Fano		Dipole
	Sensitivity	Intensity	Sensitivity
62	268	0.075	200
66	266	0.414	217
80	217	0.744	220
106	176	0.861	245
120	161	0.877	258

Table.4.1. Summary of Resonance sensitivity

Summary of the simulated Fano and dipole resonances sensitivity (unit: GHz/RIU) and Fano intensity of the ADWRs with varying L_2 (unit: μm).

When the length difference between the two wires was increased with the increasing L2, the Fano resonance sensitivity was gradually decreased from 268 to 161 GHz/RIU, while the dipole resonance sensitivity was gradually increased from 200 to 258 GHz/RIU and even higher than the Fano resonance sensitivity when L2 exceeded 80 μm, as shown in Table 4.1.

In a typical Fano resonance, the resonance linewidth is narrower than dipolar resonances. However, sharp Fano resonances also suffer from the problem of having very weak resonance intensities [136]. Since the absorption of the analyte in our case was extremely large, a weakly excited Fano resonance would not be enough to sense the absorptive analytes. Therefore, in order to enhance the intensity of the Fano resonance, we increased the asymmetry parameter in the structure which lead to large broadening of the Fano resonance along with simultaneous enhancement in the resonance intensity. The broadening of Fano resonance even exceeded the linewidth of the dipolar resonance which explains the higher sensitivity of the dipolar resonance, as shown in Table 4.1. Though the Fano resonance sensitivities of the ADWRs with L2 below 106 μm were higher, their intensities were below 0.8. Therefore, we selected the ADWR with L1 = 60 μm and L2 = 106 μm for further experimental study of highly absorptive water-methanol mixtures. From our observation of the simulated electric fields, the Fano resonance of the selected ADWR shows super-radiative excitation of fields and the higher frequency dipolar resonance shows the sub-radiative fields where the longer metallic bar almost remains unexcited and the intense electric fields are confined on the smaller metal bar, as shown in Fig. 4.3. Therefore, the dipole resonance here has narrower resonance linewidth and higher sensitivity than Fano.

We also investigated the single dipole resonance sensitivity for single wire structures with varying wire length L increased from 60 to 120 μm. The single dipole resonance sensitivity was gradually decreased from 277 to 161 GHz/RIU with increasing L. Even though the highest dipole resonance sensitivity of single wire structure (277 GHz/RIU) was a little higher than the dipole resonance sensitivity of the selected ADWR (245 GHz/RIU), the selected

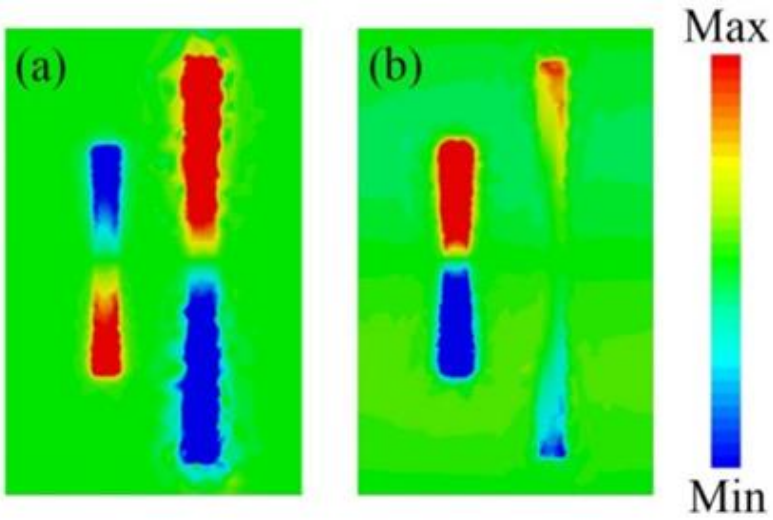

Fig. 4.3. Simulated electric field distribution of ADWR

with L1 = 60 μm and L2 = 106 μm at (a) at 1.038 THz, Fano resonance dip and (b) 1.734 THz, dipole resonance dip without analyte coated on the metasurface.

ADWR has particular importance in material sensing due to its improved sensing accuracy by detection of frequency shifts at multiple resonances. Besides, the Fano resonance dip sensitivity of the selected ADWR (176 GHz/RIU) was significantly higher than the reported terahertz asymmetric split ring (TASR) with identical analyte thickness (36.7 GHz/RIU)[122] .

4.5 Analysis of experimental results

We first measured the terahertz transmissions of the water-methanol mixtures in a quartz cuvette without ADWR and extracted the refractive indices of different water contents for subsequent measurements with ADWR. Figure 4.4(a) depicts the measured frequency- dependent amplitude transmissions of the water-methanol mixtures with various water contents from 0% (pure methanol) to 100% (pure water) at 0.5-2 THz. The measured amplitude transmission of different water-methanol mixtures was decreased with increasing water content due to stronger absorption of water than methanol. The refractive indices n(ω) of different water-methanol mixtures was derived from the transmission results by the following equation[137, 138] .

$$n(\omega) = \frac{c|\Phi_s - \Phi_r|}{\omega d} + n_r, \qquad (4.2)$$

where Φ_s and Φ_r are the phases of the sample and reference, respectively, c is the speed of light, ω is the angular frequency, d is the thickness of the liquid sample, and n_r is the refractive index of the reference. Figure 4.4(b) presents the frequency-dependent refractive indices of different water-methanol mixtures. The refractive indices of the water-methanol mixtures increased with increasing water content due to higher refractive index of water. The refractive indices of pure methanol and pure water, as shown in Fig. 4.4(b), agreed well with previous works[139, 140].

Subsequently, we measured the water-methanol mixtures with ADWR. Figure 4.5(a) shows the measured amplitude transmission of the bare ADWR metamaterial. The simulated amplitude transmission was also shown for comparison.

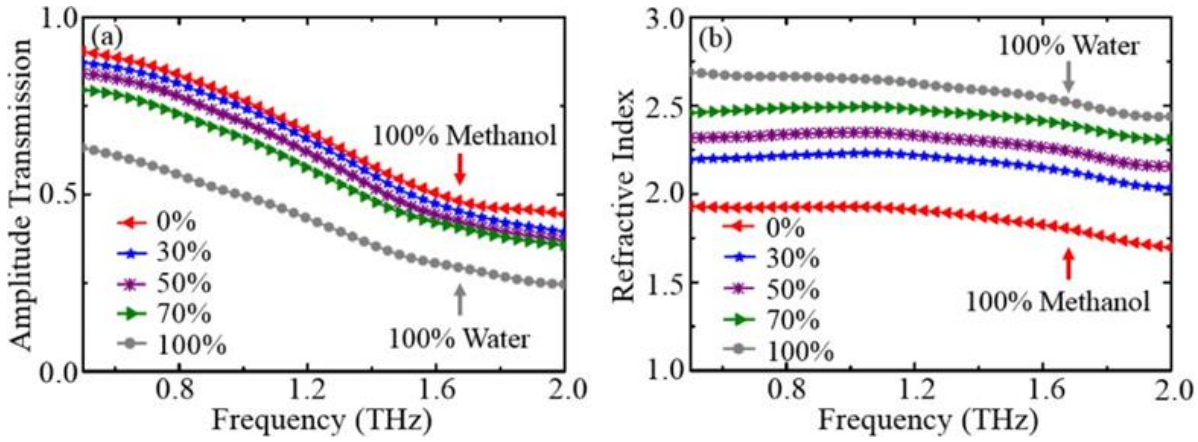

Fig. 4.4. Measured Transmission and refractive indices

(a) Measured transmission and (b) refractive indices of the water-methanol mixtures with different water contents ranging from 0% to 100%.

We can observe that the experimental amplitude transmission of the bare ADWR is in good agreement with the simulation. In order to increase the difference between water-methanol mixtures measured by ADWR-assisted THz-TDS, we used the normalized transmittance method. The normalized amplitude transmission T(ω) of water-methanol mixtures measured by the ADWR-assisted THz-TDS was obtained by the following equation: mixtures measured by the ADWR-assisted THz-TDS was obtained by the following equation:

$$T(\omega) = \frac{t_{mixture+ADWR}(\omega)}{t_{methanol}(\omega)}, \qquad (4.3)$$

where $t_{mixture+ADWR}(\omega)$ is the amplitude transmission of water-methanol mixtures measured by the ADWR-assisted THz-TDS, $t_{methanol}(\omega)$ is the amplitude transmission of 100% methanol obtained by THz-TDS without ADWR shown in Figure. 4.5(a), and ω is the angular frequency. Figure 4.5(b) presents the normalized amplitude transmission T(ω) of the water-methanol mixtures with ADWR. A gradual red shift was observed at all resonances (Fano resonance dip, Fano transmittance peak, and dipole resonance dip) with increasing water contents due to the increasing refractive indices of the water-methanol mixtures under test at the resonance frequency. Besides, the amplitude transmission of water-methanol mixtures at the Fano transmittance peak with ADWR decreased with the increase of water content which was similar to the trend obtained with traditional THz-TDS without ADWR shown in Figure 4.4(a). A clearer difference in the amplitude transmission between different water contents was observed in the Fano transmittance peak using ADWR, which demonstrates a higher sensitivity of the ADWR-assisted THz-TDS than the conventional THz-TDS.

We plotted the resonance frequency shift against the refractive index of the water- methanol mixture for all resonances in Fig. 4.6(a). Sensitivities of the Fano resonance dip, Fano transmittance peak, and dipole resonance dip turned out to be 93, 160, and 305 GHz/RIU, respectively. Note that even though, the sensitivity at Fano resonance dip and dipole resonance dip seems not to be so distinctive, the calculated sensitivities clearly prove otherwise. More importantly,

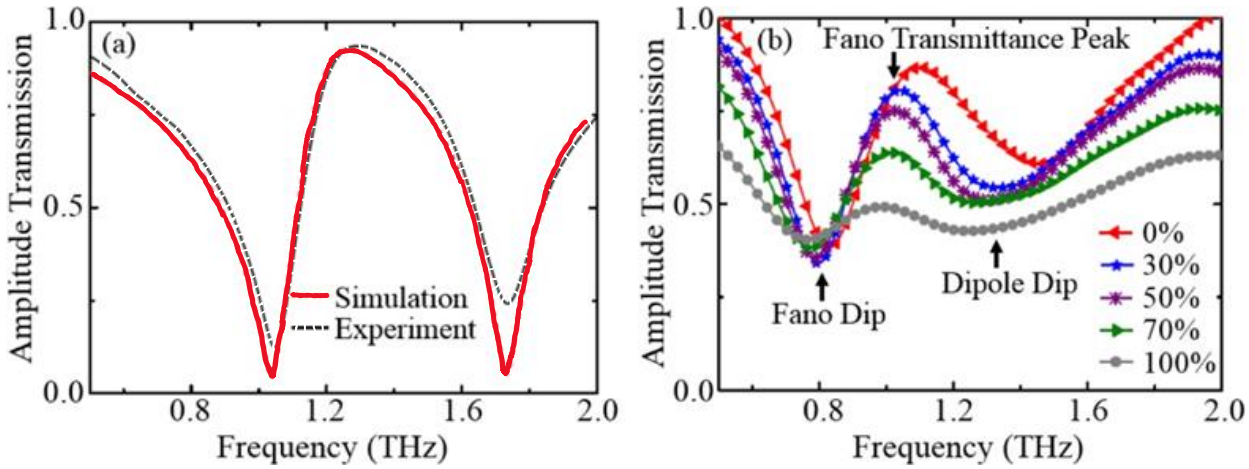

Fig. 4.5. Experimental vs Simulated transmission

(a) Experimental and simulated transmission through the bare ADWR metamaterial. (b) Normalized measured transmission of the water-methanol mixtures obtained by ADWR- assisted THz-TDS.

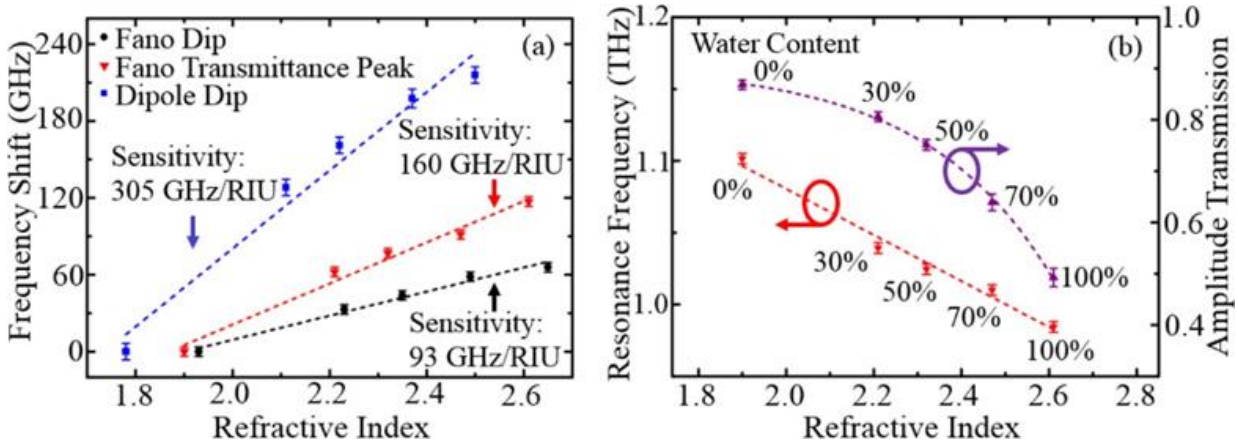

Fig. 4.6. Measured frequency shifts

(a) Fano resonance dip, Fano transmittance peak, and dipole resonance dip with the changes of refractive indices of different water contents. (b) Resonance frequencies and transmission values of the Fano transmittance peak with the changes of refractive indices of different water contents.

the amplitude of the Fano transmittance peak fitted exponentially with the changes of the refractive indices or the concentrations of water in the mixtures and their resonance frequencies were linear fitted with the changes in refractive indices when measuring with ADWR, as shown in Fig. 4.6(b). Thus we are able to realize qualitative and quantitative sensing of methanol and water simultaneously with ADWR- assisted THz-TDS.

4.6 Conclusion

By breaking the symmetry of dual-wire structures via unequal lengths, we obtained a readily available metamaterial with multi-modal resonances in the terahertz regime. By further optimizing the geometry design, a practicable terahertz metamaterial sensor with strong multi-modal resonances and high sensitivities was achieved for efficient sensing of strongly absorptive water-methanol mixtures. The experimental results of the water-methanol mixtures sensing show that the demonstrated metamaterial achieves frequency sensitivities of 93, 160, and 305 GHz/RIU for the Fano resonance dip, the Fano transmittance peak, and the dipole resonance dip, respectively. This metamaterial presents a promising avenue for highly accurate, cost-effective, label-free, real-time, qualitative and quantitative terahertz sensing of chemical and biological substances in water, methanol, and other types of highly absorptive aqueous systems. As for the real measurements of biological materials, the sensitivity and selectivity of the proposed metamaterial can be further improved by optimizing the structural parameters to match the resonance frequencies of the objective biological molecule and specific chemical reaction between the biological target and binding agents immobilized on the metamaterial. Real-time monitoring can be achieved by integrating with microfluidic devices.

ACKNOWLEDGEMENT: This chapter has been previously published as, “M. Chen, L. Singh, N. Xu, R. Singh, W. Zhang, and L. Xie, Terahertz sensing of highly absorptive water-methanol mixtures with multiple resonances in metamaterials, Optics express, vol. 25, pp. 14089-14097, 2017”.

CHAPTER V

BANDWIDTH BROADENING OF A LINEAR POLARIZATION CONVERTER BY NEAR-FIELD METASURFACE COUPLING

We experimentally demonstrate a highly efficient, broadband linear polarization converter functioning at terahertz frequencies. The linear polarization converter is composed of three metasurfaces and two dielectric layers interlaced with each other. The neighboring unit cells of the central metasurface layer of the linear polarization converter exhibit strong electromagnetic coupling, which increases the number of resonances and results in significant bandwidth broadening. The simulation and experimental results show that in the frequency range of 0.2 to 0.4THz, the proposed polarization converter has a flat transmission curve and exhibits a transmission efficiency that is higher than 80%. High performance terahertz polarization conversion is desirable in many fields, such as terahertz spectroscopy, imaging, and communications.

5.1 Introduction

The rapid advancement of terahertz science has led to the development of many practical applications in the fields of imaging, sensing, communications, and biomedicine[141-143]. For these applications, high-performance terahertz components, such as modulators[144, 145], lenses[146], wave plates[147], switches, and polarization converters[148-150], are essential for terahertz wave manipulation. Conventional polarization devices are generally realized by using birefringence in nematic liquid crystals or polymers[147-151] and are based on the mechanism of phase retardation between the two orthogonally polarized waves propagating along the device. Therefore, conventional polarization devices usually require a specific thickness and bulky configurations to obtain sufficient phase accumulation[152, 153]. It is extremely challenging to integrate these polarization converters within ultra-thin devices, such as advanced sensors and nanophotonic devices. Thus, novel approaches are desired to control the polarization state of the electromagnetic waves.

Metasurfaces, which are planar, two-dimensional, artificially engineered materials, have attracted extensive research interest for many potential applications[154-156]. By rationally designing the unit cells of the metasurfaces, one can achieve many interesting electromagnetic (EM) properties that have not yet been found in natural materials. Thus, metasurfaces provide a novel way to manipulate EM waves, including their polarization state. In recent years, many metasurface based polarization devices with diverse functionalities, such as linear to linear, linear to circular, and circular to circular polarization conversion, have been demonstrated[157-159]. The polarization converters that function in transmission mode usually have the disadvantages of being narrowband and having a low polarization conversion efficiency. Hence, most of the high-performance devices operate mainly in reflective mode. Although a few novel metasurfaces have been proposed to improve the performance of the transmission polarization converter[160, 161], achieving a high conversion efficiency over a broad bandwidth remains challenging.

In this letter, we present a linear polarization converter operating in transmission mode at terahertz frequencies. We experimentally and theoretically demonstrate that the proposed polarization converter is able to rotate linearly polarized EM waves by 90° in a broad bandwidth ranging from 0.2 to 0.4 THz and with an over 80% polarization conversion efficiency. Compared with other types of polarization converters[150, 160, 162], the high conversion efficiency bandwidth of the proposed polarizer is effectively extended.

5.2 Design and measurement

A schematic configuration of the proposed transmission-mode linear polarization converter is described in Figure 5.1(a). It consists of two metallic gratings, a double L-shaped metasurface and two dielectric plates. Mylar ($\varepsilon = 3.1 + 0.02i$) films with thickness $t = 75$ μm are used as the dielectric plates, which are employed to separate the metallic gratings and the double L-shaped metasurface due to Mylar's low dielectric losses. The two identical gratings with geometric parameters $g = 25$ μm and $g_1 = 50$ μm are placed orthogonal to each other.

Figure 5.1(b) shows the unit cell design of the middle layer metasurface, which consists of two L-shaped plasmonic antennas. The parameter α denotes the angle between the two arms of the L-shaped structure. Figure 5.1(c) illustrates the optical images of the fabricated sample, in which the light-colored parts are metal with a thickness of 0.2 μm. For any L-shaped structure, there are three regions (marked as regions I, II, and III in Fig. 5.1(c)) separated by only a short distance, d, where either the two arms or the corner angle of the L-shaped structure is closer to the counterpart of its neighboring L-shaped structure (see Fig. 5.1(c)). Because of this short distance d, significant EM mutual coupling usually occurs in these regions. In the following content (see section 5.3. Physical mechanism), we find that this EM mutual coupling in the three regions is the main contributor that leads to the performance enhancement of the proposed polarization converter. Furthermore, the distance d can be easily changed by altering the relative position of the two

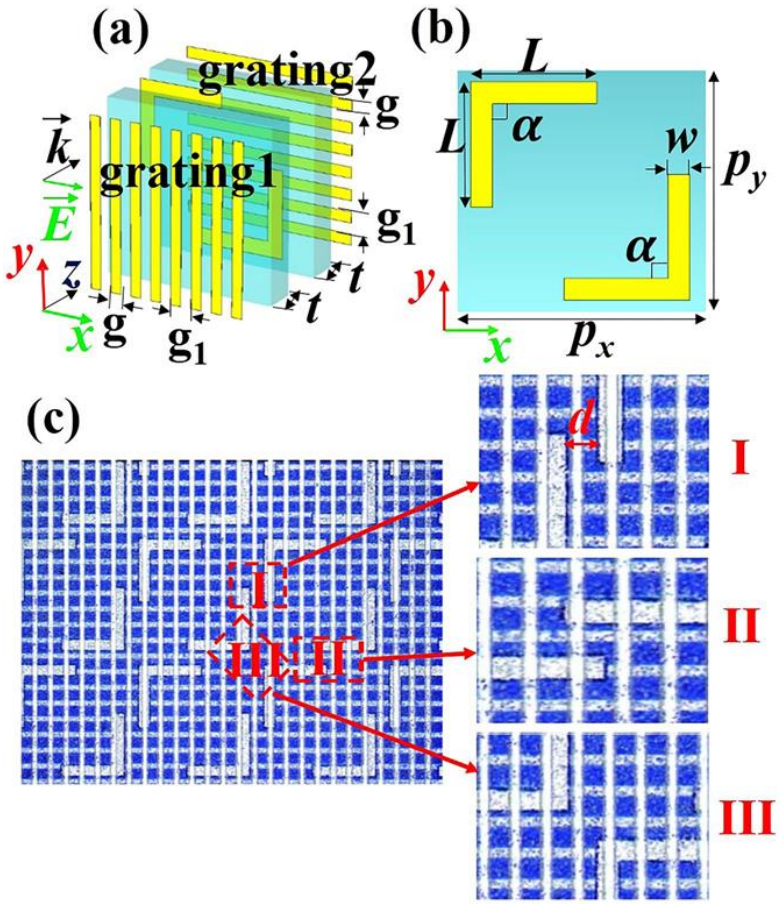

Fig. 5.1. Proposed polarization converter

(a) Unit cell of the proposed polarization converter consisting of two gratings, a double L-shaped metasurface, and two dielectric plates. (b) Front view of the metasurface unit cell. (c) Optical image of the fabricated sample. The geometric parameters are t = 75 μm, g = 25 μm, g1 = 50 μm, px = py = 400 μm, L = 200 μm, w = 35 μm, and α = 90°. The periodic lattices are along the x and y directions, and the EM waves propagate along the z direction. The regions I, II and III, surrounded by the square frame, denote the EM mutual coupling areas of a unit cell with neighboring unit cells

L-shaped structures, which makes it convenient to adjust the EM mutual coupling in regions I, II, and III to optimize the device performance.

To demonstrate the performance of the proposed polarization converter, we fabricated the sample and measured its transmission coefficient. Figure 5.1(c) shows the fabricated sample of the proposed device. We define

$$t_{xy} = |E_{yt}/E_{xi}|^2, \qquad (5.1)$$

$$r_{xx} = |E_{xr}/E_{xi}|^2, \qquad (5.2)$$

to denote the transmission and reflection coefficients. Here, E_{yt}, E_{xi}, and E_{xr} denote the electric fields of the y-polarized transmission wave, x-polarized incident wave, and x-polarized reflected wave, respectively.

The polarization converter shown in Fig. 5.1(a) was fabricated with conventional photolithography and metallization processes. We start fabrication with two 75 μm thick sheets of Mylar. The double L-shaped metasurface and the grating are fabricated on the two sides of the first Mylar sheet; the other orthogonal grating is fabricated on the second Mylar sheet. Then, with the help of a microscope, we assemble the two structured Mylar sheets using the alignment shown in Fig. 5.1(a).

Figure 5.1(c) illustrates optical images of the fabricated sample, which contains 37 × 37 unit cells with an over- all size of 15 × 15 mm^2. The sample is experimentally characterized using broadband (0.1–4.5 THz) terahertz time-domain spectroscopy (THz-TDS). Specifically, the system consists of four parabolic mirrors placed between the transmitter and receiver, which are arranged in an 8-f confocal geometry enabling a frequency independent beam waist of 3.5 mm on the sample. An x-polarized (TE-polarized) light irradiates from the left side to excite the device (see Fig. 5.1(a)). On the other side of the sample, a polarizer is placed in a plane parallel to the xy-plane. The

polarization direction of the polarizer is 45° with respect to the x-axis so that the cross-linear polarization transmission coefficient can be measured.

5.3 Physical mechanism

Figure 5.2(a) illustrates the amplitude of the cross-polarized (y-polarized) transmission coefficient for the x-polarized incident wave. It can be observed that the measured result agrees well with that of the simulation. In the experimental result, there is a frequency shift of approximately 0.02 THz, which may be caused by tolerances in the fabrication and measurement processes. From Fig. 5.2(a), we can also see that the proposed device shows a more than 88% transmission efficiency in the frequency range of 0.17 to 0.39 THz in the simulation. The measurement result reveals that the sample exhibits a more than 80% transmission efficiency in the broad bandwidth from 0.21 to 0.41 THz.

To elucidate the physical process of polarization conversion, the electric field distribution in the cross-section shown in Fig.5.2(b) was simulated. Figure.5.2(c) illustrates the simulated result. When an x-polarized EM wave impinges onto the device from the +z direction, it first couples with grating 1 and is then rotated into a y-polarized EM wave by the metasurface layer. The rotated y-polarized EM wave then couples with the right side of grating 2. Consequently, the incident x-polarized wave is converted into a y-polarized wave when it passes through the polarization device. In this physical process, the dielectric losses due to the dielectric spacer and the electrical characteristics of the double L-structured metasurface directly impact the performance of the polarized device, including the bandwidth and the transmission efficiency of the proposed device. To demonstrate this, we investigated the polarization conversion of the proposed device with different losses in the dielectric spacer and different values of α (see Fig. 5.1(b)) by using the commercial software CST Microwave Studio.

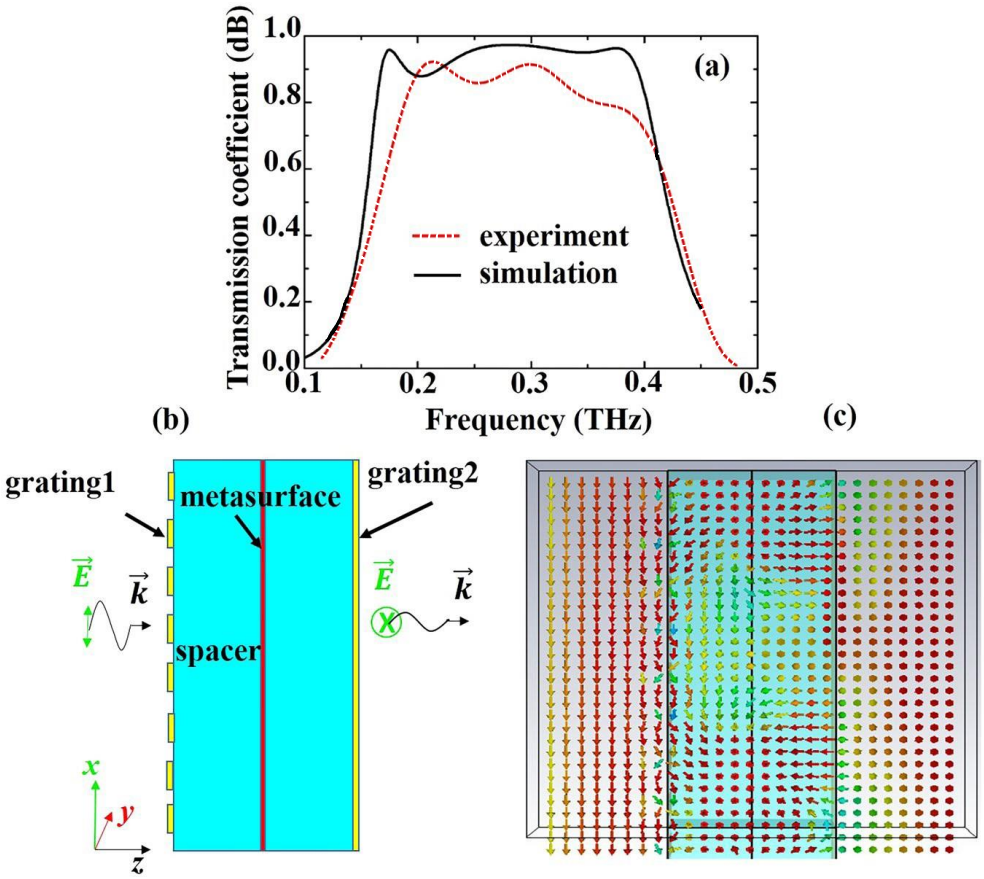

Fig. 5.2. Transmission Spectra and electric field

(**a**) Measured and simulated transmission spectra (t_{xy}) of cross-polarization. (**b**) Cross section (in the *xz* plane) of the proposed polarization converter. (**c**) Simulated electric field distribution in the cross section, which describes the polarization conversion process when the *x*-polarized EM wave propagates along the *z* -direction. The arrows denote the direction of the electric field

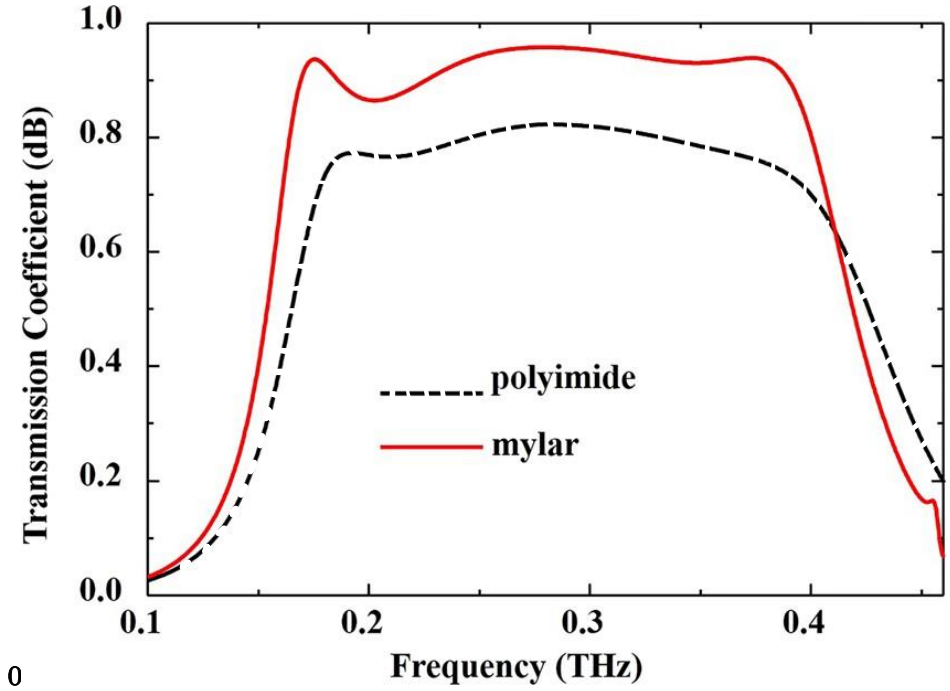

0

Fig. 5.3. Dielectric spacer transmission coefficient

Transmission coefficient (t_{xy}) for different dielectric spacers. The dielectric constants of polyimide and Mylar are 3.0 + 0.15*i* and 3.1 + 0.02*i*, respectively

Figure 5.3 shows the comparison of cross-polarization transmission coefficient (t_{xy}) for different dielectric spacers when other parameters are fixed. From Fig. 5.3, we can clearly see that the dielectric losses in the spacer can significantly affect the transmission efficiency of the device. When Mylar, with its low dielectric losses, is used as spacer, the transmission efficiency of the device is increased by approximately 15%. Therefore, we used Mylar as the dielectric spacer in our design.

To investigate the performance of the device for different values of α, we first defined

$$B_f = 2 * (f_h - f_l)/(f_h + f_l), \qquad (5.3)$$

to denote the relative bandwidth, where f_h and f_l are, respectively, the upper and lower cutoff frequencies of the operation bandwidth. Figure 5.4 illustrates the transmission and the reflection coefficients for the three typical angles (α = 0°, 45°, and 90°). As shown in Fig. 5.4(a), the parameter α can effectively impact the bandwidth and the transmission efficiency of the polarization device. When α = 90°, the cross-polarization transmission coefficient (t_{xy}) in the frequency range from 0.16 to 0.39 THz is greater than −1.1 dB, resulting in the relative bandwidth being 83.6%. When α is reduced to 45°, the relative bandwidth with txy over −1.1 dB is decreased to 66.6% (from 0.21 to 0.42 THz). Whereas when α is equal to 0°, the relative bandwidth is reduced to 16.2% (from 0.34 to 0.4 THz). Figure 5.4(b) illustrates the co-polarized reflection coefficients (r_{xx}), from which we see that different α values correspond to different resonances. For α = 0°, the metasurface has only one resonance corresponding to f = 0.381 THz. When α increases to 45°, two resonance peaks appear at frequencies 0.282 and 0.396 THz. However, for α = 90°, three resonance peaks appear at 0.17, 0.28, and 0.37 THz, showing that the metasurface is a multi-resonance system when α is equal to 45° and 90°.

To understand the physical mechanism of the multi-resonance system in further detail, we investigated the surface current and electric field distributions on the double L-shaped metasurface at α = 0°, 45° and 90°. For each value of

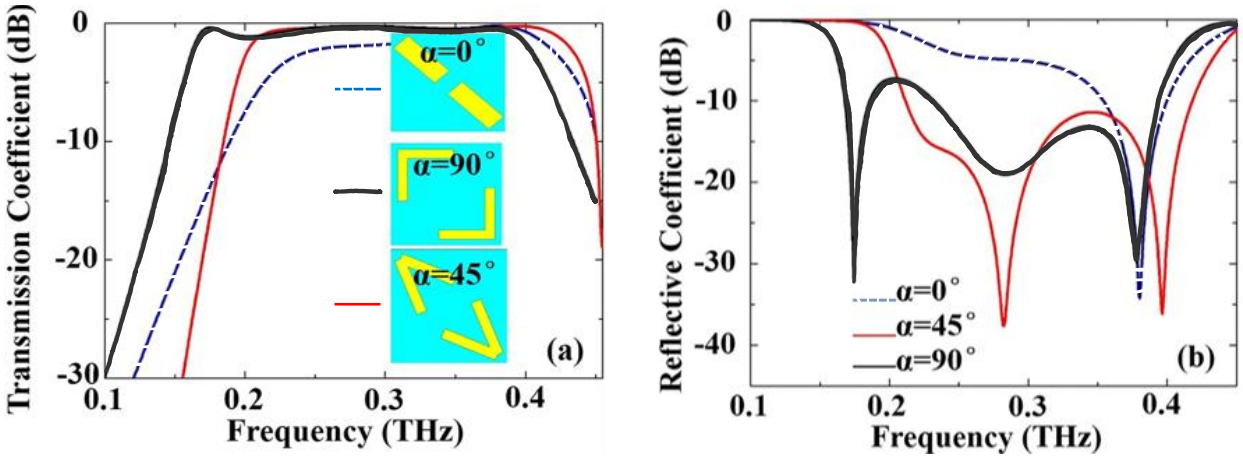

Fig. 5.4. Simulated coefficients

Simulated transmission (t_{xy}) and reflection (r_{xx}) coefficients for different α. The insets show the front view of the center metasurface layer for different α

α, we probed all the resonance frequencies, and the simulation results are shown in Figs 5.5 and 5.6. When α is equal to 0°, the double L-shaped structure is changed into a pair of cut wires, which is marked as a unit cell in Fig. 5.5(a). In this case, these cut wires can be considered equivalent to a LC resonant circuit that has only one resonance frequency at 0.381 THz. The surface current distribution shown in Fig.5.5(a) verifies the LC resonance characteristic. On the other hand, we note that the distance (d) between the unit cell and its neighboring structure is the greatest, implying weak mutual coupling in this case. This decoupling characteristic can be further demonstrated by the electric field distribution (see the lower part in Fig.5.5(a)), in which the largest electric field appears in only the gaps of the unit cell. When α is greater than 0° and less than 90°, for example, α = 45°, the metasurface acquires a double V-shaped structure, as shown in Fig.5.5(b). According to reference[163], the V-shaped plasmonic antenna can support two typical modes, the antisymmetric and symmetric modes. The current distributions for these modes are along the red arrows, as shown in Fig.5.5(b). These different current distributions make the V-shaped metasurface resonate at two different frequencies (0.282 and 0.396 THz). Due to the existence of the two resonances, the bandwidth and cross-polarization efficiency for α = 45° are obviously improved. From the electric field distributions (see the lower parts in Fig.5.5(b)), we see that at both resonances, the electric field in region II is very weak, which verifies the decoupling characteristic in this region. However, in region III, the electric field becomes strong, implying the enhancement of the EM mutual coupling

EM mutual coupling strengths in different regions cause the redistribution of the surface current, which leads to different electrical lengths and, consequently, different resonance frequencies. For the symmetric mode, the metasurface with α = 90° (Fig.5.6), has a similar surface current as that with α = 45° (Fig.5.5(a)).

Comparing the black line and the red line shown in Fig.5.4(b), we observe that the resonance frequency of the symmetric mode for α = 90° is lower than that for α = 45°. This phenomenon can be explained in terms of EM mutual coupling. In the double L-shaped metasurface (α = 90°), there are three EM mutual coupling areas (regions I, II and

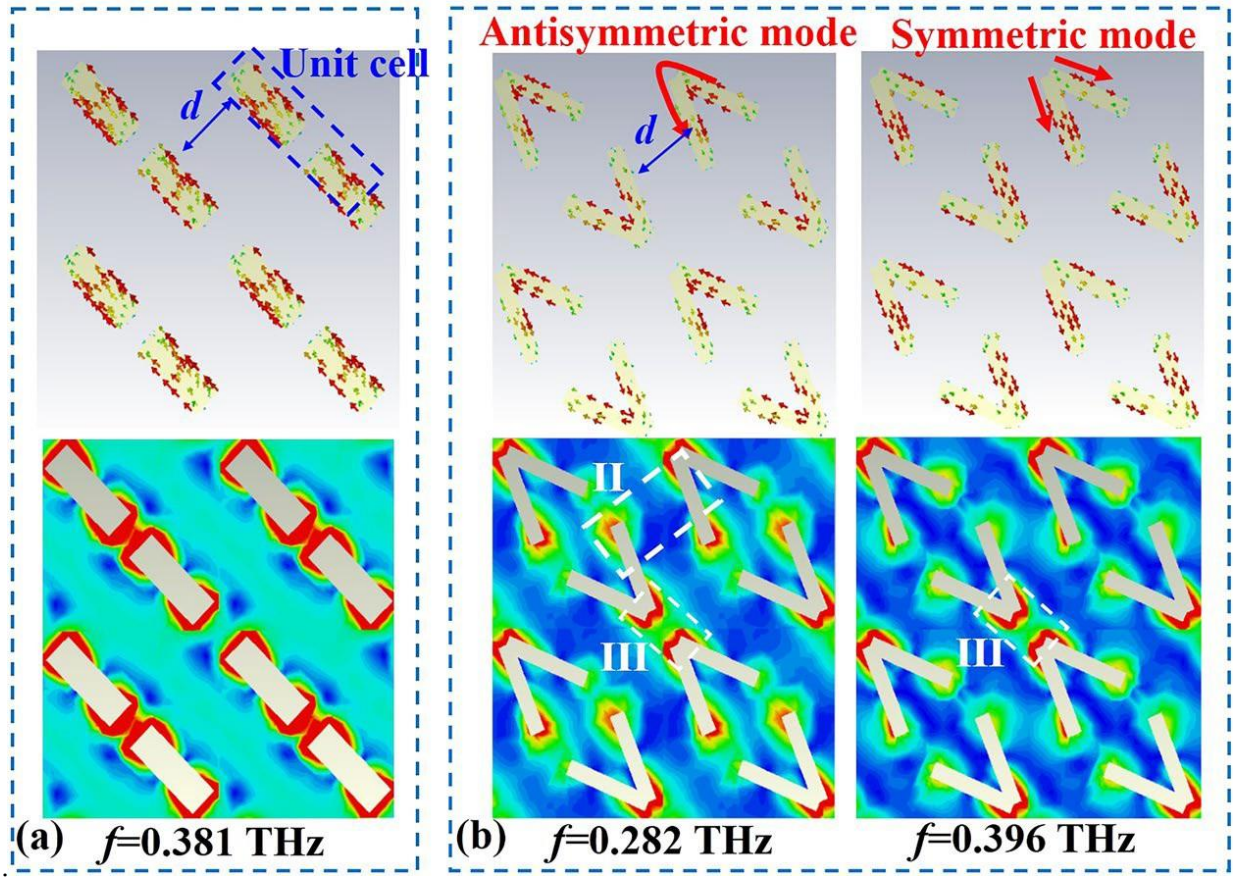

Fig. 5.5. Electric field and surface current at varying α

Surface current (upper parts) and electric field (lower parts) distributions on the middle metasurface; the red arrows denote the direction of surface current. (**a**) α = 0° and (**b**) α = 45°.

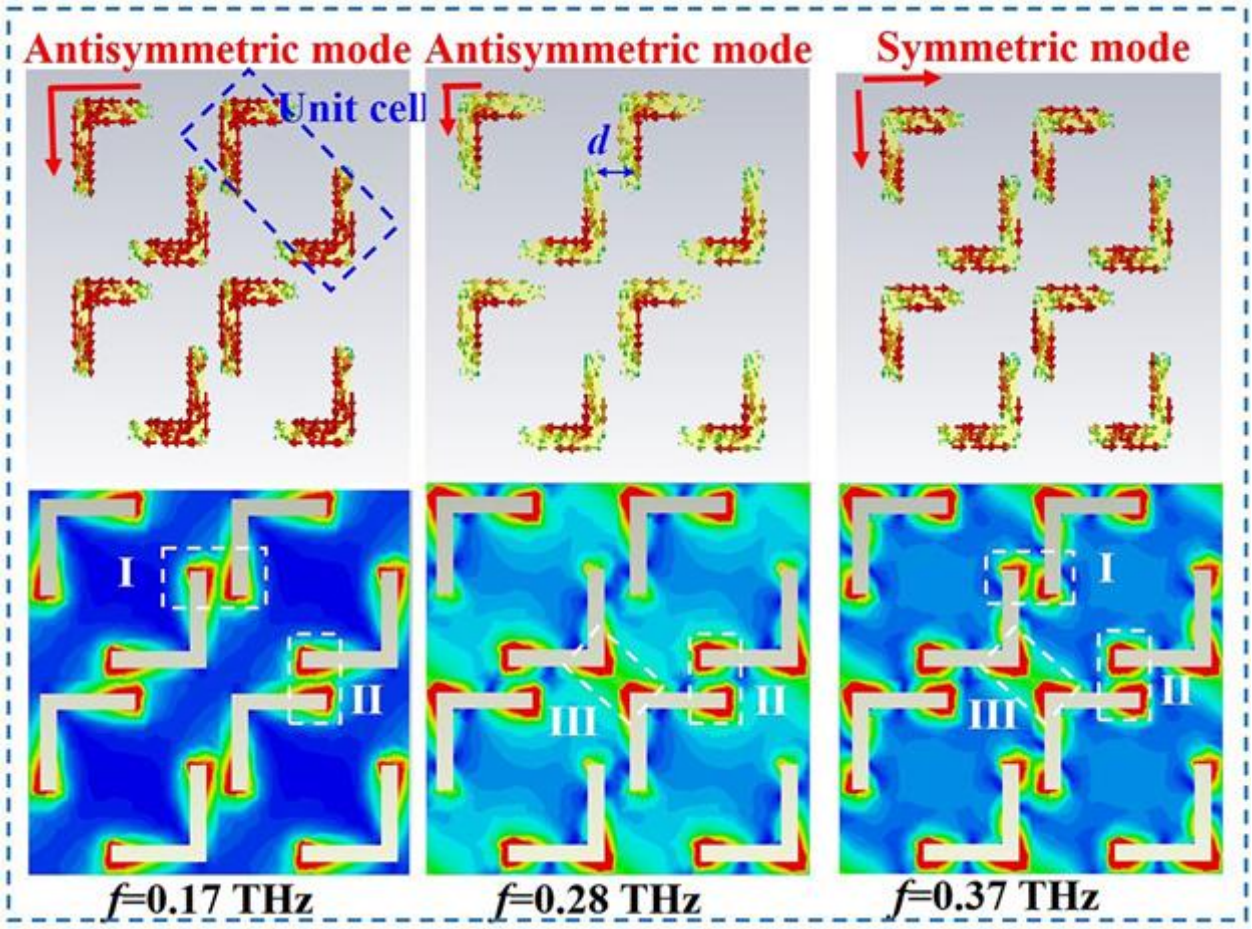

Fig. 5.6. Electric field and surface current at varying α = 90°

Surface current (the upper parts) and electric field distributions (the lower parts) on the metasurface layer with α = 90°.

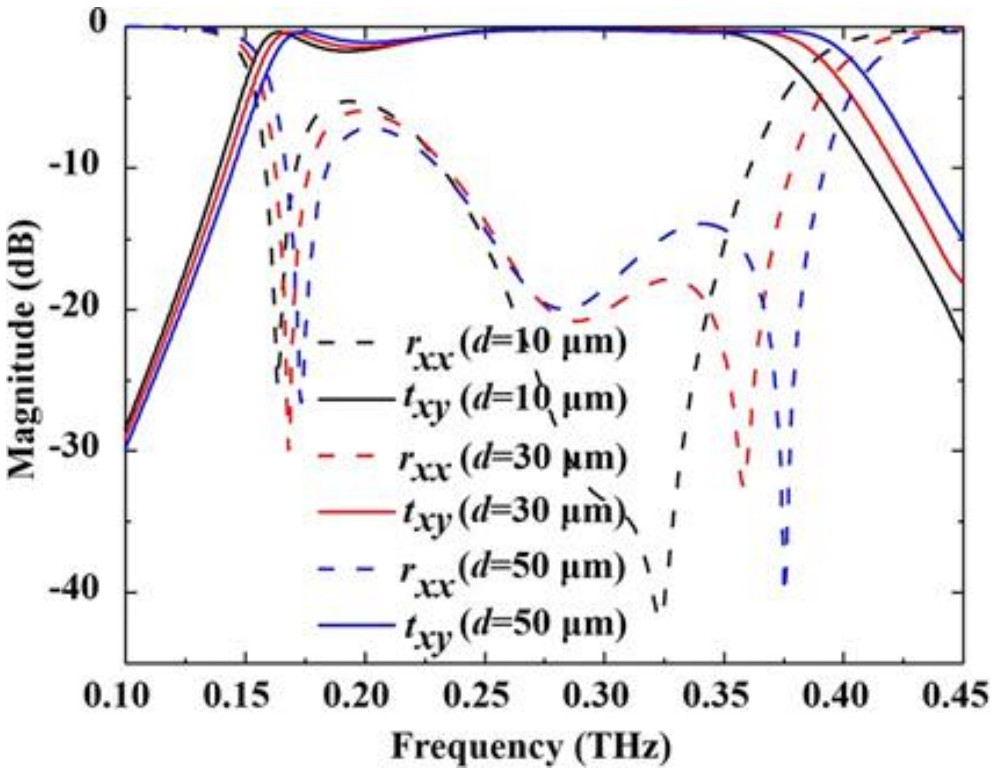

Fig. 5.7. Varying the value of the parameter d

Simulated transmission (t_{xy}) and reflection (r_{xx}) coefficients for different d in the double L-shaped metasurface when other parameters are fixed. The solid lines correspond to t_{xy}, and the dashed lines are r_{xx}.

III), whereas in the double V-shaped structure ($\alpha = 45°$), only one region (III) shows strong mutual coupling. These results demonstrate that the multi-resonance characteristic of the double L-shaped meta- surface results from the symmetric and antisymmetric modes, supported by the L-shaped antenna and the different EM mutual coupling between the neighboring unit cells, respectively. This multi-resonance characteristic plays a crucial role in significantly improving the performance of the proposed polarization device, including the bandwidth and the transmission efficiency enhancement.

For the double L-shaped metasurface ($\alpha = 90°$), we also investigated the influence of parameter d on the performance of the proposed polarization converter. Here, we take three typical values of d, such as 10, 30 and 50 μm. Figure 5.7 shows the simulated transmission (t_{xy}) and reflection (r_{xx}) coefficients for the three d values. From the reflection coefficients, we see there are two resonances when d = 10 μm and that there are three resonances when d = 30 μm and 50 μm. Furthermore, these resonant frequencies show a blue shift when d is increased from 10 μm to 50 μm. The transmission coefficients also reveal that the device performance depends on the value of d. When the distance d is altered, the EM mutual coupling between the neighboring unit cells should be changed accordingly. The changed EM mutual coupling affects the resonance of the double L-shaped metasurface and further influences the performance of the proposed polarization device. So, the device performance can be optimized by choosing the appropriate value of the parameter d.

5.4 Conclusion

We have experimentally demonstrated that a metasurface consisting of double L-shaped plasmonic antennas can convert linear polarized waves into their cross-polarized waves over a broad bandwidth, ranging from 0.2 to 0.4 THz, with more than 80% transmission efficiency. We have also investigated the physical mechanism using numerical simulations. It is observed that by employing the L-shaped structure, the plasmonic antenna shows EM mutual

coupling with neighboring antennas in different regions. Such mutual coupling behavior enables the metasurface to be a multi-resonance system and significantly affects the working bandwidth and transmission efficiency. By adjusting the mutual coupling reasonably, a polarization converter with good performance can be achieved. The demonstrated metasurface based polarization converter is an essential step toward high-performance integrated terahertz devices.

ACKNOWLEDGEMENT: This chapter has been previously published as, "X. Gao, L. Singh, W. Yang, J. Zheng, H. Li, and W. Zhang, Bandwidth broadening of a linear polarization converter by near-field metasurface coupling, Scientific reports, vol. 7, p. 6817, 2017".

CHAPTER VI

SUMMARY AND FUTURE WORK

A systematic and detailed study of refractive index engineering and various techniques used to achieve high refractive index values has been presented. Later this research work presented a novel method to obtain even high refractive index values using deep sub-wavelength coupling in a flexible free-standing substrate. The excellent overlap between the simulated and experimental results unveils the effectiveness of this technique. Furthermore, two set of universal law behaviors has been presented that can be used for obtaining specific value of refractive index at a particular value of frequency in Terahertz range. Thus, offering an elegant solution for achieving required high refractive index values at Terahertz frequencies. However, some more detailed study of this technique utilizing deep subwavelength coupling needs to be carried out , inorder to provide clear understanding of the exact physical mechanism. This would lead to the further deployment of this technique for other metamaterials related applications as well.

A resonance-based terahertz metamaterial sensor has been created for highly absorptive water methanol mixture sensing. The sensing of aqueous solutions in terahertz range is especially challenging due to strong absorption of water in this range. A highly sensitive and label free detection platform for chemical and biological materials has been

developed that utilized the long-sought terahertz spectroscopy system for sensing. Since most of the chemical and biological materials are readily available in aqueous solution, our resonance-based terahertz metamaterial sensor platform reduces the extra cost of sample dehydration by offering the capability to detect these samples directly in aqueous solutions, thus making the entire process cost effective as well. This research further presents a broadband transmission-based polarization converter by employing near field coupling between tri-layered metamaterials at terahertz frequencies. Here, we demonstrated significant bandwidth broadening and polarization conversion efficiency higher than 80% by coupling number of near frequency resonances together. Once again, the excellent overlap between simulation and experimental results establishes the potency of the design and techniques employed.

All the metamaterial designs developed in this research have contributed towards the enrichment of the terahertz application platforms. Once we have established a strong working metamaterial design and technique our next step would be to develop an active control mechanism for the terahertz metamaterial-based applications. The ability of any application or device to perform on demand is quintessential to establish its suitability, utility and demand. Thus, introduction of an active control mechanism to these metamaterial designs becomes crucial in order to develop this design towards devices.

The metamaterial designs produced in this research have the potential to utilize electrical or optical bias as an active control mechanism; for example, by a simple addition of thin layer of graphene to these designs. Another fascinating possibility could be studying the behavior of these metamaterials design under extremely low and high temperature conditions or introduction of stress as a control mechanism. An appropriate control mechanism (e.g., electrical, thermal, stress or optical) can be selected based on the requirement of the specific application where these metamaterial designs would serve as core compenents for terahaterz devices.

REFERENCES

1. Campbell, T., et al., Broadband and low loss high refractive index metamaterials in the microwave regime. Applied Physics Letters, 2013. **102**(9).

2. Engheta, N., *Pursuing Near-Zero Response.* Science, 2013. **340**(6130): p. 286-287.

3. van Exter, M., C. Fattinger, and D. Grischkowsky, *Terahertz time-domain spectroscopy of water vapor*. Optics Letters, 1989. **14**(20): p. 1128-1130.

4. Bradley Ferguson, X.-C.Z., *Materials for terahertz science.pdf*. Nature Materials, **2002**. **1**.

5. Grischkowsky, D., et al., *Far-infrared time-domain spectroscopy with terahertz beams of dielectrics and semiconductors.* Journal of the Optical Society of America B, 1990. **7**(10): p. 2006-2015.

6. Huber, R., et al., How many-particle interactions develop after ultrafast excitation of an electron–hole plasma. Nature, 2001. **414**(6861): p. 286-289.

7. Sirtori, C., Bridge for the terahertz gap.pdf. Nature, 2002. **417**.

8. Singh, L. and W. Zhang, Advancements in high refractive index media: from quantum coherence in atomic systems to deep sub-wavelength coupling in metamaterials [Invited]. Chinese Optics Letters, 2020. **18**(6): p. 062401.

9. Scherer, A., et al., Guest editorial: Electromagnetic crystal structures, design, synthesis, and applications. Journal of Lightwave Technology, 1999. **17**: p. 1928-1930.

10. Lakhtakia, A., W. Weiglhofer, and I. Hodgkinson, Complex Mediums II: Beyond Linear Isotropic Dielectrics. 2001Jun, C.T., D. Smith, and R. Liu, *Metamaterials*. 2010.

11. Pimenov, A. and A. Loidl, Experimental demonstration of artificial dielectrics with a high index of refraction. Physical Review B, 2006. **74**(19).

12. Singh, L., R. Singh, and W. Zhang, Ultra-high terahertz index in deep subwavelength coupled bi-layer free-standing flexible metamaterials. Journal of Applied Physics, 2017. **121**(23).

13. Jakšić, Z., N. Dalarsson, and M. Maksimović, *Negative refractive index metamaterials: Principles and applications.* Mikrotalasna revija, 2006: p. 36-49.

14. Padilla, W.J., D.N. Basov, and D.R. Smith, *Negative refractive index metamaterials.* Materials Today, 2006. **9**(7): p. 28-35.

15. Pendry, J., *Electromagnetic materials enter the negative age.* Physics World, 2001. **14**(9): p. 47-51.

16. Wiltshire, M.C.K., et al., Metamaterial endoscope for magnetic field transfer: near field imaging with magnetic wires. Optics Express, 2003. **11**(7): p. 709-715.

17. Smith, D.R., et al., Composite Medium with Simultaneously Negative Permeability and Permittivity. Physical Review Letters, 2000. **84**(18): p. 4184-4187.

18. Shelby, R.A., D.R. Smith, and S. Schultz, *Experimental Verification of a Negative Index of Refraction.* Science, 2001. **292**(5514): p. 77-79.

19. Moser, H.O., et al., Terahertz Response of a Microfabricated Rod--Split-Ring-Resonator Electromagnetic Metamaterial. Physical Review Letters, 2005. **94**(6): p. 063901.

20. Casse, B.D.F., et al., *Fabrication of 2D and 3D Electromagnetic Metamaterials for the Terahertz Range.* Journal of Physics: Conference Series, 2006. **34**: p. 885-890.

21. Casse, B.D.F., et al., Towards three-dimensional and multilayer rod-split-ring metamaterial structures by means of deep x-ray lithography. Applied Physics Letters, 2007. **90**(25): p. 254106.

22. Lin, J., D. Li, and W. Yu. A review of zero index metamaterial. in 2017 IEEE Electrical Design of Advanced Packaging and Systems Symposium (EDAPS). 2017.

23. Liberal, I. and N. Engheta, *Near-zero refractive index photonics.* Nature Photonics, 2017. **11**(3): p. 149-158.

24. Suzuki, T. and H. Asada, Reflectionless zero refractive index metasurface in the terahertz waveband. Optics Express, 2020. **28**(15): p. 21509-21521.

25. Fontana, J. and R. Pantell, *A high-energy, laser accelerator for electrons using the inverse Cherenkov effect.* Journal of applied physics, 1983. **54**(8): p. 4285-4288.

26. E. Bochove, G.M., M. O. Scully, and K. Wodkiewicz, Proceedings of the SPIE's Optical Engineering Southcentral '91 Conference, Dallas, Texas.

27. B. Born, E.W., *Principles of Optics (Pergamon, Oxford).* Principles of Optics Pergamon, Oxford, 1980.

28. M. Bouchiat, G.G.a.R.S., New Trends in Atomic Physics, Proceedings of Les Houches Summer School. 1982.

29. Scully, M.O., Enhancement of the index of refraction via quantum coherence. Phys Rev Lett, 1991. **67**(14): p. 1855-1858.

30. Mlynek, J. and W. Lange, *A simple method of observing coherent ground state transients.* Optics Communications, 1979. **30**(3): p. 337-340.

31. Winters, M.P., J.L. Hall, and P.E. Toschek, *Correlated spontaneous emission in a Zeeman laser.* Physical Review Letters, 1990. **65**(25): p. 3116-3119.

32. Gray, H.R., R.M. Whitley, and C.R. Stroud, *Coherent trapping of atomic populations.* Optics Letters, 1978. **3**(6): p. 218-220.

33. Alzetta, G., et al., An experimental method for the observation of r.f. transitions and laser beat resonances in oriented Na vapour. Il Nuovo Cimento B (1971-1996), 1976. **36**(1): p. 5-20.

34. Fleischhauer, M., et al., Resonantly enhanced refractive index without absorption via atomic coherence. Physical Review A, 1992. **46**(3): p. 1468-1487.

35. Zibrov, A.S., et al., Experimental demonstration of enhanced index of refraction via quantum coherence in Rb. Phys Rev Lett, 1996. **76**(21): p. 3935-3938.

36. Dowling, J.P. and C.M. Bowden, *Anomalous Index of Refraction in Photonic Bandgap Materials.* Journal of Modern Optics, 1994. **41**(2): p. 345-351.

37. Scherer, A., et al., Guest editorial: Electromagnetic crystal structures, design, synthesis, and applications. Journal of Lightwave Technology, 1999. **17**(11): p. 1928-1930.

38. Walser, R.M., et al., Electromagnetic metamaterials, in Complex Mediums II: Beyond Linear Isotropic Dielectrics. 2001.

39. Shen, J.T., P.B. Catrysse, and S. Fan, *Mechanism for designing metallic metamaterials with a high index of refraction.* Phys Rev Lett, 2005. **94**(19): p. 197401.

40. Alastair P. Hibbins, B.R.E., J. Roy Sambles, *Experimental Verification of designer surface plasmons.* Science, 2005. **308**(5722): p. 670-672.

41. Ruan, Z. and M. Qiu, Slow electromagnetic wave guided in subwavelength region along one-dimensional periodically structured metal surface. Applied Physics Letters, 2007. **90**(20).

42. Shin, Y.-M., et al., Frequency-dependent refractive index of one-dimensionally structured thick metal film. Applied Physics Letters, 2007. **91**(3).

43. Shin, J., J.T. Shen, and S. Fan, Three-dimensional metamaterials with an ultrahigh effective refractive index over a broad bandwidth. Phys Rev Lett, 2009. **102**(9): p. 093903.

44. Shi, H., et al., Characterization for metamaterials with a high refractive index formed by periodic stratified metallic wires array. Applied Physics A, 2009. **97**(4): p. 799-803.

45. Wei, X., et al., A high refractive index metamaterial at visible frequencies formed by stacked cut-wire plasmonic structures. Applied Physics Letters, 2010. **97**(1).

46. Choi, M., et al., A terahertz metamaterial with unnaturally high refractive index. Nature, 2011. **470**(7334): p. 369-73.

47. Seo, M.A., et al., Terahertz field enhancement by a metallic nano slit operating beyond the skin-depth limit. Nature Photonics, 2009. **3**: p. 152.

48. Barry, W., A Broad-Band, Automated, Stripline Technique for the Simultaneous Measurement of Complex Permittivity and Permeability. IEEE Transactions on Microwave Theory and Techniques, 1986. **34**(1): p. 80-84.

49. Tan, S., et al., Terahertz metasurfaces with a high refractive index enhanced by the strong nearest neighbor coupling. Opt Express, 2015. **23**(22): p. 29222-30.

50. Chang, T., et al., Broadband giant-refractive-index material based on mesoscopic space-filling curves. Nat Commun, 2016. **7**: p. 12661.

51. Lu, Z., B. Camps-Raga, and N.E. Islam, Design and Analysis of a THz Metamaterial Structure with High Refractive Index at Two Frequencies. Physics Research International, 2012. **2012**: p. 1-9.

52. Fang, B., et al., Realization of ultrahigh refractive index in terahertz region by multiple layers coupled metal ring metamaterials. Journal of Electromagnetic Waves and Applications, 2019. **33**(11): p. 1375-1390.

53. Lee, S.H., et al., Ultrafast refractive index control of a terahertz graphene metamaterial. Scientific Reports, 2013. **3**: p. 2135.

54. Zhu, B., et al., Nanoscale dielectric-graphene-dielectric tunable infrared waveguide with ultrahigh refractive indices. Opt Express, 2013. **21**(14): p. 17089-96.

55. Pendry, J.B., et al., *Magnetism from conductors and enhanced nonlinear phenomena.* IEEE Transactions on Microwave Theory and Techniques, 1999. **47**(11): p. 2075-2084.

56. Yen, T.-J., et al., *Terahertz magnetic response from artificial materials.* Science, 2004. **303**(5663): p. 1494-1496.

57. Schurig, D., J. Mock, and D. Smith, *Electric-field-coupled resonators for negative permittivity metamaterials.* Applied Physics Letters, 2006. **88**(4): p. 041109.

58. Smith, D.R., J.B. Pendry, and M.C. Wiltshire, *Metamaterials and negative refractive index.* Science, 2004. **305**(5685): p. 788-792.

59. Pendry, J.B., et al., *Extremely low frequency plasmons in metallic mesostructures.* Physical Review Letters, 1996. **76**(25): p. 4773-4776.

60. Pendry, J.B., *Negative refraction makes a perfect lens.* Physical Review Letters, 2000. **85**(18): p. 3966-3969.

61. Yahiaoui, R., V. Vignéras, and P. Mounaix, *Theoretical and experimental investigations of easy made fishnet metamaterials at microwave frequencies.* Applied Physics A: Materials Science & Processing, 2011. **103**(3): p. 685-688.

62. Ziolkowski, R.W., Propagation in and scattering from a matched metamaterial having a zero index of refraction. Physical Review E, 2004. **70**(4): p. 046608.

63. Alu, A., et al., Epsilon-near-zero metamaterials and electromagnetic sources: Tailoring the radiation phase pattern. Physical review B, 2007. **75**(15): p. 155410.

64. Enoch, S., et al., *A metamaterial for directive emission.* Physical Review Letters, 2002. **89**(21): p. 213902.

65. Silveirinha, M. and N. Engheta, Tunneling of electromagnetic energy through subwavelength channels and bends using ε-near-zero materials. Physical review letters, 2006. **97**(15): p. 157403.

66. Tan, S., et al., Terahertz metasurfaces with a high refractive index enhanced by the strong nearest neighbor coupling. Optics Express, 2015. **23**(22): p. 29222-29230.

67. Shin, J., J.T. Shen, and S. Fan, Three-dimensional metamaterials with an ultrahigh effective refractive index over a broad bandwidth. Physical Review Letters, 2009. **102**(9).

68. Choi, M., et al., A terahertz metamaterial with unnaturally high refractive index. Nature, 2011. **470**(7334): p. 369-373.

69. Enkrich, C., et al., *Magnetic metamaterials at telecommunication and visible frequencies.* Physical review letters, 2005. **95**(20): p. 203901.

70. Sievenpiper, D., et al., 3D metallo-dielectric photonic crystals with strong capacitive coupling between metallic islands. Physical Review Letters, 1998. **80**(13): p. 2829.

71. Shen, J.T., P.B. Catrysse, and S. Fan, Mechanism for designing metallic metamaterials with a high index of refraction. Physical Review Letters, 2005. **94**(19).

72. Chen, H.T., et al., *Manipulation of terahertz radiation using metamaterials.* Laser & Photonics Reviews, 2011. **5**(4): p. 513-533.

73. Sirtori, C., *Applied physics: Bridge for the terahertz gap.* Nature, 2002. **417**(6885): p. 132-133.

74. Yahiaoui, R., et al., Terahertz metamolecules deposited on thin flexible polymer: design, fabrication and experimental characterization. Journal of Optics, 2014. **16**(9): p. 094014.

75. Yahiaoui, R., et al., Ultra-flexible multiband terahertz metamaterial absorber for conformal geometry applications. Optics letters, 2013. **38**(23): p. 4988-4990.

76. Mansfield, S.M. and G.S. Kino, *Solid immersion microscope*. Applied Physics Letters, 1990. **57**(24): p. 2615-2616.

77. Karalis, A., et al., Surface-plasmon-assisted guiding of broadband slow and subwavelength light in air. Physical Review Letters, 2005. **95**(6).

78. Shi, Z., et al., *Slow-light fourier transform interferometer*. Physical Review Letters, 2007. **99**(24).

79. Lu, Z., B. Camps-Raga, and N. Islam, Design and analysis of a THz metamaterial structure with high refractive index at two frequencies. Physics Research International, 2012. **2012**.

80. Azad, A.K., J. Dai, and W. Zhang, Transmission properties of terahertz pulses through subwavelength double split-ring resonators. Optics letters, 2006. **31**(5): p. 634-636.

81. Thamizhmani, L., et al., Far-infrared optical and dielectric response of ZnS measured by terahertz time-domain spectroscopy. Applied Physics Letters, 2005. **86**(13): p. 131111.

82. Azad, A.K., Y. Zhao, and W. Zhang, Transmission properties of terahertz pulses through an ultrathin subwavelength silicon hole array. Applied Physics Letters, 2005. **86**(14): p. 141102.

83. Laman, N. and D. Grischkowsky, *Terahertz conductivity of thin metal films.* Applied Physics Letters, 2008. **93**(5): p. 051105.

84. Smith, D., et al., Determination of effective permittivity and permeability of metamaterials from reflection and transmission coefficients. Physical Review B, 2002. **65**(19): p. 195104.

85. Chen, X., et al., *Robust method to retrieve the constitutive effective parameters of metamaterials.* Physical Review E - Statistical, Nonlinear, and Soft Matter Physics, 2004. **70**(1 2): p. 016608-1-016608-7.

86. Szabó, Z., et al., *A unique extraction of metamaterial parameters based on Kramers-Kronig relationship.* IEEE Transactions on Microwave Theory and Techniques, 2010. **58**(10): p. 2646-2653.

87. Yahiaoui, R., et al., Towards left-handed metamaterials using single-size dielectric resonators: The case of TiO 2-disks at millimeter wavelengths. Applied Physics Letters, 2012. **101**(4).

88. Yahiaoui, R., et al., Broadband dielectric terahertz metamaterials with negative permeability. Optics letters, 2009. **34**(22): p. 3541-3543.

89. Yahiaoui, R., et al., Broadband effective magnetic response of inorganic dielectric resonator-based metamaterial for microwave applications. Applied Physics A: Materials Science and Processing, 2014. **114**(3): p. 997-1002.

90. Markel, V.A., *Can the imaginary part of permeability be negative?* Physical Review E, 2008. **78**(2): p. 026608.

91. Depine, R.A. and A. Lakhtakia, *Comment I on "Resonant and antiresonant frequency dependence of the effective parameters of metamaterials".* Physical Review E - Statistical Physics, Plasmas, Fluids, and Related Interdisciplinary Topics, 2004. **70**(4): p. 1.

92. Efros, A., Comment II on "Resonant and antiresonant frequency dependence of the effective parameters of metamaterials". Physical Review E, 2004. **70**(4): p. 048602.

93. Koschny, T., et al., Resonant and antiresonant frequency dependence of the effective parameters of metamaterials. Physical Review E, 2003. **68**(6): p. 065602.

94. Liu, N., et al., Three-dimensional photonic metamaterials at optical frequencies. Nature materials, 2008. **7**(1): p. 31-37.

95. Markoš, P., et al., Wave Scattering in Complex Media: From Theory to Application. 2003. 309.

96. Linden, S., et al., *Magnetic response of metamaterials at 100 terahertz.* Science, 2004. **306**(5700): p. 1351-1353.

97. Pendry, J.B., D. Schurig, and D.R. Smith, *Controlling electromagnetic fields.* Science, 2006. **312**(5781): p. 1780-1782.

98. Schurig, D., et al., Metamaterial electromagnetic cloak at microwave frequencies. Science, 2006. **314**(5801): p. 977-980.

99. Smolyaninov, I.I., Y.J. Hung, and C.C. Davis, *Magnifying superlens in the visible frequency range.* Science, 2007. **315**(5819): p. 1699-1701.

100. Valentine, J., et al., Three-dimensional optical metamaterial with a negative refractive index. Nature, 2008. **455**(7211): p. 376-379.

101. Zhang, S., et al., *Negative refractive index in chiral metamaterials.* Physical Review Letters, 2009. **102**(2).

102. Lee, H.J. and J.G. Yook, *Biosensing using split-ring resonators at microwave regime.* Applied Physics Letters, 2008. **92**(25).

103. Hao, F., et al., Tunability of subradiant dipolar and fano-type plasmon resonances in metallic ring/disk cavities: Implications for nanoscale optical sensing. ACS Nano, 2009. **3**(3): p. 643-652.

104. Kabashin, A.V., et al., *Plasmonic nanorod metamaterials for biosensing.* Nature Materials, 2009. **8**(11): p. 867-871.

105. Liu, N., et al., Infrared perfect absorber and its application as plasmonic sensor. Nano Letters, 2010. **10**(7): p. 2342-2348.

106. Wiwatcharagoses, N., et al. Microwave artificially structured periodic media microfluidic sensor. in Proceedings - Electronic Components and Technology Conference. 2011.

107. Chen, T., S. Li, and H. Sun, *Metamaterials application in sensing.* Sensors, 2012. **12**(3): p. 2742-2765.

108. Reinhard, B., et al., Metamaterial near-field sensor for deep-subwavelength thickness measurements and sensitive refractometry in the terahertz frequency range. Applied Physics Letters, 2012. **100**(22).

109. Xie, L., et al., Extraordinary sensitivity enhancement by metasurfaces in terahertz detection of antibiotics. Scientific Reports, 2015. **5**.

110. Debus, C. and P.H. Bolivar, Frequency selective surfaces for high sensitivity terahertz sensing. Applied Physics Letters, 2007. **91**(18).

111. Al-Naib, I.A.I., C. Jansen, and M. Koch, *Thin-film sensing with planar asymmetric metamaterial resonators.* Applied Physics Letters, 2008. **93**(8).

112. O'Hara, J.F., et al., Thin-film sensing with planar terahertz metamaterials: Sensitivity and limitations. Optics Express, 2008. **16**(3): p. 1786-1795.

113. Sun, Y., et al., Modulated terahertz responses of split ring resonators by nanometer thick liquid layers. Applied Physics Letters, 2008. **92**(22).

114. Tian, Z., et al., Surface plasmon enhanced terahertz spectroscopic distinguishing between isotopes. Chemical Physics Letters, 2009. **475**(1-3): p. 132-134.

115. Ng, B., et al., Lattice resonances in antenna arrays for liquid sensing in the terahertz regime. Optics Express, 2011. **19**(15): p. 14653-14661.

116. Tao, H., et al., *Metamaterials on paper as a sensing platform.* Advanced Materials, 2011. **23**(28): p. 3197-3201.

117. Wu, X., et al., Self-referenced sensing based on terahertz metamaterial for aqueous solutions. Applied Physics Letters, 2013. **102**(15).

118. Wu, X., et al., Alkanethiol-functionalized terahertz metamaterial as label-free, highly-sensitive and specific biosensor. Biosensors and Bioelectronics, 2013. **42**(1): p. 626-631.

119. Miyamaru, F., et al., *Highly sensitive terahertz sensing of glycerol-water mixtures with metamaterials.* Journal of Infrared, Millimeter, and Terahertz Waves, 2014. **35**(2): p. 198-207.

120. Park, S.J., et al., Detection of microorganisms using terahertz metamaterials. Scientific Reports, 2014. **4**.

121. Singh, R., et al., Ultrasensitive terahertz sensing with high- Q Fano resonances in metasurfaces. Applied Physics Letters, 2014. **105**(17).

122. Cong, L., et al., Experimental demonstration of ultrasensitive sensing with terahertz metamaterial absorbers: A comparison with the metasurfaces. Applied Physics Letters, 2015. **106**(3).

123. Seto, H., et al., Label-free detection of antigen protein using a metal mesh device surface-modified by an antibody. Analytical Sciences, 2015. **31**(3): p. 173-176.

124. Hasegawa, M., et al., Surface Coating of a Metal Mesh Device Sensor with Gold to Improve the Separation and Sensing of Mammalian Cells. IEEE Sensors Journal, 2016. **16**(13): p. 5129-5135.

125. Tao, H., et al., Terahertz metamaterials on free-standing highly-flexible polyimide substrates. Journal of Physics D: Applied Physics, 2008. **41**(23).

126. Gu, J., et al., A close-ring pair terahertz metamaterial resonating at normal incidence. Optics Express, 2009. **17**(22): p. 20307-20312.

127. Tao, H., et al., Performance enhancement of terahertz metamaterials on ultrathin substrates for sensing applications. Applied Physics Letters, 2010. **97**(26).

128. Chen, Y., et al., Membrane metamaterial resonators with a sharp resonance: A comprehensive study towards practical terahertz filters and sensors. AIP Advances, 2012. **2**(2).

129. Chen, L., et al., Excitation of dark multipolar plasmonic resonances at terahertz frequencies. Scientific Reports, 2016. **6**.

130. Xu, N., R. Singh, and W. Zhang, Collective coherence in nearest neighbor coupled metamaterials: A metasurface ruler equation. Journal of Applied Physics, 2015. **118**(16).

131. Singh, R., et al., *Sharp Fano resonances in THz metamaterials.* Optics Express, 2011. **19**(7): p. 6312-6319.

132. Liu, N., S. Kaiser, and H. Giessen, *Magnetoinductive and electroinductive coupling in plasmonic metamaterial molecules.* Advanced Materials, 2008. **20**(23): p. 4521-4525.

133. Liu, N., et al., Plasmonic analogue of electromagnetically induced transparency at the Drude damping limit. Nature Materials, 2009. **8**(9): p. 758-762.

134. Singh, R., et al., Probing the transition from an uncoupled to a strong near-field coupled regime between bright and dark mode resonators in metasurfaces. Applied Physics Letters, 2014. **105**(8).

135. Cong, L., et al., Fano Resonances in Terahertz Metasurfaces: A Figure of Merit Optimization. Advanced Optical Materials, 2015. **3**(11): p. 1537-1543.

136. Kindt, J.T. and C.A. Schmuttenmaer, Far-infrared dielectric properties of polar liquids probed by femtosecond terahertz pulse spectroscopy. Journal of Physical Chemistry, 1996. **100**(24): p. 10373-10379.

137. Arik, E., H. Altan, and O. Esenturk, Dielectric properties of ethanol and gasoline mixtures by terahertz spectroscopy and an effective method for determination of ethanol content of gasoline. Journal of Physical Chemistry A, 2014. **118**(17): p. 3081-3089.

138. Thrane, L., et al., *THz reflection spectroscopy of liquid water.* Chemical Physics Letters, 1995. **240**(4): p. 330-333.

139. Asaki, M.L.T., et al., Dielectric relaxation of electrolyte solutions using terahertz transmission spectroscopy. Journal of Chemical Physics, 2002. **116**(19): p. 8469-8482.

140. Ferguson, B. and X.C. Zhang, *Materials for terahertz science and technology.* Nature Materials, 2002. **1**(1): p. 26-33.

141. Federici, J.F., et al., *THz imaging and sensing for security applications - Explosives, weapons and drugs.* Semiconductor Science and Technology, 2005. **20**(7): p. S266-S280.

142. Piesiewicz, R., et al., *Short-range ultra-broadband terahertz communications: Concepts and perspectives.* IEEE Antennas and Propagation Magazine, 2007. **49**(6): p. 24-39.

143. Chen, H.T., et al., *A metamaterial solid-state terahertz phase modulator.* Nature Photonics, 2009. **3**(3): p. 148-151.

144. Sensale-Rodriguez, B., et al., *Unique prospects for graphene-based terahertz modulators.* Applied Physics Letters, 2011. **99**(11).

145. Hasan, N., H. Kim, and C.H. Mastrangelo, *Large aperture tunable-focus liquid lens using shape memory alloy spring.* Optics Express, 2016. **24**(12): p. 13334-13342.

146. Masson, J.B. and G. Gallot, *Terahertz achromatic quarter-wave plate.* Optics Letters, 2006. **31**(2): p. 265-267.

147. Shen, N.H., et al., Optically implemented broadband blueshift switch in the terahertz regime. Physical Review Letters, 2011. **106**(3).

148. Cong, L., et al., Manipulating polarization states of terahertz radiation using metamaterials. New Journal of Physics, 2012. **14**.

149. Cong, L., et al., *A perfect metamaterial polarization rotator.* Applied Physics Letters, 2013. **103**(17).

150. Chen, C.Y., et al., Room temperature terahertz phase shifter based on magnetically controlled birefringence in liquid crystals. Applied Physics Letters, 2003. **83**(22): p. 4497-4499.

151. Xu, J., et al., Manipulating optical polarization by stereo plasmonic structure. Optics Express, 2011. **19**(2): p. 748-756.

152. Mutlu, M. and E. Ozbay, A transparent 90 polarization rotator by combining chirality and electromagnetic wave tunneling. Applied Physics Letters, 2012. **100**(5).

153. Holloway, C.L., et al., An overview of the theory and applications of metasurfaces: The two-dimensional equivalents of metamaterials. IEEE Antennas and Propagation Magazine, 2012. **54**(2): p. 10-35.

154. Liang, D., et al., *Robust large dimension terahertz cloaking.* Advanced Materials, 2012. **24**(7): p. 916-921.

155. Cui, T.J., et al., Coding metamaterials, digital metamaterials and programmable metamaterials. Light: Science and Applications, 2014. **3**(10).

156. Cheng, Y.Z., et al., Ultrabroadband reflective polarization convertor for terahertz waves. Applied Physics Letters, 2014. **105**(18).

157. Lévesque, Q., et al., Plasmonic planar antenna for wideband and efficient linear polarization conversion. Applied Physics Letters, 2014. **104**(11).

158. Mo, W., et al., Ultrathin flexible terahertz polarization converter based on metasurfaces. Optics Express, 2016. **24**(12): p. 13621-13627.

159. Chiang, Y.J. and T.J. Yen, A composite-metamaterial-based terahertz-wave polarization rotator with an ultrathin thickness, an excellent conversion ratio, and enhanced transmission. Applied Physics Letters, 2013. **102**(1).

160. Liu, W., et al., Realization of broadband cross-polarization conversion in transmission mode in the terahertz region using a single-layer metasurface. Optics Letters, 2015. **40**(13): p. 3185-3188.

161. Grady, N.K., et al., Terahertz metamaterials for linear polarization conversion and anomalous refraction. Science, 2013. **340**(6138): p. 1304-1307.

162. Yu, N., et al., Light propagation with phase discontinuities: Generalized laws of reflection and refraction. Science, 2011. **334**(6054): p. 333-337.

VITA

Leena Singh

Candidate for the Degree of

Doctor of Philosophy

Thesis: TERAHERTZ METAMATERIALS: REFRACTIVE INDEX, SENSING, AND RESONANCES

Major Field: Electrical Engineering

Biographical:

Education:

Completed the requirements for the Doctor of Philosophy in Electrical Engineering at Oklahoma State University, Stillwater, Oklahoma in July 2021.

Completed the requirements for the Master of Science in Electrical Engineering at Oklahoma State University, Stillwater, Oklahoma in December 2015.

Completed the requirements for the Bachelor of Technology in Electronics and Communication at ABES Engineering College, Ghaziabad, India, in 2008.

Experience:

Lecturer at Apollo Institute of Technology, Kanpur, India from 2008-2009, Software Engineer at Infosys and FIS, India from 2009-2013, Graduate Assistant at Ceat Online Learning, Oklahoma State University from 2013-2021, Visiting Ph.D. Scholar at Tianjin University, China for Summer 2018, Served as Graduate College Ambassador at Oklahoma State University from 2020-2021, Graduate Student at Los Alamos national Laboratory, New Mexico from April 2021 to present.

Professional Memberships: Student member of OSA and SPIE.

LIST OF PUBLICATIONS

1. L. Singh and W. Zhang, "Terahertz index of refraction engineering," World Scientific, 2021 (Book Chapter To Be Published.)
2. L. Singh and W. Zhang, "Advancements in high refractive index media: from quantum coherence in atomic systems to deep sub-wavelength coupling in metamaterials [Invited]," Chin. Opt. Lett. Vol. 18, pp. 062401, 2020.
3. X. Gao, L. Singh, W. Yang, J. Zheng, H. Li, and W. Zhang, "Bandwidth broadening of a linear polarization converter by near-field metasurface coupling," Scientific reports, vol. 7, p. 6817, 2017.
4. L. Singh, R. Singh, and W. Zhang, "Ultra-high terahertz index in deep subwavelength coupled bi-layer free-standing flexible metamaterials," Journal of Applied Physics, vol. 121, p. 233103, 2017.
5. M. Chen, L. Singh, N. Xu, R. Singh, W. Zhang, and L. Xie, "Terahertz sensing of highly absorptive water-methanol mixtures with multiple resonances in metamaterials," Optics express, vol. 25, pp. 14089-14097, 2017.
6. J. Zheng, X. Zhang, L. Liu, Q. Li, L. Singh, J. Han, et al., "Tailoring Terahertz Propagation by Phase and Amplitude Control in Metasurfaces," Journal of Infrared, Millimeter, and Terahertz Waves, vol. 38, pp. 1034-1046, 2017.
7. L. Chen, N. Xu, L. Singh, T. Cui, R. Singh, Y. Zhu, et al., "Defect-Induced Fano Resonances in Corrugated Plasmonic Metamaterials," Advanced Optical Materials, vol. 5, p. 1600960, 2017.
8. Metamaterial with near zero refractive index at terahertz frequency: conference talk, publication description SPIE Optics + Photonics, publication date Sep 1, 2016.

9. S. Tan, F. Yan, L. Singh, W. Cao, N. Xu, X. Hu, et al., "Terahertz metasurfaces with a high refractive index enhanced by the strong nearest neighbor coupling," Optics express, vol. 23, pp. 29222-29230, 2015.